Developing an energy efficient steam reforming process to produce hydrogen from sulfur-containing fuels

Amanda Simson

Submitted in partial fulfillment of the
requirements for the degree
of Doctor of Philosophy
in the Graduate School of Arts and Sciences

COLUMBIA UNIVERSITY

2013

ABSTRACT

Developing an energy efficient steam reforming process to produce hydrogen from sulfur-containing fuels

Amanda Simson

Hydrogen powered fuel cells have the potential to produce electricity with higher efficiency and lower emissions than conventional combustion technology. In order to realize the benefits of a hydrogen fuel cell an efficient method to produce hydrogen is needed. Currently, over 90% of hydrogen is produced from the steam reforming of natural gas. However, for many applications including fuel cell vehicles, the use of a liquid fuel rather than natural gas is desirable. This work investigates the feasibility of producing hydrogen efficiently by steam reforming E85 (85% ethanol/15% gasoline), a commercially available sulfur-containing transportation fuel. A Rh-Pt/SiO_2-ZrO_2 catalyst has demonstrated good activity for the E85 steam reforming reaction.

An industrial steam reforming process is often run less efficiently, with more water and at higher temperatures, in order to prevent catalyst deactivation. Therefore, it is desirable to develop a process that can operate without catalyst deactivation at more energy efficient conditions. In this study, the steam reforming of a sulfur-containing fuel (E85) was studied at

near stoichiometric steam/carbon ratios and at 650°C, conditions at which catalyst deactivation is normally measured. At these conditions the catalyst was found to be stable steam reforming a sulfur-free E85. However, the addition of low concentrations of sulfur significantly deactivated the catalyst.

The presence of sulfur in the fuel caused catalyst deactivation by promoting ethylene which generates surface carbon species (coke) that mask catalytic sites. The amount of coke increased during time on stream and became increasingly graphitic. However, the deactivation due to both sulfur adsorption and coke formation was reversible with air treatment at 650°C. However, regenerations were found to reduce the catalyst life.

Air regenerations produce exotherms on the catalyst surface that cause structural changes to the catalyst. During regenerations the accessibility of the precious metal particles is reduced which causes the catalyst to deactivate more rapidly during subsequent steam reforming cycles. Changes to the carrier morphology also occur at these conditions. Regenerating the catalyst before significant deactivation is measured can improve the stability of the catalyst. Thus a process with preemptive controlled air regenerations is proposed in order to run a steam reforming process with sulfur containing fuels.

Table of Contents

List of Figures

List of Tables

Acknowledgements

I would like to thank my advisors, Professors Marco Castaldi and Robert Farrauto, for their guidance and support during the Ph.D. My advisors taught me how to perform, present and enjoy scientific research and for that I will be forever grateful. I would also like to thank current and former members in both the Combustion and Catalysis research group and in the Catalysis for a Sustainable Environment research group. Specifically, I would like to thank Naomi Klinghoffer, Dr. Christiane Janke, Melis Duyar, Qinghe Zheng, Emi Leung, Garrett Fitzgerald, Marcella Lusardi, Heather Lanman, Tim Sharobem, Dr. McKenzie Kohn, Dr. Federico Barrai, Dr. Forrest Zhou, Dr. Eilhann Kwon, and Dr. Lucas Dorazio. I would also like to thank several BASF employees who contributed to this project including Nancy Brungard, Sharon Walsh and George Munzing. Additionally, I would like to thank Dr. Antonio Sanchez at Brooklyn College for several valuable discussions on my research. Finally, I would like to thank my family and friends for their love and support during my studies.

This thesis is dedicated to my family

Chapter 1 : Introduction

1.1 Motivation

The average global surface temperature has increased by nearly 1°C over the past hundred years [1]. The associated impacts of this level of warming include rising sea levels, drought, and decreases in crop yields. Additional increases of up to 2-6°C are expected over the next century [1]. The impacts of this change in climate will pose significant challenges for future generations. The recent changes in climate are due to increasing levels of atmospheric CO_2; primarily caused by the burning of fossil fuels. To mitigate the impacts of climate change we must develop cleaner, more efficient methods to generate power. Fuel cells are a promising method to generate electricity with higher efficiencies and lower greenhouse gas emissions than traditional combustion technology. There are several different types of fuel cells, however, the most suitable for vehicle or portable power generation is the low temperature Proton Exchange Membrane (PEM) fuel cell [2].

Fuel cells convert chemical energy directly to electricity. Because fuel cells are not heat engines they are not limited by certain efficiency limits of traditional combustion engines [3]. In 2012 the efficiency of a PEM hydrogen

fuel cell was approximately 60% [2] whereas the efficiencies of a typical internal combustion engine in a car were 14-26% [4]. These higher efficiencies mean lower CO_2 emissions. Further, fuel cells are easily scalable. Therefore, they can be used in large scale stationary applications like power plants and also for small applications like home electricity production or production of power for vehicles.

The transportation sector is responsible for over 20-30% of the total US CO_2 emissions [5]. Thus, efficiency improvements in vehicles can lead to significant environmental benefits. In 2010 the U.S. Department of Energy (DOE) found that fuel cell vehicles reduce CO_2 emissions of a traditional internal combustion vehicle by 55% and of a hybrid vehicle by 25% [6]. Further, the U.S. DOE found that the cost of fuel cell vehicles had dropped by 83% between 2002 and 2012 [7]. Despite this progress, there are many challenges to large-scale fuel cell deployment; one of which is the efficient production and storage of hydrogen.

PEM fuel cells are most efficient when run on hydrogen fuel [8]. Therefore, an efficient method to produce hydrogen is necessary. Currently hydrogen is primarily produced by steam reforming methane [8]. However, under many circumstances, it is preferred to use a portable (liquid) fuel source rather than gaseous fuels like methane. For example, for fuel cell vehicles, hydrogen will be produced at service stations [9], therefore, it is

preferred to reform a liquid transportation fuel, for which there is already infrastructure in place. In this study we focus on improving the efficiency of producing hydrogen from E85 (an 85% ethanol/15% gasoline blend), a commercially available transportation and primarily bio-derived fuel.

The use of liquid fuels to produce hydrogen and generate electricity via a fuel cell is a process that also has applications outside of the transportation industry. There are many areas of the world where there is neither access to compressed natural gas nor an electrical grid. In these areas, within which 20% of the world's populations reside, electricity must be produced via small-scale technologies such as fuel cells or solar cells. Further, the hydrogen used in the fuel cell must be produced via portable, liquid fuels. Thus, the work described here, utilizing primarily ethanol (a bio-derived fuel produced easily on a small scale) and water to produce hydrogen can directly apply to efforts to bring electrical power to areas that are not connected to a grid. Fuel cells, run on biomass derived liquid fuels (via fuel reforming), are one of a few practical methods to provide electricity in these areas.

In summary, fuel cells are a more efficient and thus more sustainable means to provide electrical power than burning fossil fuels. Fuel cells are especially effective at providing small-scale, decentralized power, and therefore can lower the environmental costs of powering vehicles or other off-grid applications. However, a primary obstacle to fuel cell deployment is the

efficient production of hydrogen. This is particularly important for these off-grid applications where a liquid fuel will be used to generate hydrogen. The purpose of this work is to improve the efficiency of producing hydrogen from liquid fuels utilizing catalyst technology to enable fuel cell use for decentralized power production.

1.2 Choice of feedstock

In addition to developing more efficient methods to generate power, alternative and renewable feedstocks to provide the power should be utilized. Ethanol is a common liquid fuel which is easy and safe to transport and can be produced renewably from most agricultural feedstocks. For these reasons, ethanol has become a common transportation fuel. Studies by Argonne National Lab have determined that using ethanol produced by conventional methods (via corn starch) reduces the greenhouse gas emissions over standard gasoline by 18% to 29% [10]. However, ethanol produced via sugarcane reduces greenhouse gas emissions by 87% to 93% over standard gasoline [10]. Thus, the method to produce the ethanol is an important consideration in measuring the environmental impact of ethanol-based technologies.

Recently there has been an increased focus on converting cellulosic feedstock into ethanol. If cellulosic methods improve, ethanol will be

produced from agricultural waste or from dedicated cellulosic crops grown on typically non-arable land. By increasing yields and utilizing a larger array of feedstocks, cellulosic ethanol has the potential to further reduce the amount of greenhouse gases produced in the utilization of liquid transportation fuels. In 2007 the US government designated $385 million to companies for commercial cellulosic ethanol plants [11]. Before cellulosic ethanol can become a commercial fuel, more significant improvements in yield must occur. Such improvements would come from the design of new thermal processes for cellulosic conversion and the discovery of new enzymes to convert cellulosic feedstocks to ethanol [11].

Ethanol has a lower vapor pressure relative to gasoline and therefore ethanol/gasoline blends such as E85 (85% ethanol), E15 (15% ethanol) or E10 (10% ethanol) are more commonly available then pure ethanol to provide the necessary vapor pressure for automobile cold-start [12]. Although there has been extensive research on the reforming of conventional transportation fuels such as ethanol, gasoline, diesel, or jet fuel there have been very few studies on ethanol/gasoline blends. Since gasoline contains sulfur, a poison for catalysts, the challenge is to reform the sulfur-containing blends. In this work the reforming of both ethanol and ethanol/gasoline blends are studied to demonstrate the feasibility of steam reforming sulfur-containing oxygenated liquid fuels.

1.3 Producing hydrogen efficiently by steam reforming ethanol and E85

Hydrogen can be generated from a liquid fuel, such as ethanol via the following reactions:

POX: $C_2H_5OH + ½\ O_2 \rightarrow 3H_2 + 2CO$ $\Delta H°_{298} = +20\ kJ\ mol^{-1}$ (1)

SR: $C_2H_5OH + 3H_2O \rightarrow 6H_2 + 2CO_2$ $\Delta H°_{298} = +174\ kJ\ mol^{-1}$ (2)

ATR: $C_2H_5OH + 2H_2O + ½\ O_2 \rightarrow 5H_2 + 2CO_2$ $\Delta H°_{298} = -50\ kJ\ mol^{-1}$ (3)

Equations 1-3 include the forward water gas shift (WGS) reaction in their stoichiometry which increases the H_2 production with additional water usage:

WGS: $CO + H_2O + \rightarrow H_2 + CO_2$ $\Delta H°_{298} = -41\ kJ\ mol^{-1}$ (4)

The endothermic steam reforming (SR) reaction (equation 2) requires the addition of heat. However, the heat requirements for SR are outweighed by the increases in hydrogen generated per mole fuel (the heating value of H_2 is 286 kJ/mol). Furthermore, autothermal reforming (ATR) or partial oxidation (POX) frequently use air rather than O_2 which dilutes the concentration of hydrogen with nitrogen. This study will examine only the catalytic steam reforming reaction of ethanol and E85, although this could also provide a baseline for future examination of ATR.

According to the ethanol steam reforming (ESR) reaction (equation 2) the stoichiometric water/ethanol ratio required to produce hydrogen from one mole of ethanol is 3 moles of water per mole ethanol. In addition to producing H_2 and CO_2 (according to the stoichiometry in equation 2), steam reforming

produces CO, CH_4 and unconverted H_2O. The thermodynamically predicted product distribution for ESR with a stoichiometric (3:1) steam/carbon (S/C) ratio is shown in Figure 1.1. The equilibrium product distribution was calculated by minimizing the Gibbs energy function for temperatures between 400-900°C at atmospheric pressure and given the constraint of the atom balance for the reactants. The potential products which the Gibbs function was minimized for were chosen based on products measured experimentally or reported in the literature.

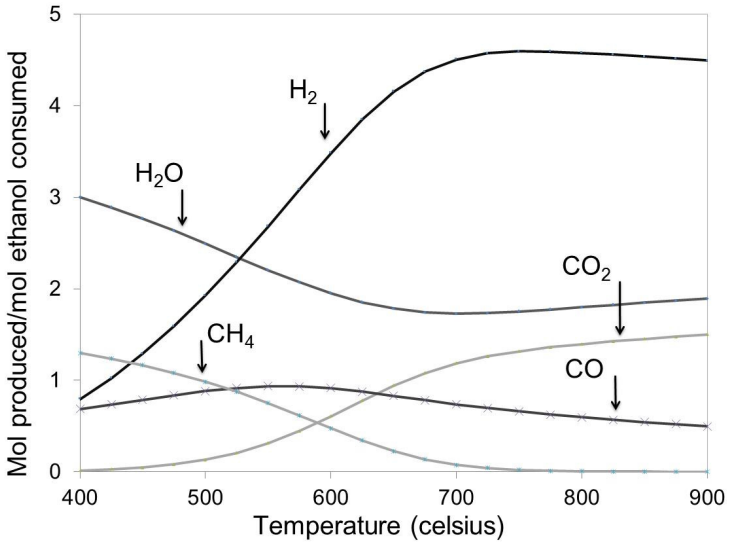

Figure 1.1: Thermodynamically predicted product distribution for stoichiometric water/ethanol

Carbon monoxide, which is produced during the steam reforming reaction regardless of temperature (Figure 1.1) poisons the platinum anode in low temperature fuel cells. Therefore, low temperature fuel cells have severe constraints on the allowable CO concentrations (<10 ppm). To reduce CO

concentrations to allowable levels, the hydrogen production process includes several steps to "clean-up" the CO. An example of the most common hydrogen production process including the CO clean-up is shown in Figure 1.2. In the future, low temperature fuel cells with higher CO tolerance may be developed and allow for a less complex and less energy intensive hydrogen production process.

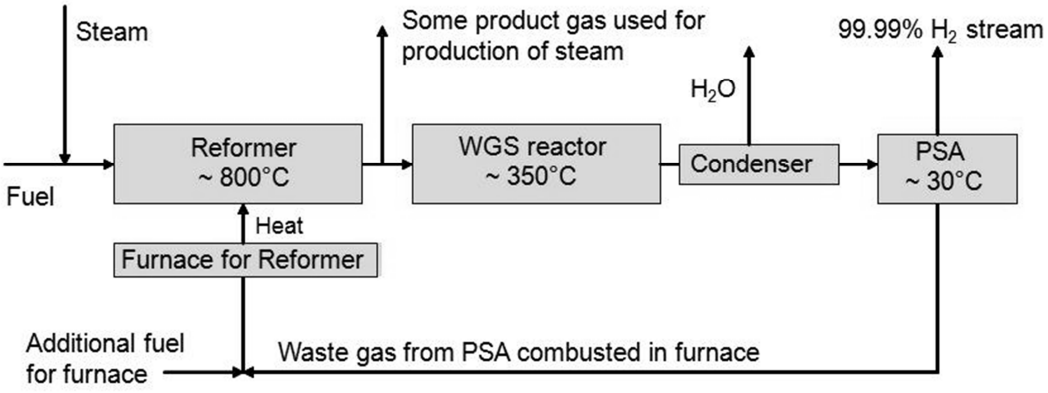

Figure 1.2: Current hydrogen production process for a PEM fuel cell.

The schematic in Figure 1.2 does not include a desulfurization reactor, although they are included in most industrial hydrogen processes. Sulfur is a common catalyst poison and is present in most gaseous and liquid fuels (i.e. natural gas, gasoline, diesel, jetfuel, and bioethanol). Therefore, desulfurization reactors are used to remove sulfur from the fuel prior to the reformer (via sulfur adsorbents). However, the desulfurization process costs energy and is more impractical for small-scale reformers [13]. Thus,

producing hydrogen efficiently with sulfur-tolerant catalysts is desirable, particularly for vehicles and other small-scale applications [13, 14].

In order to determine the optimum reaction conditions to run the reformer, an energy efficiency analysis was performed. The efficiency was calculated as a function of temperature and S/C ratio based on the following definition for efficiency:

$$n_1 = \frac{output}{input} = \frac{nH_2 \cdot HV_{H_2} - Q_{in}}{HV_{EtOH}} \quad (5)$$

The output was calculated from the heating value of hydrogen, HV_{H2}, and the thermodynamically predicted moles of hydrogen produced, nH_2, produced at temperatures between 300 and 1000°C and for S/C ratios between 0:1 to 10:1. This definition accounts for the heat required for the reformer Q_{in} by subtracting this heat from the product stream. The input is the heating value of ethanol HV_{EtOH}. The results of these calculations are shown in Figure 1.3. The maximum efficiencies are achieved at near-stoichiometric water/ethanol conditions and temperatures between 650 and 700°C. These calculations are in good agreement with published thermodynamic studies [15]. The same optimum operating conditions were identified when the analysis was performed with E85 rather than ethanol. The thermodynamic analysis assumed isooctane as a surrogate for the gasoline in E85.

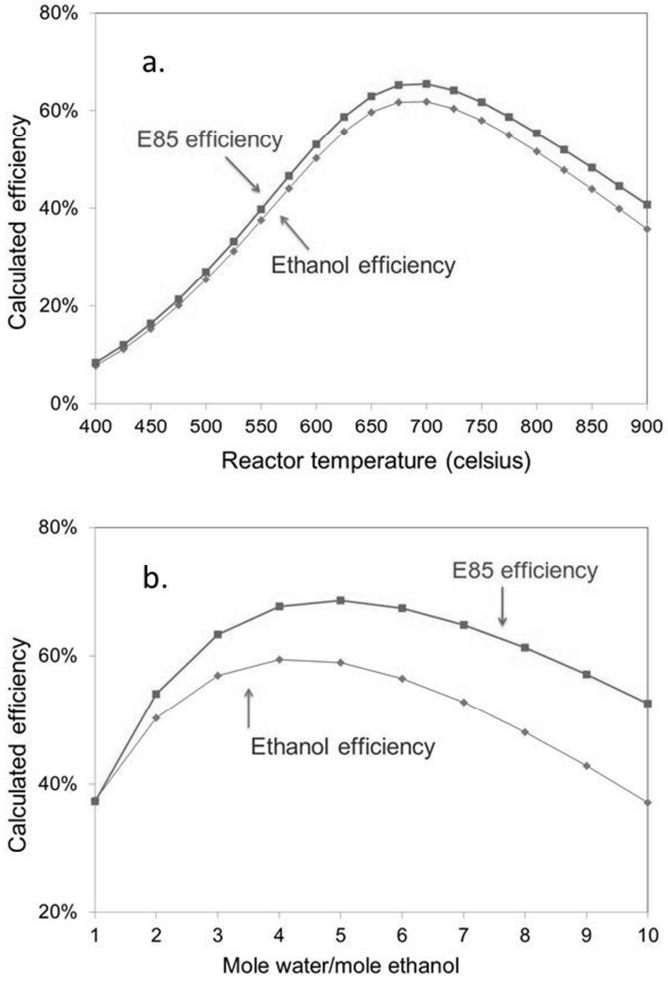

Figure 1.3: Thermodynamic efficiency a) for varying temperature at stoichiometric water/ethanol ratios and b) for varying water/ethanol ratios at 650°C

The results of our thermodynamic analysis find that hydrogen production is most efficient at moderate temperatures (650-750°C) and near-stoichiometric S/C ratios. Despite this, industrial hydrogen production is performed at temperatures above 800°C and with high concentrations of water [8, 16]. These conditions are used because the steam reforming catalyst is stable at these conditions whereas at the more energy efficient conditions the catalyst is subject to deactivation. There are many possible reasons for

catalyst deactivation at these conditions ranging from catalyst morphology changes to fouling and poisoning. A main focus of this work is to understand and quantify the different causes of deactivation occurring on a precious metal catalyst at the temperature and S/C conditions identified during the energy efficiency analysis.

1.4 Catalytic steam reforming and catalyst selection

The catalytic steam reforming of ethanol to produce hydrogen gained momentum in the late 1990's as interest in hydrogen-powered fuel cells increased. Initially, ESR was mainly reported over copper catalysts, a common catalyst for the WGS reaction [17]. Copper was found to be ineffective at breaking ethanol's carbon-carbon bond. Research shifted towards nickel, a common catalyst for natural gas reforming, as well as other base metals such as cobalt [17]. A significant amount of research has been published on nickel catalysts for ESR. Nickel catalysts produce significant amounts of coke during ESR. Surface carbon, or coke, is a common catalyst deactivation mechanism (discussed in detail in Section 2.2.2). Thus a significant portion of ESR papers with nickel catalysts have investigated methods to mitigate coke formation [18-25]. Concerns regarding the deactivation of nickel catalysts during ESR have led to more research on noble metal catalysts for this process [26-28].

Although noble metal catalysts are more expensive then base metal catalysts on a per weight basis, they frequently have higher activity and better resistance to deactivation. Therefore, noble metal catalysts can often be more economically advantageous then base metal catalysts. Rhodium was identified as a potential noble metal catalyst for ESR because it is particularly effective at cleaving ethanol's C-C bond [29-31]. Additionally, rhodium based catalysts are known to have higher resistance to deactivation from coke formation, sulfur poisoning or sintering relative to base metal catalysts [13, 32].

Recently, rhodium-containing bi-metallic catalysts have been proposed for ESR. Several authors have suggested adding nickel to rhodium catalysts in order to reduce the cost of the catalyst. Other authors have suggested Rh-Pt catalysts since platinum is known to promote the forward WGS reaction (equation 4) increasing H_2 yield and decreasing CO [33, 34]. Bimetallic Rh-Pt catalysts have also been shown to be more coke resistant that monometallic rhodium or platinum catalysts during fuel reforming [35]. Since the conditions used in this study are near stoichiometric S/C ratios where both coking and sulfur poisoning are potential deactivation mechanisms, a commercial Rh-Pt catalyst was chosen in order to reduce the susceptibility to deactivation from these mechanisms. The Rh-Pt catalyst was dispersed on a SiO_2-ZrO_2 carrier.

Catalyst carriers provide a surface to disperse the active metal particles; however, catalyst carriers can also impact catalyst selectivity and stability. For instance, during the steam reforming of ethanol it has been reported that acidic carriers such as alumina promote the dehydration of ethanol to ethylene and promote coke formation [26, 27, 30, 36, 37]. Doping an alumina carrier with potassium to neutralize acidic sites has been shown to reduce coke formation [26]. In addition to altering acid-base properties, the support can alter the electronic properties of the metal due to the interaction between the metal and the carrier. Further, the interaction between the metal and the support affects the susceptibility of the catalyst to metal sintering (the migration and agglomeration of metal particles that reduces the number of effective catalytic sites).

Zirconia is a catalyst carrier that interacts strongly with an active metal species and thus has a lower susceptibility to metal sintering. The disadvantage of using zirconia as a carrier is that is has low surface area (approximately 30-80 m^2/g). In contrast, silica has high surface area but binds weakly to metal species and thus produces low metal dispersion [38]. Pairing zirconia with silica produces a high surface area support with high metal dispersion. In this study we have used a SiO_2-ZrO_2 carrier that has a surface area of 180-200 m^2/g. Although Rh-Pt catalyst have been reported for steam reforming of ethanol and other fuels, the only published study of a Rh-

Pt catalyst supported on SiO_2-ZrO_2 was on the SR of natural gas [39]. In that study, the Rh-Pt/SiO_2-ZrO_2 catalyst was found to have good SR activity and a high sulfur-tolerance [40].

1.5 Ethanol reforming (lessons learned from the masters thesis)

Initial work on steam reforming with the Rh-Pt/ SiO_2-ZrO_2 catalyst was performed with pure ethanol. It was determined that this catalyst was very active for the ESR reaction and thus was a strong candidate to use for E85 reforming. The catalyst was able to achieve 100% ethanol conversion to equilibrium concentrations of H_2, CO, CO_2 and CH_4 at moderate temperatures (500-700°C), stoichiometric S/C, and a gas hourly space velocity (GHSV) of 20,000 h^{-1} [41] (GHSV discussed in Section 2.2.3). At these conditions the catalyst was stable for up to 100-hrs reforming pure ethanol.

In addition to these low space velocity (high conversion) conditions, a series of high space velocity (low conversion) conditions was studied. At these conditions, a kinetic rate expression for the catalyst was developed and intermediate products were identified. The rate expression had an activation energy of 85 kJ/mole [41]. The reaction order for ethanol was found to be 1.2 for water/ethanol ratios near stiochiometric conditions and 0.2 for higher water/ethanol ratios [41]. Several kinetic studies have found ESR to be first order with respect to ethanol [42-44]. However, fractional reaction orders

have been published for high water/ethanol test conditions [45, 46]. The reaction order for water was found to be near-zero which was in agreement with literature [47, 48]. Additional details on the development of the kinetic rate expression are given in Appendix B.1.

Intermediate species were identified at high space velocities (and low conversions). Product distributions at several space velocities are shown in Table 1.1. The selectivity, S_i, for each individual species was calculated according to equation 6 where the measured molar flow rate of the species in the effluent is N_i, the initial molar flow rate of ethanol is $N_{EtOH,in}$ and the molar flow rate of ethanol in the effluent is $N_{EtOH,out}$:

$$S_i = \frac{N_i}{N_{EtOH,in} - N_{EtOH,out}} \quad (6)$$

Table 1.1: Selectivity of the Rh-Pt/SiO_2-ZrO_2 monolith catalyst (washcoat loading = 0.5 g/in^3) at stoichiometric water/ethanol

High loaded catalyst							
		mole product/mole ethanol consumed					
GHSV h^{-1}	*Conversion*	*H_2*	*C_2H_4O*	*CO*	*CO_2*	*CH_4*	*C_2H_4*
50 000	*91.58 %*	*3.34*	*0.13*	*0.67*	*0.62*	*0.09*	*0.04*
100 000	*40.55 %*	*3.50*	*0.19*	*0.43*	*0.79*	*0.06*	*0.06*
200 000	*24.58 %*	*1.65*	*0.51*	*0.35*	*0.16*	*0.12*	*0.11*
Equilibrium values							
	Conversion	*H_2*	*C_2H_4O*	*CO*	*CO_2*	*CH_4*	*C_2H_4*
	100.00 %	*3.96*	*0.00*	*0.97*	*0.76*	*0.27*	*0.00*

Intermediate species included acetaldehyde, ethylene and trace concentrations of ethane. These intermediates have also been identified by other authors using a rhodium catalyst [49-51]. These species are not

chemical equilibrium products and are therefore associated with reaction kinetics.

Acetaldehyde, one of the primary ESR intermediates, typically forms on basic sites [52]. Acetaldehyde is produced via the dehydrogenation reaction (equation 7).

$$C_2H_5OH \rightarrow C_2H_4O + H_2 \quad (7)$$

$$C_2H_4O + 3H_2O \rightarrow 2CO_2 + 5H_2 \quad (8)$$

$$C_2H_4O \rightarrow CO + CH_4 \quad (9)$$

Acetaldehyde can be reformed directly to CO_2 and H_2 (equation 8) or can decompose to CO and CH_4 (equation 9). Acetaldehyde has also been shown to oxidize into acetate species which can then decompose to CH_4, CO_2 and acetone [36, 53]. It is possible that through one of these conversion mechanisms acetaldehyde can generate coke.

The other primary intermediate, ethylene, is typically formed on acid sites [52]. Ethylene is formed via the dehydration of ethanol (equation 10).

$$C_2H_5OH \rightarrow C_2H_4 + H_2O \quad (10)$$

$$C_2H_4 + H_2 \rightarrow C_2H_6 \quad (11)$$

$$C_2H_4 + 2H_2O \rightarrow CO + 4H_2 \quad (12)$$

Ethylene can be hydrogenated to form ethane (equation 11) and can also be reformed to produce H_2 and CO_2 (equation 12). Ethylene is also reported to be the most active hydrocarbon for coke formation [54].

1.6 Reforming ethanol vs E85

E85 is 15 liquid-volume% gasoline, equivalent to approximately 6 mole% gasoline. The modification of the ESR equation (equation 2) to include the additional gasoline is shown in equation 13.

$$0.94\ C_2H_5OH + 0.06\ C_8H_{18} + 3.78\ H_2O \rightarrow\ 7.14\ H_2 +\ 2.36\ CO_2\ \ \Delta H^{\circ}_{298} = 207\ \frac{kJ}{mole} \quad (13)$$

As discussed previously in Section 1.3, it was found that the thermodynamically predicted product distributions for pure ethanol and E85 reforming were similar. The experimentally measured product distributions were also similar. The differences in the product distribution predicted by thermodynamics and measured experimentally are shown in Figures 1.4a and 1.4b respectively.

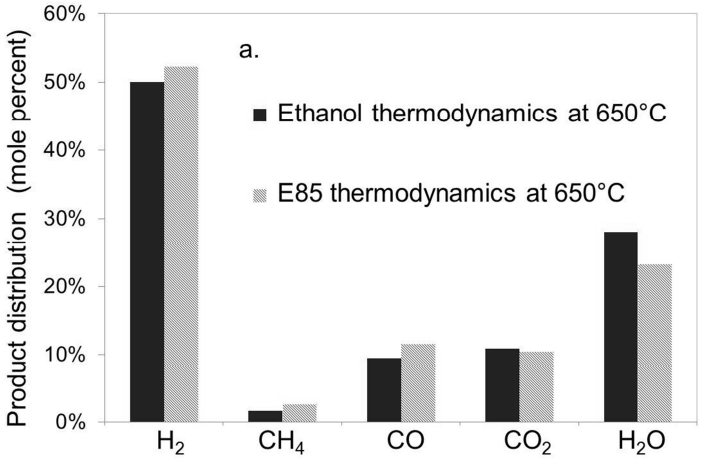

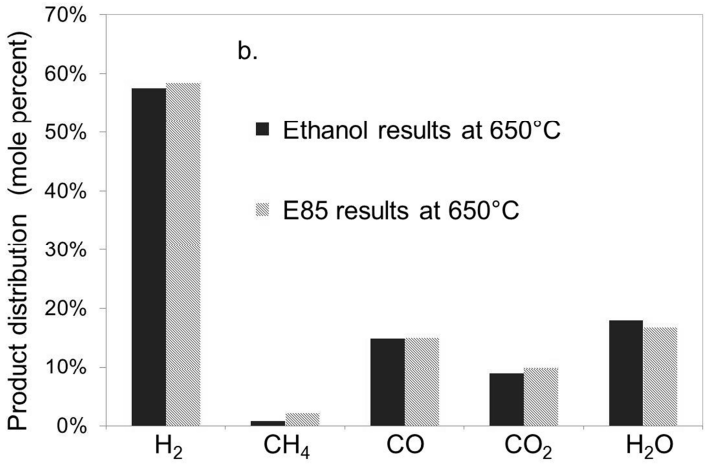

Figure 1.4: a) Thermodynamically predicted product distribution for stoichiometric S/C at 650°C and b) Experimentally determined product distribution for stoichiometric S/C at 650°C using Rh-Pt/SiO_2-ZrO_2 washcoated monolith (2.0 g/in^3) and GHSV = 22,000 h^{-1}

During the ethanol and E85 steam reforming, the experimentally measured concentrations of methane and water are lower, and the experimentally measured concentrations of carbon monoxide and hydrogen are higher than those expected by thermodynamics. This may indicate that the CO methanation reaction (equation 14) has not reached equilibrium.

$$3H_2 + \mathrm{CO} \rightarrow CH_4 + H_2\mathrm{O} \quad (14)$$

The comparison of E85 and ethanol steam reforming demonstrates that the addition of the higher hydrocarbons did not contribute significantly to the process efficiency (Section 1.3), nor to the predicted or experimental determined product distributions. Although the addition of gasoline did not significantly change catalyst activity or selectivity, as demonstrated in future sections, it did significantly impact catalyst stability.

1.7 Thesis aim and organization

A major challenge in steam reforming liquid transportation fuels is catalyst deactivation. This is particularly true for commercial fuels that contain catalyst poisons such as sulfur and have higher hydrocarbons that can increase coke formation. Since steam reforming is performed on commercial fuels, such as E85 or natural gas, catalyst deactivation dictates that less energy efficient conditions with larger amounts of steam or higher temperatures are used in the reformer to avoid deactivation. The goal of this work is to develop a steam reforming process that can operate at more energy efficient conditions despite the use of a commercial fuel.

In Chapter 2, a review of the literature on catalyst stability during steam reforming of liquid fuels is presented. Catalyst stability studies performed during either ethanol or E85 reforming are reviewed. Afterward, some of the common deactivation mechanisms that impact catalysts: sulfur poisoning, coke formation, carrier sintering, and metal sintering, are discussed and reported instances of these mechanisms impacting steam reforming catalysts are reviewed.

The third chapter summarizes the experimental methodology used in the work presented in subsequent chapters. The methods used to prepare, test and characterize the catalysts are described.

In the fourth chapter, the stability of the catalyst during steam reforming of ethanol and sulfur-free E85 is investigated. Significant catalyst deactivation was measured during the steam reforming of the sulfur-containing fuel. The catalyst stabilized at an activity and selectivity level that is unacceptable for industrial hydrogen production. This chapter illustrates the need to incorporate regenerations into a process reforming sulfur-containing fuels with this catalyst.

In the fifth chapter, the potential for catalyst regenerations to sustain stable performance at energy efficient conditions is investigated. It is found that after deactivation catalysts can be regenerated with air treatment to initial activity but subsequent deactivation is more rapid. Three possible hypotheses were proposed for the irreversibility: that residual sulfur was not removed during regenerations, that refractory coke was not removed during regeneration, or that an additional deactivation mechanism such as metal or carrier sintering was occurring. The succeeding chapters investigate these hypotheses.

Chapter 6 investigates the impact of sulfur on catalyst performance and the reversibility of sulfur poisoning. Chapter 7 investigates the type of coke that forms on the catalyst and its regenerability with air treatment. Chapters 8 and 9 investigate additional deactivation mechanisms that may change the catalyst chemistry or morphology and cause the irreversible

deactivation identified in Chapter 5. Carrier sintering or segregation of the mixed-oxide carrier is investigated in Chapter 8. Precious metal sintering is investigated in Chapter 9. Finally, in Chapter 10, conclusions and recommendations for future work are discussed.

Chapter 2 : Literature review

Although a significant body of literature exists on the deactivation of catalysts during fuel reforming, there has been only one reported study on the reforming of E85. The literature on the stability of catalysts during ethanol reforming is also limited. This chapter begins with a review of these studies. The bulk of this chapter reviews stability studies on steam reforming of other sulfur-containing fuels. The primary deactivation mechanisms that are identified are: sulfur poisoning, coke formation, metal sintering, and support sintering. Studies pertaining to each of these mechanisms are reviewed. Additionally, reports on the reversibility of each mechanism are reported.

2.1. Catalyst deactivation studies during ethanol or E85 reforming

The literature on ESR primarily focuses on identifying active and selective catalysts for the reaction. However, several studies have investigated the stability of both base metal and precious metal catalysts during ESR. The most commonly reported cause of deactivation during the endothermic process is coke formation. Although coke formation is not thermodynamically predicted at or above stoichiometric S/C, both base metal [18-20, 22, 23] and noble metal [33, 36, 55, 56] catalysts have been found to

generate stable surface carbon species at these conditions. Increasing either S/C or bed temperature can decrease the susceptibility of the catalyst to coking.

Another factor that affects the amount of coke formation during ESR is the selectivity of the catalyst to ethylene. As discussed in Section 1.5, ethanol is dehydrated to ethylene on acidic sites. It is well documented that alumina, an acidic carrier, promotes the production of ethylene. Further, it has been shown that decreasing the acidity of the carrier with promoters can reduce coking [26, 57]. In addition to changing surface acidity by modifying the catalyst formulation, it has been reported that ethylene formation can be minimized by adding basic compounds to the reactants. For instance, the addition diethylamine was shown to improve the stability of a $Rh/MgAl_2O_3$ catalyst during ESR whereas the addition of acidic compounds such as acetic acid were found to decrease stability [58]. Therefore, carrier formulation as well as the presence of impurities in the fuel can impact catalyst stability during ESR.

Stability studies during ESR have mainly used 100% pure ethanol rather than ethanol that contains impurities such as either bioethanol (the product of fermentation) or ethanol/gasoline blends (common transportation fuels). Both of these commercial ethanol fuels contain sulfur. However, only one paper was identified on sulfur induced deactivation during ESR.

Yamazaki et al studied the reforming of bioethanol, a primarily ethanol/water mixture that contains low levels of sulfur [59]. The authors reported that a Pt/ZrO_2 catalyst was not stable during the reforming of bioethanol and attributed deactivation to the sulfur-containing impurities.

2.2. Potential deactivation mechanisms during steam reforming

2.2.1. Sulfur poisoning

A major challenge in steam reforming liquid transportation fuels is catalyst deactivation due to sulfur poisoning. Sulfur binds strongly with catalytically active sites rendering them inactive [60, 61]. As discussed in Section 1.3, reforming sulfur-containing fuels is typically performed at less energy efficient conditions (high temperatures and high water/fuel ratios) to reduce the susceptibility of the catalyst to coke and sulfur-induced deactivation. As a result, very few papers have been published on the reforming of sulfur-containing fuels at moderate temperatures (500-700°C) and low S/C ratios. At these conditions most studies reform sulfur-free fuels or perform ATR rather than SR of sulfur-containing fuels. In addition, most of these ATR papers have studied sulfur impacts by adding a single sulfur-compound (such as H_2S) to a model fuel compound (such as n-hexane) rather than reforming a commercial fuel that contains a large array of sulfur

compounds. Thus there are limited studies on the reforming of sulfur-containing commercial fuels at conditions where deactivation is likely to occur.

The only published paper on the steam reforming of E85 (containing sulfur) used high temperatures (800-900°C) and high water/fuel ratios (6:1) with a Rh/Ceria catalyst. At these conditions no deactivation was observed [62]. In contrast, we have reported that a Rh-Pt/SiO_2-ZrO_2 catalyst deactivates at 650°C and near stoichiometric water/fuel ratios [63]. Therefore, the only two published studies on E85 reforming illustrate the dependence of catalyst stability on temperature and water/fuel ratio.

Both studies performed on E85 reforming used noble metal rather than base metal catalysts. In agreement with thermodynamics, noble metal catalysts have proven more sulfur-tolerant than base metal catalysts [13]. Thus, a majority of studies on reforming sulfur-containing fuels have used precious metals or precious metal-containing bi-metallic catalysts. Although these catalysts are more stable than base metal catalysts, the sulfur impacts are typically lessened rather than eliminated. For instance, Strohm et al studied steam reforming of jet fuel at moderate temperatures (520°C) and near stoichiometric S/C ratios with a bimetallic Rh-Ni catalyst on CeO_2-modified Al_2O_3 and found that the Rh-Ni catalyst was stable until a S_{surf}:Rh_{surf} ratio of 0.28 was reached [32].

In addition to binding strongly with active sites, sulfur can also catalyze other deactivation mechanisms such as coking or metal sintering. Sulfur-promoted coke formation has been reported in both ATR and SR studies. Lakhapatri et al found that sulfur promoted coke formation during n-hexadecane reforming with a Rh-Ni/Al_2O_3 catalyst [64]. Utilizing the same catalyst, Xie et al determined that sulfur increased carbon deposition during the reforming of Norpar (a mix of alkanes) with 3-MBT (*3*-methylbenzothiophene) as a sulfur additive [65]. This phenomenon has also been reported during ATR or SR with monometallic Rh [66-71] and platinum catalysts [59, 72].

Several authors have found sulfur poisoning to be partially or fully reversible. For example, Lausche et al found that deactivation of a Mo_2C catalyst during methanol SR with 5-ppm sulfur was fully reversible by removing sulfur from the feed [73]. However, the authors found that sulfur poisoning was not reversible on a Pt/Mo_2C catalyst [73]. In another study, Ferrandon et al reported that initial activity of a Rh/La-Al_2O_3 catalyst during ATR of 34-ppm gasoline could be recovered by switching to a sulfur-free fuel at 800°C [74]. However, the authors found that the catalyst regained only 50% of initial activity when this procedure was performed at 700°C [74]. Similarly, Cheekatamarla et al found that during ATR of synthetic diesel (at 400°C), activity of a Pt/CeO_2 could be partially recovered by switching to a

sulfur-free fuel [75]. Thus, both the catalyst formulation and the conditions are factors in determining whether sulfur-poisoning is reversible.

The reversibility of sulfur poisoning has also been reported for other applications, specifically the WGS reaction. Xue et al. found that 200 ppm H_2S poisoned a Pt/ZrO_2 catalyst (resulting in conversion changes from 44% to 12%), however, deactivation could be fully reversed by removing sulfur from the feed [76]. The authors found that sulfur poisoning was more permanent on other catalysts including Cu–Zn, Co–Cr. In another WGS study, Farrauto et al found that a Pt-Re catalyst was irreversibly deactivated by sulfur whereas a Pt-only catalyst was reversibly deactivated [40]. As discussed previously, sulfur poisoning may also catalyze other deactivation mechanisms such as coking or sintering. Thus, in some cases, sulfur adsorption may be reversible but other deactivation mechanisms that it promotes may not be.

The previously reviewed studies indicate that under certain conditions, and with certain catalysts, removing sulfur from the reactants reverses sulfur poisoning. However, in cases were sulfur adsorption is not reversed by the removal of sulfur from the reactants, treatment of the catalyst with oxygen, steam or hydrogen may also be effective at removing sulfur from the surface. Rostrup-Nielsen et al demonstrated that a Mg or Ca promoted Ni catalyst could be partially regenerated by treating it with steam at 700°C [77]. In this study the reversibility of sulfur poisoning on the $Rh\text{-}Pt/SiO_2\text{-}ZrO_2$

will be investigated with two methods: by removing sulfur from the reactant feed and by treating the catalyst with an oxidizing regeneration treatment.

The catalyst formulation used for this study was specifically chosen for its sulfur-tolerance. Rhodium and platinum have been found to be more resistant to sulfur poisoning than other noble metals such as rhenium or palladium [8]. The support was also chosen for its sulfur-tolerance; both silica [78] and zirconia [79] have been identified as sulfur-tolerant carriers. Further, the Rh-Pt/SiO_2-ZrO_2 catalyst used in this study has already demonstrated good sulfur tolerance during steam reforming of natural gas [39, 40]. The extent of deactivation was less than with other noble metal catalysts and the deactivation was fully reversed when sulfur was removed from the reactants [40].

2.2.2. Coke formation

In chapter 2 we determined that carbon formation is catalyzed by the presence of sulfur but also forms during sulfur-free E85-SR. Coke is likely formed through one of the following mechanisms [80]:

$$2CO \leftrightarrow C_s + CO_2 \ \ (Boudouard\ reaction) \qquad (15)$$

$$CO + H_2 \leftrightarrow C_s + H_2O \qquad (16)$$

$$CH_4 \leftrightarrow C_s + 2H_2 \qquad (17)$$

$$C_nH_{2n+2} \leftrightarrow nC_s + (n+1)H_2 \qquad (18)$$

In SR, the amount of coke formation is determined by both the rate of coke formation and rate of coke removal. Reactions 15-18 above are reversible [80]; thus increasing H_2O concentrations can reduce coking by increasing the steam gasification rate (backwards reaction of 16). In addition to a dependence on steam concentration, this rate is also dependent on the reactivity of C(s). Coke species range from reactive, amorphous forms to less-reactive, more refractive (graphitic) forms. The form of the coke species is a function of reactor temperature, feed content, and contact time. Time on stream can also impact the form, specifically the degree of dehydrogenation, and thus reactivity of the carbon [64].

There are several different types of coke that can form on a catalyst during steam reforming. Different types of coke have different degrees of hydrogenation and reactivity. Factors such as S/C, temperature and TOS can influence the type of coke that is formed on the catalyst [80]. For instance, weakly adsorbed atomic carbon can form carbides during TOS becoming more difficult to remove [8]. However, coke most commonly deactivates the catalyst by 'fouling.' Fouling is the process of species condensing on the catalyst surface, covering active sites and plugging pores [38]. Fouling is typically caused by adsorbed CH_x species that polymerize to form carbon films [8]. Surface carbon species can also become increasingly dehydrogenated forming

graphitic coke [8, 60]. Graphitic coke can encapsulate active sites and is harder to remove then more amorphous forms [8, 60].

Regeneration of coked catalysts is typically achieved by oxidizing or gasifying the carbonaceous deposits with air, O_2 or H_2O although CO_2 and H_2 can also be potential methods [8]. The minimum temperature required to remove coke deposits is a function of the type and location of the coke and the atmosphere used during the regeneration. More graphitic forms of coke may require temperatures up to 900°C to fully oxidize [8].

Although catalyst regeneration is a common industrial technique it is rarely reported on in the ESR literature. We have identified only two papers that discuss the regeneration of a deactivated catalyst after ESR. In one of these two studies, a Co/SiO_2 catalyst with and without the addition of Rh or Ru was regenerated after oxidative reforming of ethanol at 350-400°C [81]. The authors found that air exposure removed coke and restored performance of bimetallic $Rh\text{-}Co/SiO_2$ and $Ru\text{-}Co/SiO_2$ catalysts but did not regenerate a Co/SiO_2 catalyst. Thus, they found that oxidative treatment was successful at restoring activity with the precious metal and not the base-metal catalyst. This study, did not look at significant levels of deactivation (less than 90% conversion) nor significant periods of TOS (more than 5-hrs). In the other study, Wanat et al found that air treatment was effective at removing coke from a Rh/Al_2O_3 and $Rh\text{-}Ce/Al_2O_3$ catalyst after ESR at low S/C ratios (1:1)

and high temperatures (800°C). However, the authors reported that only partial activity was returned following air treatment and the regenerated catalyst accumulated coke more rapidly during successive reforming segments [82].

The study by Wanat et al demonstrates that catalyst regeneration can sometimes restore some but not all of the catalyst's initial activity. This behavior has been reported in the reforming literature (for fuels other than ethanol). In a paper on dry reforming (CO_2/CH_4), Bitter et al found that a Pt/Al_2O_3 catalyst could be regenerated to initial activity by removing carbon with air treatment at 400°C [83]. However, deactivation rates following the regeneration treatment were higher than initial deactivation rates [83]. These results imply that regenerations are only partially effective, or that the regeneration condition detrimentally impacts the catalyst. For instance, high surface temperatures during regenerations may lead to thermal degradation of the catalyst [84].

2.2.3. Carrier deactivation mechanisms

Catalyst carriers are typically porous, high surface area materials that provide good dispersion of active catalyst particles. Thus, one of the most common deactivation mechanisms to afflict the carrier is carrier sintering, whereby the carrier surface area is diminished. This process can collapse

catalyst pores decreasing the availability of the active metal. Temperature-induced phase changes are frequently responsible for such behavior. For instance, γ-Al_2O_3, a common carrier in automotive catalysis becomes α-Al_2O_3 at high temperatures leading to severe losses in surface area [38]. In this study, SiO_2, a high surface area support is utilized. Although SiO_2 suffers from low thermal stability, ZrO_2 has been found to stabilize the catalyst against sintering at high temperatures [85]. In a study by Deeba et al a 25% ZrO_2/SiO_2 carrier, similar to the one used in this study, displayed no change in surface area during 70-hrs of treatment in air at 800°C [85]. Regaining carrier surface area is rarely possible; however, certain promoters such as La_2O_3, BaO, and ZrO_2 can retard sintering rates at high temperatures.

As discussed in Section 1.5, the catalyst carrier can play an important role in the selectivity of the catalyst. Thus, changes to the carrier chemistry can have implications for catalyst selectivity and the likelihood for coke formation. It has been demonstrated that segregation of SiO_2-ZrO_2 carriers can occur at temperatures between 700-1000°C [86-88]. The acidity of mixed SiO_2-ZrO_2 oxides is different than the acidity of the individual oxides [89]. Thus, segregation of the SiO_2-ZrO_2 carrier is another potential deactivation mechanism that is investigated in Chapter 8.

2.2.4. Precious metal sintering

Metal sintering is the process of metal particles migrating and coalescing to form larger particles. This process reduces the surface to volume ratio of the precious metal particles decreasing the number of accessible precious metal sites. Metal sintering happens by several different processes including: crystallite or atomic migration along the surface or, in the case of high temperature processes, vaporization and re-capture of the metal by other particles. Higher temperatures increase both the surface diffusion rate and vaporization of the catalytic metal; therefore, temperature strongly affects the degree of metal sintering. The gaseous environment also affects the sintering rate. For instance, higher partial pressures of steam have been shown to increase sintering rates of industrial nickel reforming catalysts [61]. Oxidative environments have also been found to sinter catalysts more so than N_2 or H_2 environments [60, 90, 91].

Sintering is more frequently reported during ATR then during SR due to the high surface temperature "hot-spots" that can occur on the surface in ATR. Sintering of precious metal catalysts during ATR has been reported during ethanol ATR [92] and gasoline ATR [68, 93]. Thus, in this study it is possible that sintering may occur during the oxidative regenerations which may produce high temperatures on the catalyst surface. In Chapter 9, the

impact of reforming conditions and regeneration conditions on the morphology of the metal particles is investigated.

Metal sintering is frequently considered an irreversible deactivation mechanism; however, re-dispersion methods have been reported. Wang and Schmidt reported that smaller rhodium particles could be formed on a SiO_2 support by first treating the catalyst with oxygen at 600°C and then hydrogen at 400°C [94]. Treating catalysts with oxy-chlorination has also been shown to improve metal dispersion [95]. Promoters can increase or decrease metal sintering rates [8].

2.2.5. Additional deactivation mechanisms

In addition to the deactivation mechanisms described previously, more complex mechanisms that affect the interfacial boundary between the metal and the carrier can occur. One of these mechanisms is strong metal support interaction (SMSI) between the carrier and the precious metal. SMSI typically occurs between a precious metal and a reducible oxide support in high temperature reducing environments [96]. SMSI lowers the chemisorption capacity of the active metal, therefore, the behavior is most often characterized by discrepancies between H_2 or CO chemisorption predicted particle sizes and actual particle sizes measured by imaging technique such as TEM [96]. SMSI can also be characterized by the binding

energy of the precious metal, for instance, SMSI rhodium is characterized by a binding energy of approximately 310 eV whereas the binding energy of typical rhodium metal is 307-307.3 eV and the easily reducible oxide is 308.6-109.4 eV [97].

There is a lot of variation in the literature on the mechanism that causes SMSI, the carriers that can exhibit SMSI, and the impacts of SMSI on catalyst performance [98]. The most commonly reported mechanism for SMSI is decoration of the active metal with the support [99]. Other authors have referred to encapsulation or burrowing of the active component into the carrier as SMSI. Some studies report enhanced catalyst stability due to SMSI because it maintains dispersion at high temperatures [99, 100] while other studies report that SMSI diminishes activity by reducing the activity of the active metal [101, 102]. Thus, SMSI can be a benefit or a detriment to performance depending on the catalyst formulation, the desired selectivity and the reaction conditions.

In the typical definition of SMSI (metal decoration), it is reported on supports such as TiO_2 [103-106] and CeO_2 [101, 102, 107]. However, several authors have reported encapsulation as SMSI. Encapsulation of Rh, Pt, or Rh-Pt by zirconia has been reported [35, 79, 108, 109]. Traditional SMSI behavior (metal decoration) can be reversed by performing low temperature reduction (typically at 400°C) followed by oxidation [101, 103, 106]. However,

other changes to the catalyst-carrier interface, such as encapsulation are more difficult to reverse. In Chapters 8 and 9, changes to the catalyst carrier and the precious metal are studied. From these investigations information on the interfacial boundary may also be discerned.

Chapter 3 : Experimental Methodology

3.1. Catalyst preparation

A commercially available 3%Rh-1%Pt/SiO_2-ZrO_2 reforming catalyst (BASF catalysts, LLC) was used for all catalytic tests. Catalyst preparation was done at the BASF facilities in Iselin, NJ. The catalyst was prepared by depositing an aqueous solution of the catalyst precursors onto the SiO_2-ZrO_2 carrier via incipient wetness. The catalyst precursor salts are proprietary BASF formulations. After impregnation, a 25% solid slurry was created and ball milled to generate particle sizes less than 10 μm. Subsequent preparation varied for monolith and particle bed tests. Both catalyst particles and washcoated monoliths were used in reactor studies.

Washcoated monoliths were used to study catalyst performance at realistic process conditions. Monoliths produce low-pressure drops and efficient heat transfer and thus are used in most environmental catalytic processes [40]. The cordierite ($2MgO–2Al_2O_3–5SiO_2$) monoliths were supplied by Corning Inc. and had a cell density of 400 cells/in^2. Monoliths were coated with catalyst slurry, dried at 120°C for 2-hrs and calcined at 550°C for 2-hrs. Two catalyst washcoat loadings were prepared: 2.0 g/in^3 and 0.5 g/in^3. The extent of loading was measured wet as a preliminary measure of loading and again after drying and calcination. Multiple coatings were performed to

achieve the desired loading. Monoliths were cored to have an external diameter of 0.75 in. The axial length for the high loaded catalysts was 1.0 in. and 0.25 in. for the low washcoat loading.

For certain reactor studies, a particle bed (packed bed) was used to facilitate easier characterization of spent catalysts. To produce the catalyst particles, the catalyst slurry (10 μm particles) was dried at 120°C for 2-hrs and calcined at 550°C for 2-hrs to generate the catalyst powder. The powder was pressed into 12 mm diameter pellets (4000 psi, 4 min), crushed and sieved to 600-700 μm. The particle size for the packed bed was chosen by considering pressure drop through the bed and diffusion limitations of larger particles. This analysis is shown in Appendix B.3. The bed consisted of 250 mg catalyst and 750 mg quartz diluent. The quartz particles were also 600-700 μm. The bed size was 0.75 in diameter and 0.5 in long.

3.2. Reactor tests

In the following chapters, three types of stability tests are performed: the stability of the catalyst during pure ethanol reforming, the stability of the catalyst during sulfur-free E85 reforming, and the stability of the catalyst during sulfur-containing E85 reforming. One reactor was used for each of these tests with slight modifications for the different fuels. The schematic of this reactor is shown in Figure 3.1. During ethanol reforming the syringe

pump was not used. For tests SR with the commercial E85 (28 ppm sulfur) the entire fuel composition was injected by syringe pump and the HPLC pump was used for water.

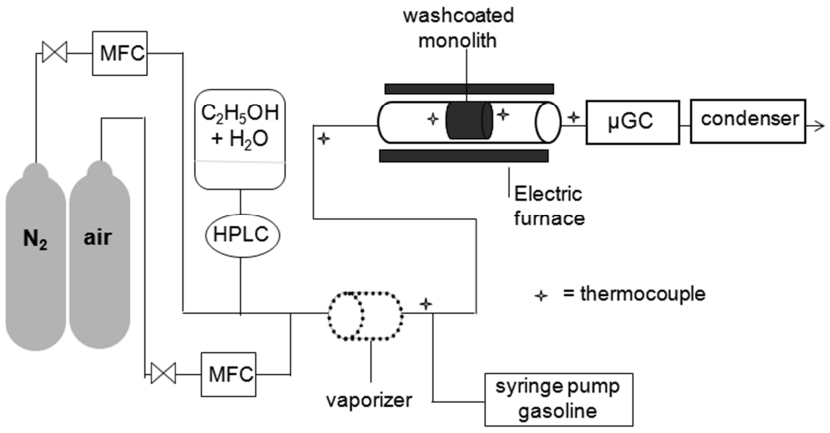

Figure 3.1: Reactor schematic for washcoated monoliths

Modifications were also made for the packed bed reactor tests. Unlike the reactor in Figure 3.1, the packed bed was a vertically aligned reactor with upward flow. Two quartz frits held the packed bed in place.

The reactor effluent was measured with an Agilent 3000 micro-GC (Gas Chromatograph) with the following columns: a molecular sieve column for measuring H_2, O_2, N_2, CH_4, and CO; a PlotQ column for measuring CO_2, C_2H_4, C_2H_6, H_2O as well as other larger hydrocarbons, an OV-1 column for measuring species including: H_2O, C_2H_5OH, $(CH_3)_2CO$ and C_2H_4O and an Innowax column for measuring species including H_2O, C_2H_5OH, and C_2H_4O. The GC was equipped with inlet heaters and therefore able to measure room-temperature liquid products like ethanol and water. These measurements

allowed for accurate ethanol conversion and full product distribution measurements.

The capability of the GC to measure all species online (without condensing out room temperature liquid species) allowed for full atom balances (for H, C and O) to be performed for every test. Ultra high purity (UHP) nitrogen (99.999% purity) was used as an internal standard to establish the molar flow rate and carry out atom balances. The product distributions of all tests were normalized for nitrogen content. Lastly, the online measurement of water and ethanol allowed for bypass tests to verify that the proportion of fuel, water, and nitrogen in the feed were correct; this was an important validation of the flow systems and overall set-up.

In previous work we reported the decomposition of ethanol on the walls of a stainless steel reactor [41]. To avoid this, all tests were performed in a quartz tube reactor. The reactor was heated with an electric furnace and the temperature was monitored by Omega K-type thermocouples placed ¼ in upstream and downstream from the catalyst bed. Heat balance calculations were performed by comparing the measured temperature difference between the inlet and outlet thermocouples with an adiabatic temperature differential based on the enthalpies of the products at the outlet temperature.

3.2.1. Test conditions

For monolith tests, several different test conditions were used. These conditions were defined by the gas hourly space velocity (GHSV) and the amount of precious metal catalyst washcoated on the monolith. The GHSV is defined according to the equation 19:

$$GHSV = Q/V \quad (19)$$

where Q is the total gaseous flow rate and V is the bed volume. During monolith deactivation tests, catalyst deactivation was measured at different GHSV conditions and different washcoat loadings. During packed bed conditions, only the time on stream (TOS) and the time between regenerations was varied. The test conditions are summarized in Table 3.1.

Table 3.1: Summary of test conditions for monolith and particle bed tests

Monolith test conditions		GHSV h^{-1}	washcoat loading (g/in^3)	total catalyst weight (g)
1	process condition	22,000	2.00	0.63
2	high deactivation condition	22,000	0.50	0.05
3	high GHSV condition	44,000	0.50	0.05
Particle test condition		**GHSV h^{-1}**	**quartz/catalyst (wt ratio)**	**total catalyst weight (g)**
4	particle test	22,000	3:1	0.25

At each contact time a steam/carbon (S/C) ratio of 1.8 was maintained (stoichiometric steam/carbon ratio is 1.6 for E85 and 1.5 for pure ethanol). Tests were all conducted with inlet temperatures at or near 650°C.

In Chapter 5, catalyst regeneration is investigated. Except as noted, regenerations were performed with 50% air/50% N_2 at 650°C. The flow rate was equivalent to the total flow used during reforming conditions (thus the monolith GHSV was maintained).

3.2.2. Reactants

The catalyst's stability was measured during reforming of several different fuels, each shown in Table 3.2 with associated ethanol and sulfur content. The ethanol used in fuels 1-4 was 99.99% purity purchased from Sigma Aldrich. Isooctane (99.99% purity) from Sigma Aldrich was used as a surrogate for gasoline in a synthetic E85 (fuel 2). An additional sulfur-free E85 fuel (fuel 3) was prepared using 15 liquid volume% sulfur-free gasoline provided by Conoco Chevron.

Table 3.2: Fuels used during reactor tests with associated ethanol and ppm sulfur content (mg/kg)

	Fuels tested	*% Ethanol (liq vol%)*	*sulfur ppm (mg/kg)*
1	Ethanol	100	0
2	85% Ethanol, 15% Isooctane	85	0
3	85% Ethanol, 15% sulfur-free gasoline	85	0
4	85% Ethanol, 15% commercial gasoline	85	5
5	Commercial E85	85	28

Two sulfur-containing fuels were studied: a commercial grade E85 with 28 ppm sulfur, and a simulated E85 made by combining 85 liquid volume% ethanol with 15% liquid volume commercial gasoline. The commercial gasoline contained 32-ppm sulfur and therefore the simulated E85 had a total sulfur concentration of 5-ppm. Both the E85 and the gasoline were purchased from a local service station. The sulfur content of each fuel was determined by X-Ray Flourescense (by Herguth Laboratories using ASTM D4294). A large array of sulfides and thiols were identified in the gasoline; in agreement with other reported analyses of gasoline [110]. The results of the sulfur analysis are detailed in Appendix A.1.

3.3. Catalyst characterization

3.3.1. TPO

Temperature programmed oxidation (TPO) of spent particle catalysts were performed with a Quantachrome ChemBET Pulsar instrument equipped with a thermal conductivity detector (TCD). An Agilent MicroGC-3000 was connected to the ChemBET to measure the concentrations of individual species (CO_2 and H_2O). Prior to each test, samples were pre-dried at 140°C for 1-hr. After drying, samples were cooled to 40°C in UHP He. TPO experiments were performed in 80 mL/min oxygen flow (5%O_2/He) with a heating rate of 7°C/min to 1000°C.

TPO of spent monolith catalysts were performed with thermogravimetry analysis (TGA) and differential thermoanalysis (DTA) coupled with Mass Spectrometry (MS). A TGA–DTA/DSC apparatus (Netzsch STA 409 PC Luxx) measured changes in mass during a 5°C/min temperature ramp from 25°C to 900°C in 80 mL/min of 50% air, 50% N_2. The effluent of the TPO tests was analyzed with an Agilent 5973 MS. The amount of CO_2 was measured to determine the total carbon on the surface. SO_2 was not detectable in the effluent during these tests, thus total sulfur could not be quantified. Sensitivity tests were run to determine the detection limit of SO_2. These tests are discussed in Appendix B.2.

3.3.2. ICP

Inductively Couple Plasma Atomic Emission Spectrometry (ICP-AES) sulfur analysis was completed with a Perkin Elmer 2001 DV ICP spectrometer after acid digestion with $HClO_4$ and HF. These tests were conducted at the BASF facilities in Iselin, NJ by Sharon Walsh.

3.3.3. TGA H_2S adsorption studies

Isothermal TGA H_2S adsorption studies were performed with a Netzsch STA 409 PC Luxx at 450, 650, or 850°C. UHP nitrogen was used as a purge and protective gas for all tests. Samples were pre-dried at 140°C for 1-hr and pre-reduced at 450°C for 1-hr in 4% H_2/N_2. During adsorption segments, the catalyst was exposed to 5 ppm H_2S/N_2 with gas flow rate 80 mL/min. Desorption was measured with either 100% UHP N_2 segments (at various temperatures) or with 40% H_2/N_2.

3.3.4. XPS

X-ray photoelectron spectroscopy (XPS) was performed with a Thermo Fisher K Alpha instrument equipped with Al K (alpha) monochromatic source. Intact washcoated monolith sections were removed from the radial center of the sample and were taken both from the inlet and outlet end of the monolith. Samples were mounted on carbon tape for analysis. Washcoat

samples were scraped from the monolith, ground with a mortar, and placed on double sided tape for analysis. The run conditions were as follows: pass energy = 40 eV (high resolution analysis) and pass energy = 150 eV for low resolution survey scan analysis. Vacuum conditions were 9×10^{-8} torr or better and spot size = 400 µm with 90° analyses angle. Data was analyzed using Thermo Fisher Avantage software and Scofield sensitivity factors [111]. Binding energies were referenced to the ubiquitous C1s = 285.0 eV.

3.3.5. XRD

The crystalline structure of catalysts was obtained by X-ray diffraction (XRD). XRD patterns were recorded in the range of $2\theta = 10–120°$ with a step size of 0.017 on an INEL diffractometer at room temperature with Cu Kα radiation (1.78897 Å). Additional details on XRD methods are discussed in Appendix D.

3.3.6. TPR

Temperature programmed reduction (TPR) profiles of fresh or spent catalysts were obtained under hydrogen flow (5%H_2/Ar) by using the Quantachrome ChemBET Pulsar instrument. Catalyst samples of 25-30 mg were analyzed using TPR-H_2. Prior to the TPR tests, samples were pre-dried at 140°C for 1-hr. After drying the catalysts were cooled to 40°C in UHP He.

The TPR-H_2 profiles were registered by heating the samples from 25 to 800°C at a rate of 7°C/min. Gas separation and monitoring was performed with an Agilent MicroGC-3000 to obtain profiles of H_2 consumed and H_2O produced during the test. The gas flow rate was 80 mL/min for all test segments.

3.3.7. CO Chemisorption

Active metal dispersion measurements were performed by CO-chemisorption experiments on a Quantachrome ChemBET Pulsar instrument. The catalyst was pre-dried in N_2 at 120°C for 2-hrs and subsequently reduced in 4%H_2/N_2 at 400°C for 2-hrs. The adsorption measurements were performed at room temperature. The dispersion of precious metal was calculated from the total CO uptake by assuming a chemical adsorption stoichiometry of CO:PM = 1.

3.3.8. TEM

Transmission electron microscopy (TEM) images were collected with a Zeiss electron microscope EM 902 at the City College of New York with the help of postdoctoral researcher Antonio Sanchez. Precious metal particle size distributions were measured manually utilizing at least 15 images and 150 particles.

3.3.9. BET surface area

Dynamic, single-point BET surface area was measured using a Quantachrome ChemBET Pulsar instrument. Approximately 100 mg of sample was pre-dried at 130°C for 2-hrs in 100% N_2. Nitrogen was condensed on the sample in 100 mL/min 30% N_2/He flow at approximately -200°C and subsequent N_2 desorption (in 100% He) was measured by TCD and integrated to determine surface area. The surface areas found were similar to those reported in the literature for SiO_2-ZrO_2 catalysts [112].

Chapter 4 : Catalyst stability during fuel reforming

The goal of this chapter is to determine and quantify the stability of the catalyst during steam reforming of commercial E85. The conditions utilized are the energy efficient conditions identified in Section 1.5: near stoichiometric S/C ratios and temperatures of 650°C. In order to isolate the impact of the higher hydrocarbons in the E85 on catalyst stability, the catalyst's performance while steam reforming pure ethanol and sulfur-free E85 is compared. In order to isolate the impact of sulfur on catalyst stability, the catalyst's performance while steam reforming a sulfur-free and sulfur-containing E85 is compared.

4.1. Reforming pure ethanol: the impact of space velocity on stability

As a foundation for future investigations on the stability of the catalyst during E85 reforming, catalyst stability tests were conducted with pure ethanol using a washcoated monolith. The Rh-Pt/SiO_2-ZrO_2 catalyst was stable during 24-hrs of continuous operation reforming pure ethanol at the low space velocity condition (S/C = 1.8, GHSV = 20,000 h^{-1}, washcoat loading = 2.0 g/in^3). Further, the catalyst was stable in non-continuous conditions (including start-ups and shut downs) for over 100-hrs at these conditions. No change in conversion, product distribution or monolith outlet temperature

was measured during these tests. In order to measure deactivation, the washcoat loading was lowered and the GHSV was increased. At these conditions (S/C = 1.8, GHSV = 44,000 h^{-1}, washcoat loading = 0.5 g/in^3) the catalyst deactivated immediately upon introduction of reactants. In Figure 4.1, the product distributions for the two GHSV tests are compared.

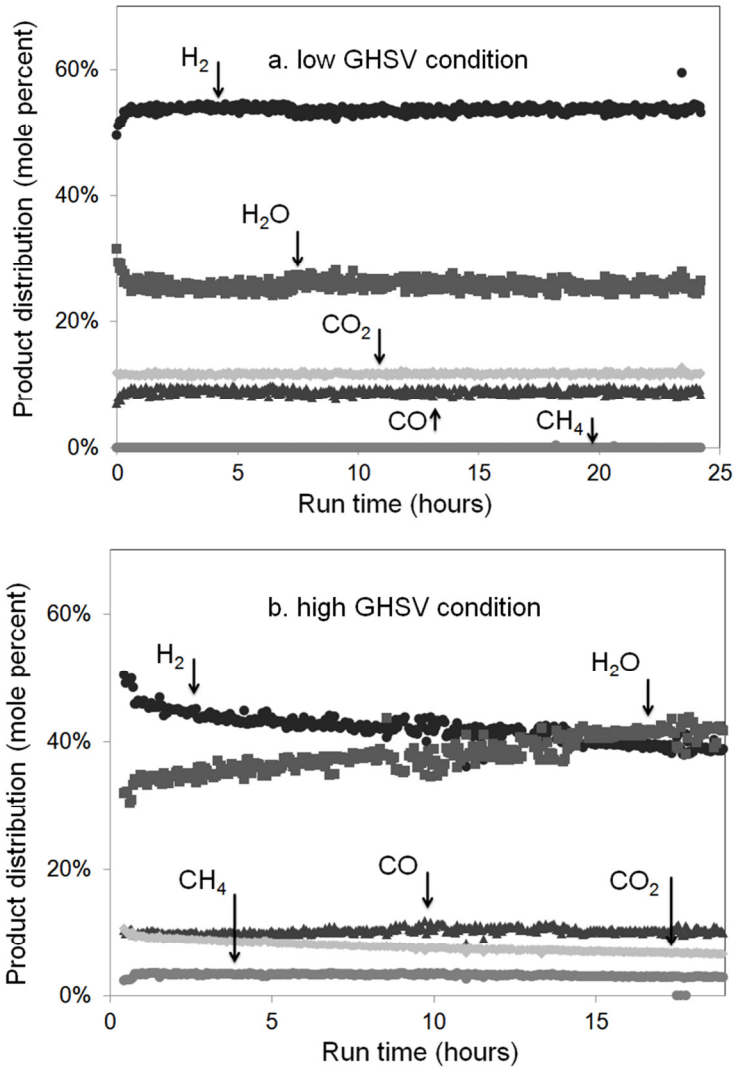

Figure 4.1: Reforming pure ethanol with a 1.8 S/C ratio and a) monolith GHSV = 22,000 h^{-1}. Washcoat loading = 2.0 g/in^3 and b) monolith GHSV = 44,000 h^{-1}. Washcoat loading = 0.5 g/in^3.

During the 19-hr high GHSV test, conversion decreased from 94% to 78% and hydrogen selectivity decreased by 10%. Thus activity changed more significantly then selectivity. The changes in selectivity that occurred were primarily due to changes in WGS activity (equation 5). Additional details are provided in Appendix C.1. In addition to the changes in selectivity towards C_1 gas species, the selectivity towards acetaldehyde and ethylene increased with TOS. Acetaldehyde increased more rapidly than ethylene, however, neither increased at rates significant enough to impact the distribution of H_2 and C_1 gas species. The cause for deactivation during ESR is likely coke formation. After the test shown in Figure 4.1b, an oxidation treatment of the catalyst at 650°C produced CO_2 indicating that coke was present on the surface.

4.2. Reforming sulfur-free E85: the impact of higher hydrocarbons

The high and low space velocity conditions used in the previous section during ESR were also used to steam reform a sulfur-free E85. By comparing the results of sulfur-free E85 with pure ethanol, the impact of the higher hydrocarbons in the gasoline on catalyst stability can be studied without compounded effects from sulfur. Two sulfur-free E85 fuels were used: an 85% ethanol/15% isooctane (gasoline surrogate) blend and an 85% ethanol/15% sulfur-free gasoline blend.

Initial results at the low space velocity condition determined that the catalyst was stable reforming both the ethanol/isooctane fuel for 24-hrs on stream and the ethanol/sulfur-free gasoline fuel for 110-hrs on stream. Similar to the ESR results at these conditions, no change in activity, selectivity, or monolith temperature profile was measured during the entirety of these tests. Unconverted ethanol was not detected in the effluent and C, H, and O atom balances indicated that both the ethanol and gasoline (or isooctane) were fully converted to the major product species shown. Thus, no impact of the higher hydrocarbons was observed at these conditions. The results of these tests are shown in Figure 4.2 and Figure 4.3.

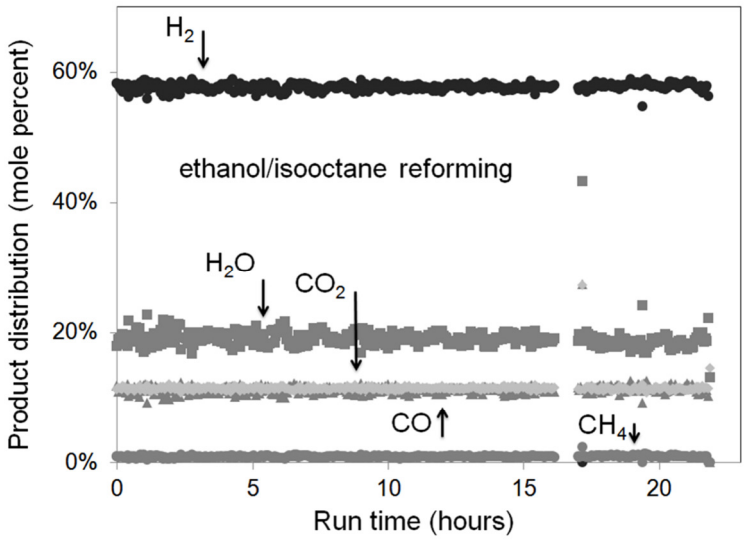

Figure 4.2: Reforming sulfur-free 85% ethanol/15%isooctane with 1.8 S/C and GHSV = 22,000 h^{-1}. Washcoat loading = 2.0 g/in^3

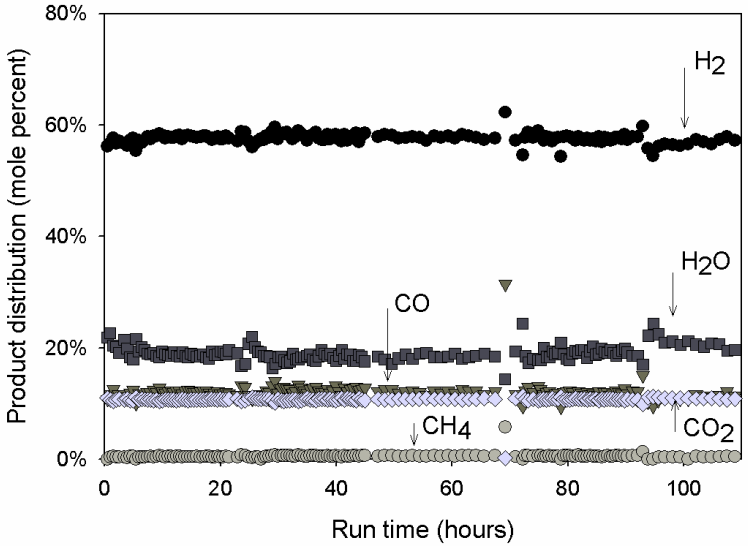

Figure 4.3: Reforming sulfur-free E85 with 1.8 S/C and GHSV = 22,000 h^{-1}. Washcoat loading = 2.0 g/in^3

At the high GHSV, catalyst deactivation was immediately measureable upon introduction of the sulfur-free E85 (washcoat loading 0.5 g/in^3 and GHSV: 44,000 h^{-1}). The results of this test are shown in Figure 4.4. After 4-hr on stream ethanol conversion had dropped from 100% to 97% and hydrogen yield had decreased by 14%. Selectivity to both hydrogen and carbon dioxide decreased whereas selectivity towards carbon monoxide and methane increased. These changes in selectivity were similar to those measured for pure ESR. Similar to the ESR results, the production of C_2 species (acetaldehyde and ethylene) increased with TOS, however, the production rates were higher during the sulfur-free E85 reforming than during the ethanol reforming.

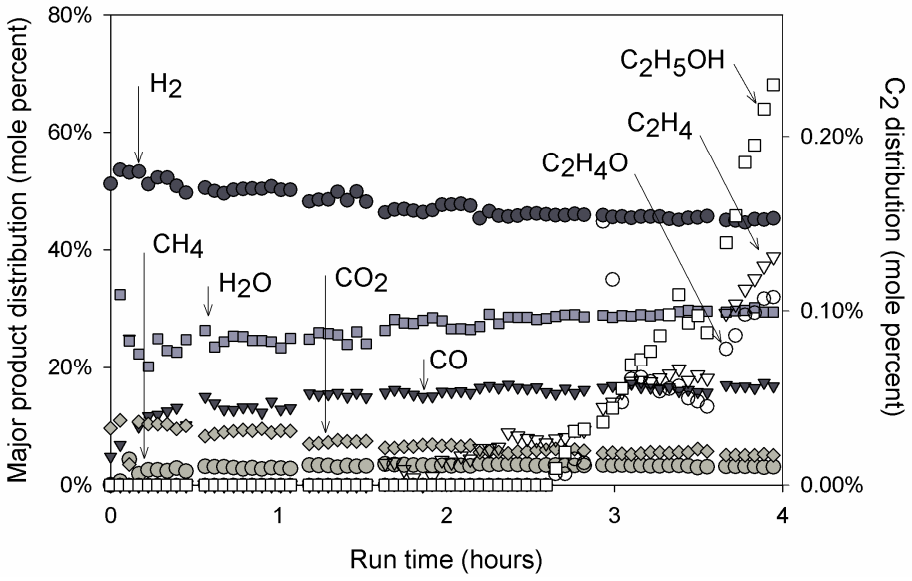

Figure 4.4: Reforming sulfur-free E85 with S/C = 1.8, washcoat loading = 0.5 g/in^3 and GHSV 44,000 h^{-1}

Although there were differences in selectivity between the SR of ethanol and sulfur-free E85, the trends were similar. In addition, the changes in activity were also similar. The deactivation rate for the pure ethanol and sulfur-free E85 reforming were calculated and the deactivation rate during E85 steam reforming was within 5% of the rate measured for ethanol steam reforming. The deactivation rate (r_d) was calculated by measuring the change in activity (*da*) during the time on stream (*dt*) according to equation 19.

$$r_d = \frac{da}{dt} = \frac{N_{tf} - N_{to}}{N_{in}} \cdot \frac{1}{\mathrm{dt}} \quad (19)$$

In equation 19 the change in activity was calculated using the change in molar flow rate of ethanol in the effluent during the time on stream ($N_{tf} - N_{to}$) as a fraction of the total molar flow rate of ethanol at the inlet. The results of

these calculations demonstrated that the higher hydrocarbons in the gasoline did not significantly impact catalyst activity.

4.3. Reforming sulfur-containing E85

The only previously published paper on steam reforming E85 used high reactor temperatures (800°C and above) and high S/C ratios (6:1 and above). At these conditions the authors did not measure catalyst deactivation. However, the impacts of both sulfur and coke formation are more likely to impact the catalyst at lower temperature and S/C ratios. In this section the reforming of E85 containing 5 ppm sulfur was studied at the same temperature, S/C ratio, and GHSV conditions used in the previous sections. Thus, the results can be compared to tests with sulfur-free fuels reported in previous sections to identify the impact of sulfur on catalyst stability.

At the low GHSV condition, for which no deactivation was measured reforming the pure ethanol, the isooctane/ethanol, or the sulfur-free E85, significant catalyst deactivation was measured with the sulfur-containing fuel. The product distribution for major gas species is shown in Fig 4.5.

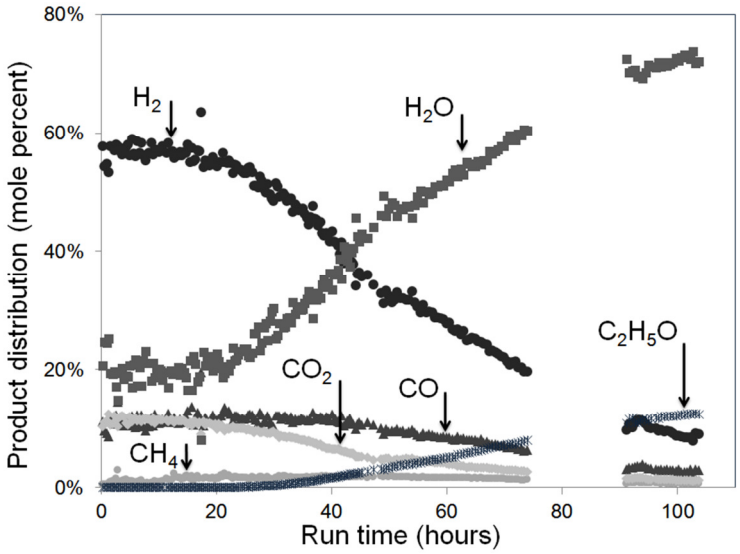

Figure 4.5: Reforming 5 ppm sulfur E85 with S/C = 1.8, washcoat loading = 2.0 g/in^3, GHSV = 22,000 h^{-1}

Initially, the catalyst reformed the sulfur containing fuel to equilibrium product distribution and full conversion, yielding the same result as the sulfur-free fuel. However, after 20-hrs on stream unreacted ethanol was detected and at 22-hrs this coincided with changes in the concentrations of major gas species and initial detection of ethylene, acetaldehyde and ethane. After 60-hrs on stream higher hydrocarbons species such as benzene, isooctane and butadiene were detected in trace amounts indicating that the catalyst was no longer reforming the higher hydrocarbons. Catalyst activity began to stabilize at conversions of approximately 21% after 105-hrs on stream. The initial and final conversion and the initial and final selectivity for each species are shown in Table 4.1.

Table 4.1: Initial and final selectivity for 105-hr test (Figure 10) reforming E85 containing 5-ppm sulfur with S/C = 1.8 and 22,000 h^{-1}

		Product distribution (mol/mol ethanol consumed)						
	Conversion	H_2	CO	CO_2	H_2O	CH_4	C_2H_4	C_2H_4O
Initial yield	100%	5.33	1.09	1.06	2.97	0.07	0	0
Final yield	21%	2.48	0.77	0.34	0.22	0.18	0.55	0.02
Equilibrium	100%	5.23	1.07	1.08	2.58	0.21	0	0

During the test in Figure 4.5, two different deactivation regimes were observed. In the first, acetaldehyde, CO, and CH_4 production (per mole ethanol converted) increased with TOS. After approximately 45-hrs on stream the production levels stabilized and began to decrease. In contrast, production of H_2 and CO_2 and conversion of H_2O continuously decreased and production of ethylene continuously increased during the entirety of the test. During the test, outlet temperatures increased from 628°C to 654°C; thus the reaction became less endothermic with TOS.

Given that carbon formation was detected after sulfur-free reforming tests (Section 4.2), and that one of the primary products at the end of the test in Figure 4.5 was a coke precursor (ethylene), it was assumed that coke had formed during the 105-hr test. In order to quantify the extent of coking, TPO was performed on the spent catalyst. TPO determined that carbon accounted for 58% of the catalytic washcoat weight. The CO_2 and mass loss measured during this test are shown in Figure 4.6. The primary exothermic energy

peak (not shown), mass loss peak and CO_2 occurred between 500 and 650°C. The presence of graphitic carbon was confirmed by XPS analysis. The product distribution at the end of the test (Table 4.1), including 21% ethanol conversion, was produced on a catalyst with significant carbon coverage (120:1 C:PM ratio). Thus, either some catalytic surface is still available or some of the carbon species are catalytically active. Since the primary pathway to ethanol conversion in this instance is the dehydration reaction to ethylene (over 55% of the ethanol is converted to ethylene) it is possible that this reaction is catalyzed on a different type of site (for instance on carrier sites) or that coke primarily forms on the carrier rather than the precious metal.

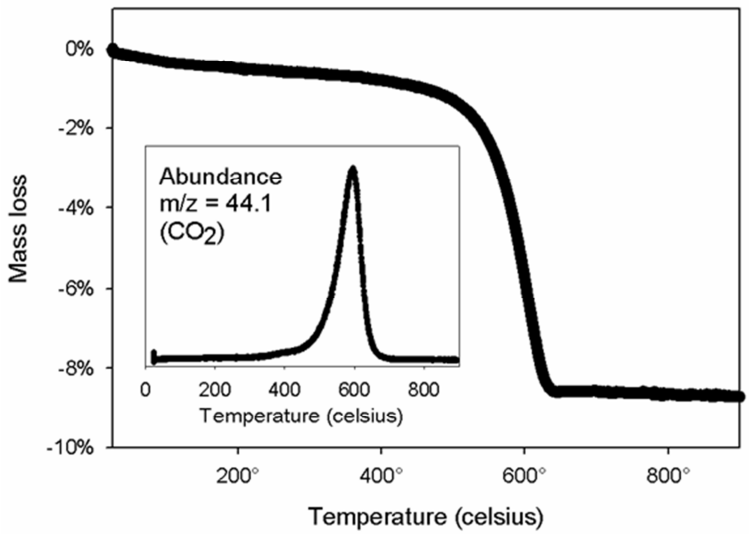

Figure 4.6: TPO results for catalyst exposed to 105-hrs reforming 5 ppm sulfur E85 (Figure 9). TPO heating rate = 5°C/min.

Although ppm concentrations of sulfur led to the substantial catalyst deactivation depicted in Figure 4.5, significant amounts of residual sulfur were not measured on the spent catalyst. XPS tests on the catalyst did not measure sulfur indicating that the amount was less than the XPS detection limits (0.1 at%). Yamazaki et al also reported significant sulfur-induced catalyst deactivation without detecting residual sulfur on used Pt/ZrO_2 catalysts [59]. ICP was performed to augment XPS results and the analysis measured surface concentrations of less than 0.03 at% (S:PM < 3:100). Despite these low values, the catalyst had sufficient sulfur exposure during the first 10-hrs on stream to have complete precious metal coverage. Thus, although the catalyst had considerable exposure to sulfur only a small fraction of this sulfur was measureable on the catalyst surface. The impact of sulfur on catalyst stability is discussed in more detail in Chapter 6.

4.4. Conclusions and Future work

The $Rh\text{-}Pt/SiO_2\text{-}ZrO_2$ catalyst was stable reforming ethanol and sulfur-free E85 at low GHSV conditions for over 100-hrs. At high GHSV conditions, catalyst deactivation was observed and deactivation rates were calculated. The performance of the catalyst during steam reforming of ethanol and during steam reforming of sulfur-free E85 at different GHSV was compared and it was concluded that the higher hydrocarbons did not significantly

impact catalyst stability. At the low GHSV condition the catalyst was stable steam reforming the sulfur-free E85 for 110-hrs with no indication of catalyst deactivation.

At conditions for which no deactivation was measured in the absence of sulfur for over 100-hrs, small amounts of sulfur in the fuel (5 ppm wt%) were found to significantly decrease activity and lower selectivity towards H_2. After 105-hrs on stream ethanol conversion was 21% and H_2 selectivity had decreased by 53%. The extent of sulfur-induced deactivation was surprising considering that the amount of residual sulfur on the catalyst was low (0.03 at%). However, TPO determined the spent catalyst was 58 wt% carbon. Thus, sulfur may increase the susceptibility of the catalyst to coking. This hypothesis is explored in further detail in Chapter 6.

In this chapter we have shown that small amounts of sulfur deactivate the catalyst to levels that are unacceptable for industrial hydrogen production from E85. Thus, in order to operate a stable process at the energy efficient conditions identified in Chapter 1, catalyst regenerations must be utilized. The potential for incorporating regenerations into the E85 steam reforming process is investigated in the next chapter.

Chapter 5 : The regenerability of a deactivated catalyst

In Chapter 4, it was shown that the Rh-Pt/SiO_2-ZrO_2 catalyst deactivates during E85 steam reforming at energy efficient conditions. Thus, in order to operate a stable process with this catalyst, the conditions could be changed to less energy efficient conditions (higher temperatures and higher S/C ratios) where deactivation is less likely to occur. Alternatively, the process could be run at the energy efficient conditions identified in Section 1.3 but methods to regenerate the catalyst could be incorporated into the process. Catalyst regeneration techniques are often used in industrial processes to allow for less energy intensive (and thus more cost effective) operation. In a typical 500 MW coal fired power plant, regeneration of environmental control catalysts saves between $500K and $1 million in annual operating costs [113]. In this chapter the potential of incorporating regeneration methods to operate an efficient E85 reforming process with the Rh-Pt/SiO_2-ZrO_2 catalyst is investigated. Different methods of regeneration are evaluated and the success of regenerations after various degrees of deactivation is also investigated.

5.1. Potential catalyst regeneration techniques

During reforming of sulfur-containing E85 some degree of the Rh-Pt/SiO_2-ZrO_2 deactivation is attributed to coke formation. The most common method to regenerate a coked catalyst is by oxidation with air [8]. However, gasification with steam is also a potential method to remove coke [114]. Thus, regeneration was attempted at 650°C with three different gaseous environments: 100% N_2, 80% N_2/20% steam and 50% N_2/50% air.

In order to determine the most effective regeneration method, a deactivated catalyst was exposed to different regeneration conditions and the subsequent performance was measured. Regenerations were performed on a catalyst that was deactivated during steam reforming of E85 with 28 ppm sulfur (GHSV = 22,000h^{-1}, monolith washcoat loading = 2.0 g/in^3). At these steam reforming conditions, catalyst deactivation was measureable after 14-hrs on stream. Regenerative treatments were performed after the catalyst had been on stream for 33-hrs during which time conversion decreased from 100% to 84%. Initial activity, activity after deactivation, and activity after treatment with steam and air are compared in Figure 5.1 (treatment with nitrogen not shown for clarity).

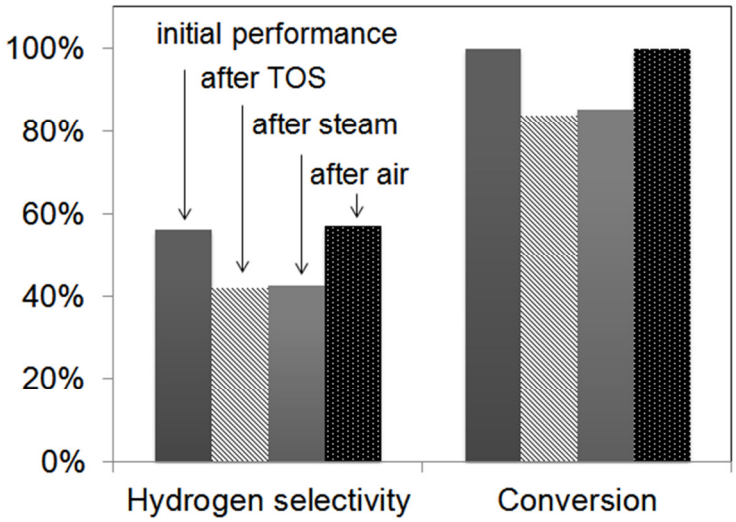

Figure 5.1: Catalytic performance after deactivation followed by treatment by either steam (20% H_2O/N_2) or air (50% air/N_2) at GHSV = 22,000 h^{-1}

Neither exposure to the inert atmosphere nor exposure to the steam improved either activity or selectivity. Treatment with air, however, was found to be an effective method to regenerate the catalyst. After air treatment, initial activity and selectivity were measured. The ineffectiveness of the steam treatment may be due to the nature of the carbon or the experimental conditions (i.e. temperature and residence time). In this work, all subsequent regeneration studies use air treatment.

5.2. Catalyst performance after air treatment

Although air treatments restored catalytic performance, deactivation occurred more rapidly after the regeneration than it did on the fresh catalyst. As shown in Figure 5.2, although the first regeneration was performed after

33-hrs on stream, in order to maintain conversion above 84%, the second air treatment had to be performed after only 19-hrs on stream. Thus the deactivation occurred more rapidly after the air treatment and the time between regenerations was shortened. After both the second and third air treatments, changes in activity were measured immediately after the reactants were introduced. Further, earlier detection of C_2 intermediates occurred after each successive regeneration (Figure 5.2b). Thus, air treatments were effective at reproducing initial (measured) performance but did not return the catalyst to its initial chemical and/or structural state.

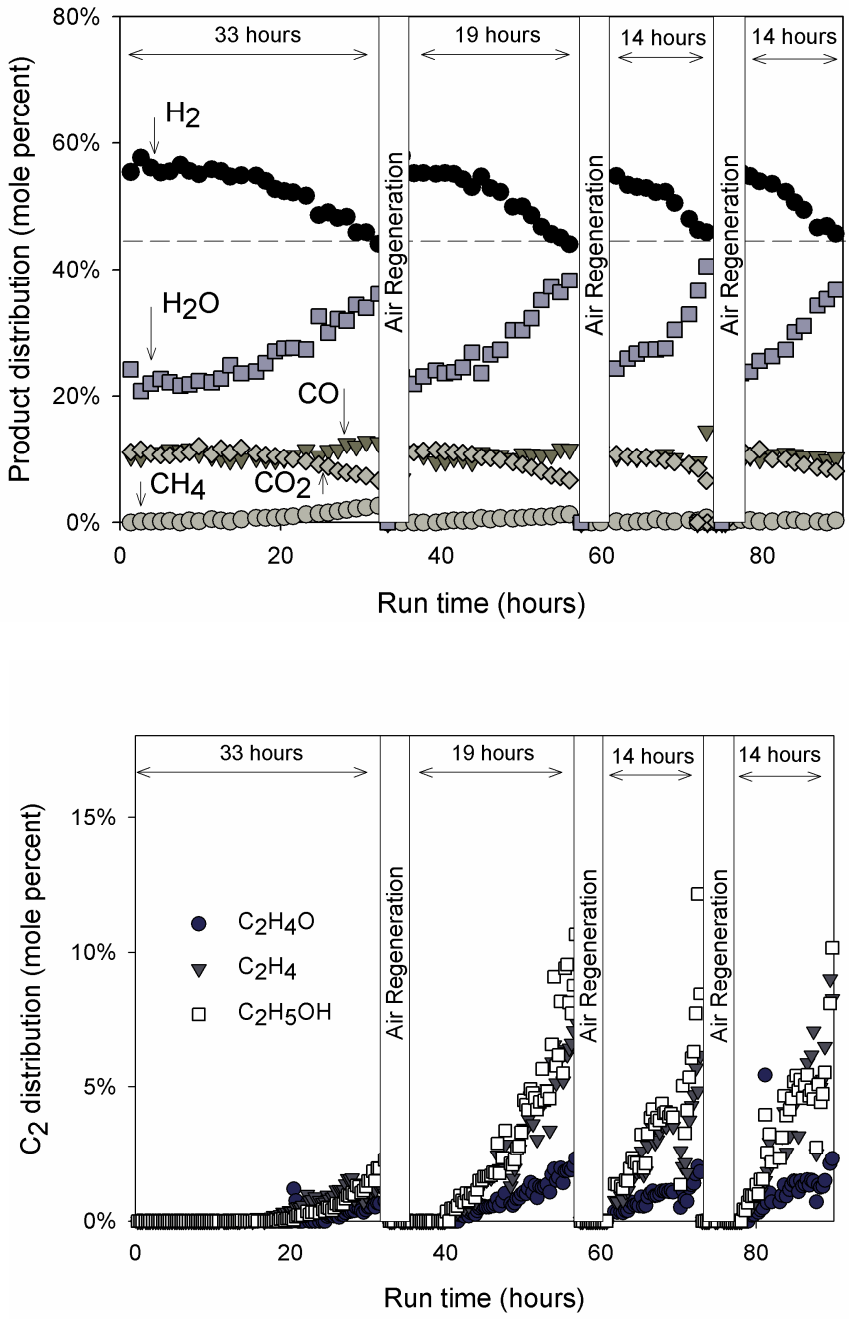

Figure 5.2: Reforming 28 ppm sulfur E85 with steam/carbon = 1.8, washcoat loading = 0.12 g/cm^3 (2.0 g/in^3) and GHSV = 22,000 h^{-1} with air regenerations = 50% air, 50% N_2.

The results of the test in Figure 5.2 demonstrate that air treatments can partially regenerate a deactivated catalyst. Although initial activity was always restored, deactivation was not fully reversed; subsequent deactivation occurred more rapidly. The catalyst in Figure 5.2 initially operated at equilibrium conditions for 14-hrs on stream, thus the catalyst was operating with an excess of active sites. Therefore, it is possible that the regenerations restored a fraction of actives sites, but that the restored number was enough to achieve the initial activity. In the next section, regeneration is performed on a catalyst with a lower washcoat loading (less total catalyst) than the test in Figure 5.2. The goal is to study whether air regeneration can restore initial activity after more severe levels of deactivation.

5.3. The influence of extent of deactivation on catalyst regenerability

In order to test the regenerability of the catalyst after more extensive levels of deactivation, tests similar to those shown in Figure 5.2 were performed with a reduced amount of catalyst (washcoat loading = 0.5 g/in^3 and GHSV = 22,000 h^{-1}). The regenerability of the catalyst was measured after conversion had decreased from 100% to 25%. The results of this test are shown in Figure 5.3. Although the catalyst used for this test had lower washcoat loading and was deactivated to a greater extent than in the previous test, the result of the two tests were similar: initial activity was

restored after air treatment but subsequent deactivation was more rapid. Additional studies performed at similar conditions but with higher GHSV's than those in Figures 5.2 and 5.3 also revealed higher deactivation rates after regenerations. Results obtained during steam reforming of the sulfur-containing E85 at higher GHSV is shown in Appendix C.2 and results during the steam reforming of a sulfur-free fuel is shown and discussed in Section 6.6.

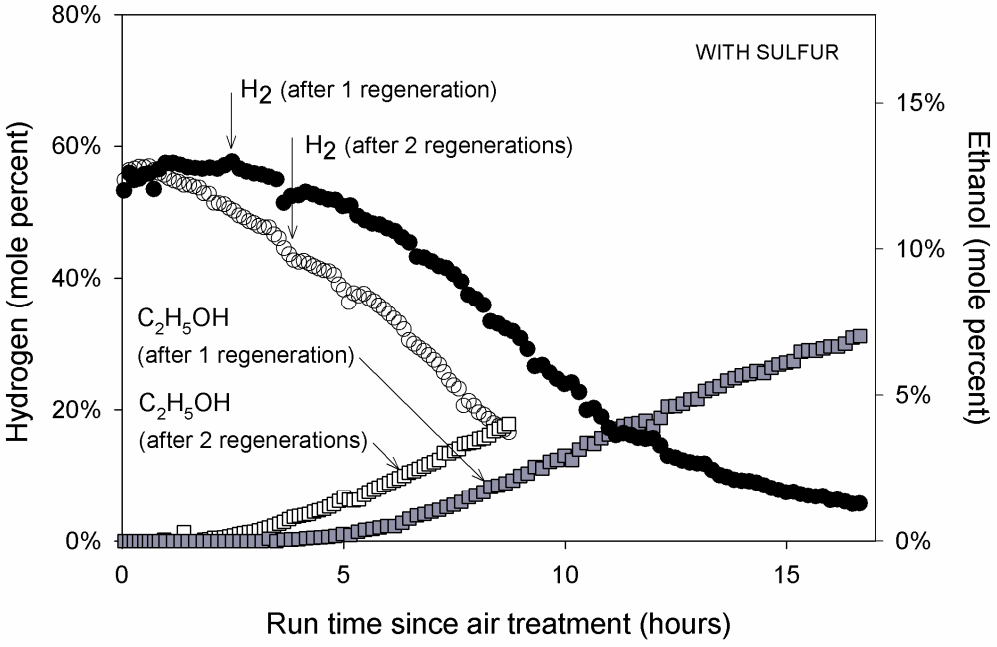

Figure 5.3: Reforming 5 ppm sulfur E85 with steam/carbon = 1.8, washcoat loading = 0.5 g/in^3 and GHSV = 22,000 h^{-1}, with air regeneration = 50% air, 50% N_2

The results of the different regeneration tests discussed thus far indicate that the catalyst is not returned to its initial state after prolonged TOS followed by air treatment. It is possible that all sites were not

regenerated by air treatment, for example, due to sulfur or refractory carbon that remain on the surface after regeneration. An additional hypothesis is that air treatments regenerate all sites but detrimentally impact the catalyst. Finally, it is possible that an additional deactivation mechanism occurs during the steam reforming condition such as metal or support sintering which the air treatment does not reverse. These hypotheses are explored in more detail in the next chapters.

5.4. Preemptive air regenerations

In the previous sections catalyst regeneration was attempted after varying extents of deactivation. In addition to these tests, a test was performed with 'preemptive' regenerations, meaning, regenerative air treatments were performed prior to any measure of catalyst deactivation. These tests were conducted at the same GHSV and washcoat loading conditions as the test shown in Figure 5.2. Hour long regenerations were performed after every 4-hrs of reforming. Seven reforming/regeneration cycles were performed for a total reforming time of 28-hrs and a total run time of 35-hrs (7 cycles). The product distribution for this test is shown in Figure 5.4.

During the test with preemptive regenerations, the catalyst maintained initial activity with no sign of deactivation for the entirety of the

test, whereas the catalyst was able to sustain initial performance for less than 14-hrs without preemptive air treatments (Figure 5.2). Further, during the test in Figure 5.2, although deactivation of major species was measured at 14-hrs, trace levels of ethanol and C_2 intermediates became measureable after 10-hrs on stream. However, during the test with preemptive regenerations C_2 intermediates were never detected. We can conclude that preemptive regenerations prolong stable performance.

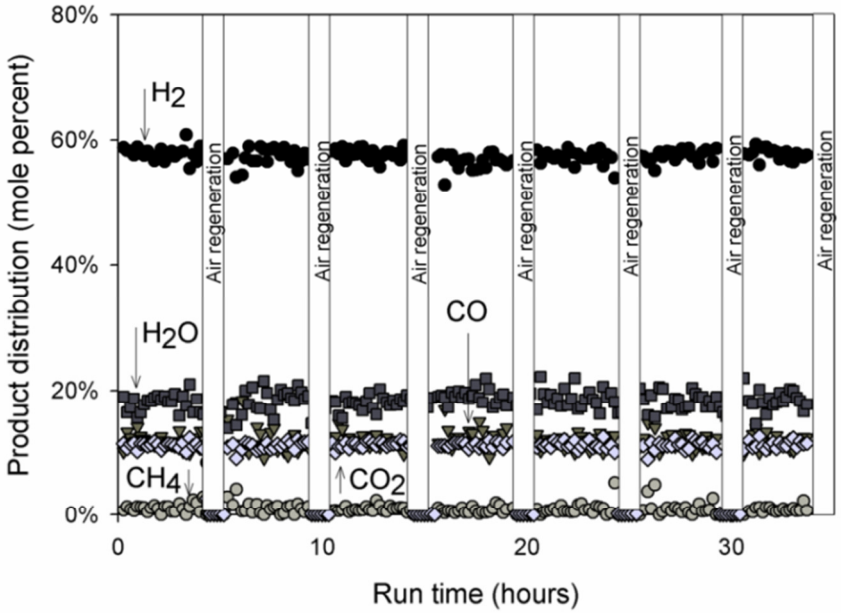

Figure 5.4: Reforming 28 ppm sulfur E85 with steam/carbon = 1.8, washcoat loading = 0.12 g/cm^3 (2.0 g/in^3) and GHSV = 22,000 h^{-1}, with preemptive air regeneration = 50% air, 50% N_2.

Catalyst coking is at least one of the causes of catalyst deactivation, thus, preemptive regenerations may prolong stable performance by removing surface carbon before enough accumulates to yield measureable deactivation. However, in the previous regeneration studies some extent of irreversible

deactivation was measured. The preemptive regenerations may have the same impact on the catalyst as the regenerations performed after longer periods of time on stream (partially regenerating the catalyst) and the irreversible element of deactivation is not yet realized in the TOS presented in Figure 5.3. It is also possible that utilizing preemptive regeneration 'cycling' may prevent the irreversibility measured previously.

5.5. Conclusions and future work

In Chapter 4 it was shown that the Rh-Pt/SiO_2-ZrO_2 catalyst was significantly deactivated during steam reforming of sulfur-containing E85. In this chapter it was demonstrated that air treatments were an effective method to regenerate the catalyst, even after the degree of deactivation observed in Chapter 4. After extensive deactivation (over 75% activity loss) initial activity was restored by exposing the catalyst to air treatment at 650°C.

Although air treatments were found to be the most effective method to regenerate the catalyst, the deactivation rates measured after air treatments were higher than the initial deactivation rates. This result demonstrated that air treatment may only partially reverse deactivation; thus there may be both an irreversible and reversible aspect to the deactivation. Alternatively, air

regenerations may detrimentally impact the catalyst making it more susceptible to subsequent deactivation.

The cause of the higher deactivation rates during subsequent reforming cycles is explored in the next chapters. The first hypothesis investigated in Chapter 6 is that chemisorbed sulfur is not removed by air treatments and therefore higher sulfur concentrations increase the deactivation rate during subsequent reforming cycles. The second hypothesis, investigated in Chapter 7, is that refractory coke species are not removed by air treatment and reduce the number of effective sites during subsequent reforming cycles. The third hypothesis, investigated in Chapter 8, is that changes to the catalyst carrier, such as carrier sintering cause the higher deactivation rates. Finally, in Chapter 9, changes to the precious metal particles, such as precious metal sintering, are investigated as a possible cause for the irreversible deactivation observed in Figure 5.2.

In this chapter, in addition to performing regenerations after measured deactivation, regenerations were performed before deactivation was measured. These 'preemptive' regenerations prolonged stable activity. It is unknown whether this procedure delays the onset of measured deactivation or whether it prevents it. If preemptive regenerations indefinitely maintain stability, there may be a time-dependent aspect to the deactivation. For instance, a deactivation mechanism may be regenerable

after short periods of time on stream but may become irreversible after more extensive deactivation. Therefore, understanding the different deactivation mechanisms that occur during the steam reforming conditions, as well as the reversibility of each of these mechanisms may also determine why preemptive regenerations are effective.

Chapter 6 : The impact of sulfur on catalyst stability

In this chapter the effect of sulfur on the catalyst activity and selectivity is investigated. In Chapter 4 it was shown that the catalyst deactivated due to low concentrations of sulfur in the reactants. During a 105-hr test steam reforming E85 with 5 ppm sulfur, catalyst performance decreased to less than 21% of the initial activity. Despite the significant drop in performance due to sulfur, approximately 0.03 at.% sulfur was detectable on the catalyst. Thus, the concentration of sulfur was not enough to cause the amount of catalyst deactivation observed. It was postulated that sulfur caused coke formation, which was also identified on the catalyst by TPO. In this section, the influence of sulfur on coke formation is quantified. In addition, sulfur's effect on catalyst selectivity is investigated to determine whether the mechanism that causes coke formation can be identified.

In Chapter 5, it was found that catalyst deactivation was faster after regeneration treatments. It was hypothesized that this could be caused by residual sulfur remaining on the surface that was not removed by the air regenerations. To investigate this hypothesis, the reversibility of sulfur poisoning on the Rh-Pt/SiO_2-ZrO_2 catalyst is studied.

6.1. The effect of sulfur on catalyst activity and selectivity

Several authors have reported that sulfur may impact both selectivity and activity during catalytic fuel reforming. In this section, we compare catalyst activity and selectivity during the reforming of the sulfur-free and sulfur-containing fuel. One set of tests was conducted at the high GHSV condition used in Sections 4.1 and 4.2. The second set of tests was conducted with a particle bed in order to facilitate easier characterization of the spent catalysts. Therefore, the impact of sulfur was studied at different conditions and for different degrees of deactivation. The product distributions for the major gas species during each of these tests are shown in Figure 6.1 (packed bed) and Figure 6.2 (washcoated monolith). A table including the initial and final ethanol conversion and the initial and final selectivity towards major product species is located in Table 6.1.

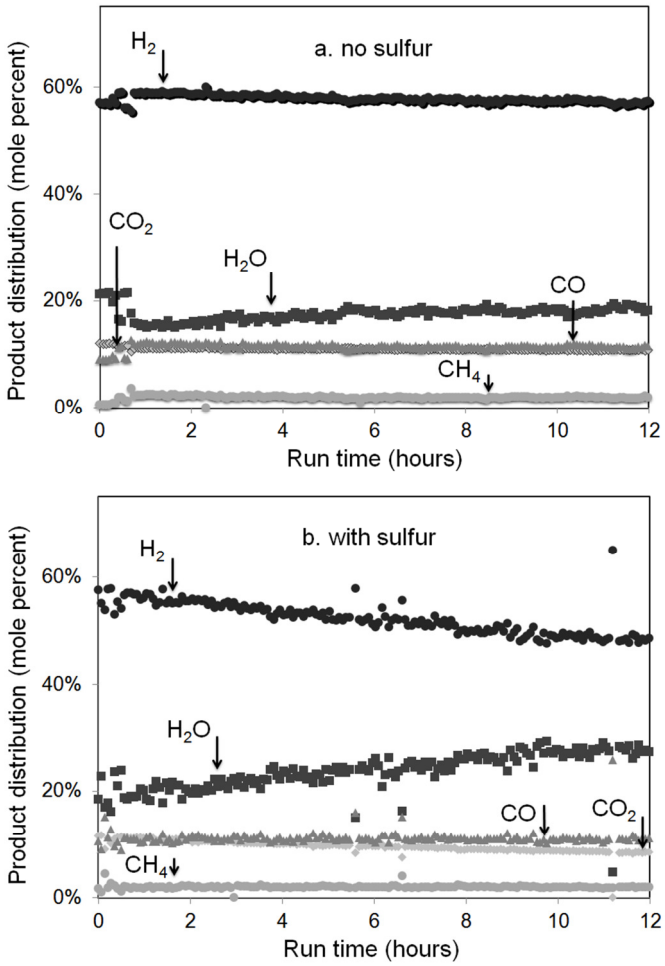

Figure 6.1: Reforming a) sulfur free E85 and b) 5 ppm sulfur E85 with conditions: S/C = 1.8, 250 mg catalyst, 3:1 wt ratio quartz:catalyst, GHSV = 22,000 h^{-1}

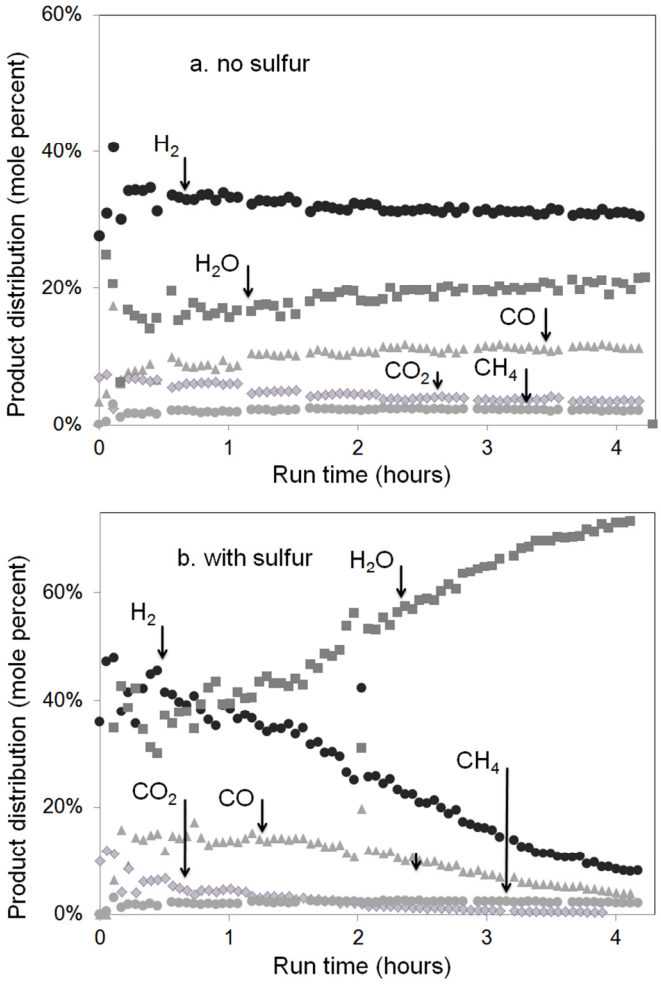

Figure 6.2: Reforming a) sulfur free E85 and b) 5 ppm sulfur E85 with conditions: S/C = 1.8, washcoat loading = 0.5 g/in^3, GHSV = 22,000 h^{-1}

For both the packed bed and monolith tests, the presence of sulfur significantly decreased catalyst activity (Table 6.1). During the monolith tests, ethanol conversion decreased from 100% to 35% in 4-hrs reforming the sulfur-containing fuel whereas it decreased from 100% to 98% in 4-hrs reforming the sulfur-free fuel. During the packed bed tests, ethanol conversion decreased from 98% to 84% in 12-hrs while reforming the sulfur-

containing fuel and decreased from 100% to 99% reforming the sulfur-free fuel.

Table 6.1: Initial and final conversion and selectivity towards major product species for packed bed (Figure 6.1) and monolith tests (Figure 6.2)

Particle bed tests	Selectivity towards major products			
	Sulfur		No sulfur	
Product	Initial	Final	Initial	Final
H_2	5.51	5.06	6.04	5.67
CO	1.12	1.16	1.23	1.12
CO_2	1.07	0.88	1.15	1.08
H_2O (consumption)	2.86	2.63	3.13	2.94
CH_4	0.19	0.21	0.24	0.19
Conversion	98.0%	84.0%	100.0%	99.0%

Monolith tests	Selectivity towards major products			
	Sulfur		No sulfur	
Product	Initial	Final	Initial	Final
H_2	3.87	1.98	4.49	3.89
CO	1.28	0.97	1.12	1.44
CO_2	0.54	0.08	0.84	0.45
H_2O (consumption)	1.32	-1.98	2.03	1.63
CH_4	0.30	0.26	0.24	0.26
Conversion	1.0%	35.0%	100.0%	98.0%

The same selectivity trends were seen during the sulfur and sulfur-free tests, for instance, comparing Figure 6.1b and 6.2b. During either the reforming of the sulfur-free or the sulfur-containing fuel, production of H_2 and CO_2 and conversion of H_2O decreased with TOS. Also, in both cases the CO and CH_4 initially increase with TOS. As discussed in Section 4.1 during the steam reforming of pure ethanol, the overall steam reforming reaction (equation 2) was most significantly affected by deactivation, however, some

loss in WGS activity with TOS was also observed. The results in Figure 6.1, Figure 6.2 and Table 6.1 indicate that sulfur exacerbated the trends in selectivity (towards H_2 and C1 gas species) that were observed during reforming with sulfur-free fuels.

In Figure 6.2b, the selectivity towards CO and CH_4 changes after a certain TOS. Thus, for the significantly deactivated catalyst, two different deactivation regimes exist. This result was consistent with the changes in selectivity measured during the 105-hr low GHSV test for the sulfur-containing fuel (Figure 4.5). Since this extent of deactivation was not reached during any of the sulfur-free tests, it is unknown whether this result is attributable to sulfur.

In addition to having a significant impact on conversion, sulfur had a clear impact on acetaldehyde and ethylene production. The selectivity towards these intermediate species with and without sulfur is compared for the particle bed tests in Figure 6.3 and for the washcoated monolith tests in Figure 6.4. As discussed in section 1.5, ethylene is a known precursor, and it is also possible that acetaldehyde can lead to coke formation. Thus, sulfur may increase coke formation by promoting the production of one or both of these species. Alternatively, sulfur may impact the mechanism associated with converting these species to final products, thus increasing their measured concentrations. For instance, sulfur may prevent the gasification of

the carbon species (reverse reaction of equation 16) reducing the number of active sites to convert C_2 intermediates.

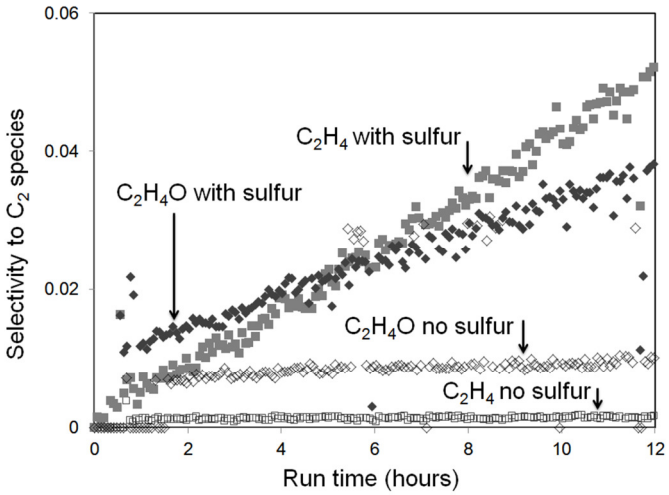

Figure 6.3: Selectivity towards C_2 species during packed bed tests with and without sulfur

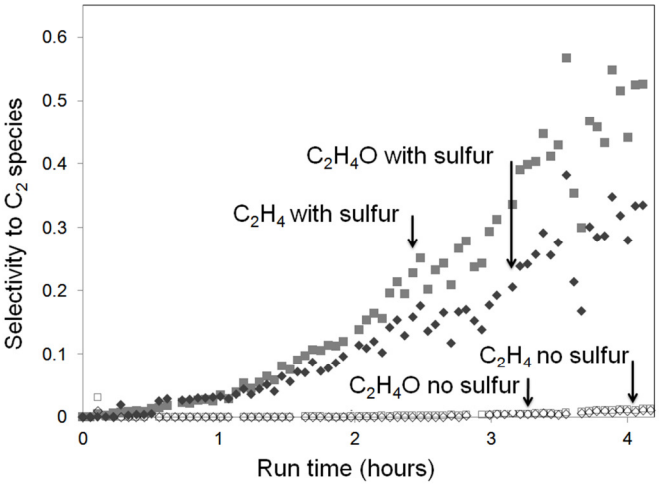

Figure 6.4: Selectivity towards C_2 species during monolith tests with and without sulfur

The results in Figures 6.3 and 6.4 demonstrate that sulfur increases the production of ethylene and acetaldehyde. Either of these species may be

coke precursors, however, ethylene is reported to be the most active hydrocarbon for coke formation [54]. During ESR, ethylene production occurs on acid sites whereas acetaldehyde is promoted on basic sites [52]. Thus, the increase of both of these species may indicate that they are promoted via different mechanisms. For example, sulfur may directly promote one of these intermediates, which indirectly increases the concentrations of the other. If sulfur promotes ethylene production, for instance, which in turn causes coking, than the increases in acetaldehyde concentrations could be the result of surface carbon rather than sulfur. Similarly, if sulfur primarily deactivates the catalyst by promoting coking, and coking is also the deactivation mechanism in the absence of sulfur, then the deactivation with sulfur would be similar, but more exacerbated than the deactivation without sulfur. This is the result demonstrated in the previous sections. Based on the influence of sulfur on ethylene and acetaldehyde, we propose that sulfur primarily deactivates the catalyst by promoting additional coke formation. The impact of sulfur on coking is studied in more detail in the next sections.

6.2. The impact of sulfur on coking

In order to assess how sulfur impacts coke formation, TPO was performed on the particle catalysts that had reformed the sulfur containing and sulfur-free fuels (Figure 6.1). During the TPO tests CO_2 and H_2O were

the only detected products in the effluent. The total carbon on the surface was calculated by integrating the CO_2 in the effluent and normalizing to the sample weight. The TPO profiles for the catalyst that had reformed the sulfur-free fuel and the sulfur-containing fuel are shown in Figure 6.5. The results demonstrate that sulfur increased coking rates. However, the sulfur-free sample also had considerable amounts of coke on the surface. Thus, sulfur was not the sole mechanism for coke formation.

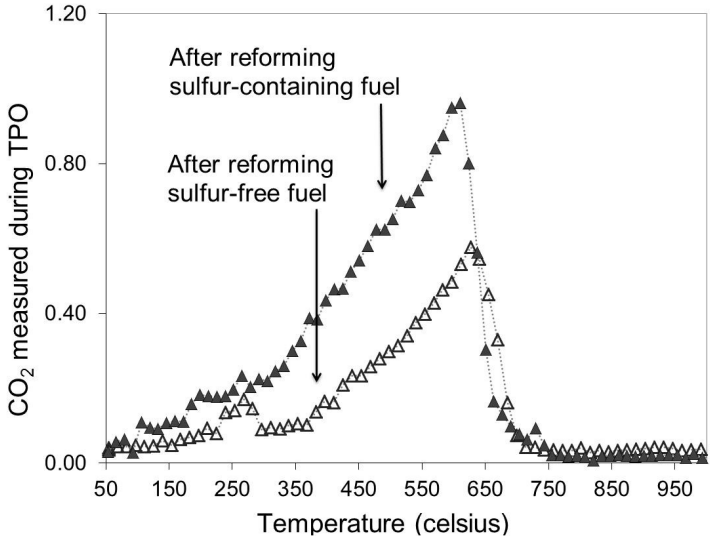

Figure 6.5: TPO results after 12-hrs reforming E85 with 0-ppm sulfur or 5-ppm sulfur (reactor tests shown in Figures 6.1). TPO (5%O_2/He) heating rate = 7°C/min.

TPO can also provide information on the degree of dehydrogenation of the coke. During TPO, the coke (C_xH_y) is oxidized to CO_2 and H_2O. Based on the concentrations of CO_2 and H_2O in the effluent, the C/H ratio of the coke species is calculated. The C/H ratio is an indicator of the degree of dehydrogenation of the coke species. As shown in Table 6.2, sulfur increased

both the amount and the C/H ratio of the coke. However, the coke burn-off temperature, an indication of the type of coke on the surface, was similar for the two catalysts (Figure 6.5). Further, after 12-hrs of steam reforming the sulfur-free fuel the catalyst had a similar C/H ratio to a catalyst that had reformed a sulfur-containing fuel for a shorter period of time (9-hrs). Thus, in this case the graphitic nature of the coke was not caused by sulfur, as suggested by other authors [64, 115].

Table 6.2: Sample weight% C, H_2 and overall C/H ratio on catalyst after 12-hrs reforming E85 with 0-ppm sulfur or 5-ppm sulfur (reactor tests shown in Figure 6.1)

	wt% C	wt% H_2	C/H
After reforming sulfur-free fuel 12-hrs	4.9%	6.6%	2.2
After reforming sulfur-containing fuel 12-hrs	13.1%	3.6%	4.9

6.3. The reversibility of sulfur poisoning (adsorption studies)

A series of tests was performed using TGA to understand the reversibility of sulfur adsorption on the Rh-Pt/SiO_2-ZrO_2 catalyst. At temperatures of 450, 650 and 850°C a pre-reduced catalyst was exposed to 5-ppm H_2S/N_2 and the resultant sulfur adsorption was measured as a mass gain. Although the fuels used in the reactor studies contain a complex mix of sulfur species, it is assumed that these species are readily converted to H_2S in the reformer [116-118]. Therefore, H_2S was used as the sulfur species

during TGA tests. The total sulfur adsorbed on the catalyst at 450, 650 and 850°C is shown in Table 6.3.

Table 6.3: Total adsorption (mg) of H_2S on pre-reduced Rh-Pt/SiO_2-ZrO_2 catalyst

Material	Temperature (celsius)	Adsorption (mg)	Corresponding S:PM ratio
Rh-Pt/SiO_2-ZrO_2	450	0.27	0.82
Rh-Pt/SiO_2-ZrO_2	650	0.24	0.72
Rh-Pt/SiO_2-ZrO_2	850	0.05	0.15
Carrier	6.5	0.00	0.00

As expected, the extent of adsorption is lowest at 850°C, a common threshold temperature above which sulfur-induced deactivation is minimized.

The results in Table 6.3 indicate that temperature has a significant impact on sulfur adsorption. This result is in agreement with the thermodynamics of sulfur adsorption on precious metals [61] and with experimental studies on sulfur poisoning during reforming processes [119]. In addition to temperature, the thermodynamics predict that the ratio of H_2S/H_2 is an important factor in determining the extent of adsorption [61]. Thermodynamics predicts lower amounts of sulfur adsorption at lower H_2S/H_2 ratios. Therefore, in the reactor, in the presence of high concentrations of hydrogen the sulfur adsorption will be much less than the concentrations in Table 6.3.

The isothermal desorption of sulfur was measured in a 100% N_2 environment and in a 40% H_2/N_2 environment. The results of this test are

shown in Figure 6.6. No mass loss was measured after the introduction of pure N_2, however, full desorption was measured after introduction of 40% H_2. Given the sensitivity limits of the TGA, it can be assumed that less than 0.013 at% sulfur remained on the surface after the introduction of hydrogen. Thus, the TGA results suggest that sulfur adsorption on this catalyst may be reversed in a H_2 environment when H_2S is removed.

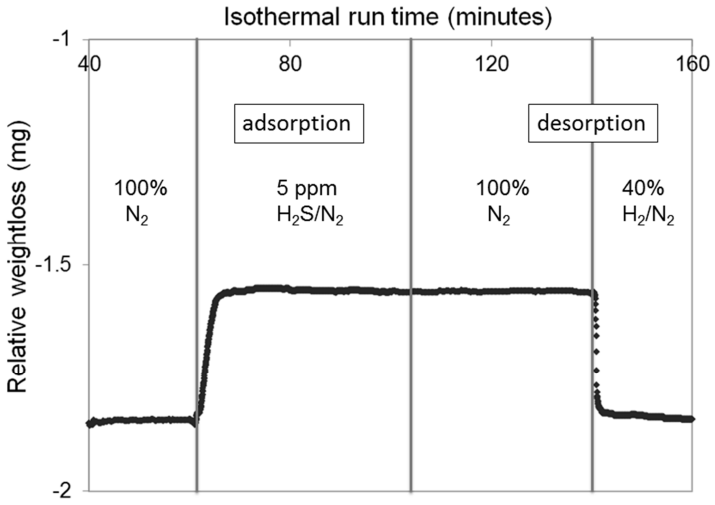

Figure 6.6: Isothermal (650°C) adsorption and desorption of H_2S on pre-reduced Rh-Pt/SiO_2-ZrO_2. Adsorption performed with 5 ppm H_2S/N_2. Desorption performed with 100% N_2 followed by 40% H_2/N_2.

6.4. Reversibility of sulfur poisoning (reactor tests)

In addition to the TGA studies, a series of reactor tests were performed to study the reversibility of sulfur poisoning during the steam reforming conditions. During these tests the catalyst reformed a sulfur-free E85 and was periodically exposed to injection of 1-ppm H_2S (1-ppm H_2S was total gas

concentration, thus more significant than the 5-ppm wt% in the fuel). The results of one of these tests are shown in Figures 6.7 and 6.8. As expected based on previous results, the injection of H_2S had a significant impact on catalyst stability. Immediately after injection, the catalyst activity began to decrease, selectivity towards hydrogen decreased and acetaldehyde and ethylene were detected in the effluent.

As shown in Figure 6.7, removal of H_2S from the feed immediately reduced the production of ethylene. However, the production of acetaldehyde sharply increased after the removal of H_2S and continued to do so for 0.5 additional hours. The dramatic response of ethylene, both to injection and removal of H_2S indicates the sulfur may impact ethylene production most directly. Ethylene is known to form on acidic sites and the adsorption of H_2S is known to increase surface acidity [120]. Thus, sulfur may promote carbon by increasing the acidity of the catalyst thus promoting the dehydration of ethanol to ethylene. The higher concentrations of acetaldehyde may be a direct result of a decrease in catalytic sites due to the coke, therefore, an indirect result of the sulfur.

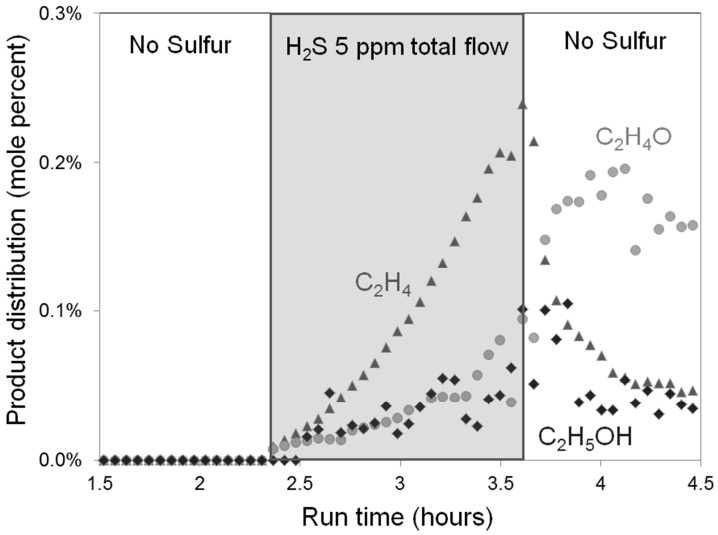

Figure 6.7: Reforming sulfur free E85 with conditions: S/C = 1.8, washcoat loading = 0.5 g/in^3, GHSV = 22,000 h^{-1}with 1.5-hr injection of 200 mL/min H_2S

In addition to the changes in selectivity towards C_2 species, sulfur also changed the selectivity towards major gas species. The product distribution for the major gas species are shown in Figure 6.8. The CO and CH_4 concentrations increased and H_2, CO_2 and water conversion decreased. These were the same trends that were observed during the reforming of both sulfur-free and sulfur-containing fuels in Section 6.1. Therefore, these changes may be the result of coke formation rather than sulfur poisoning. Further, ethylene was the only product that was significantly impacted by the removal of sulfur from the reactants. The major gas species were stable following sulfur removal.

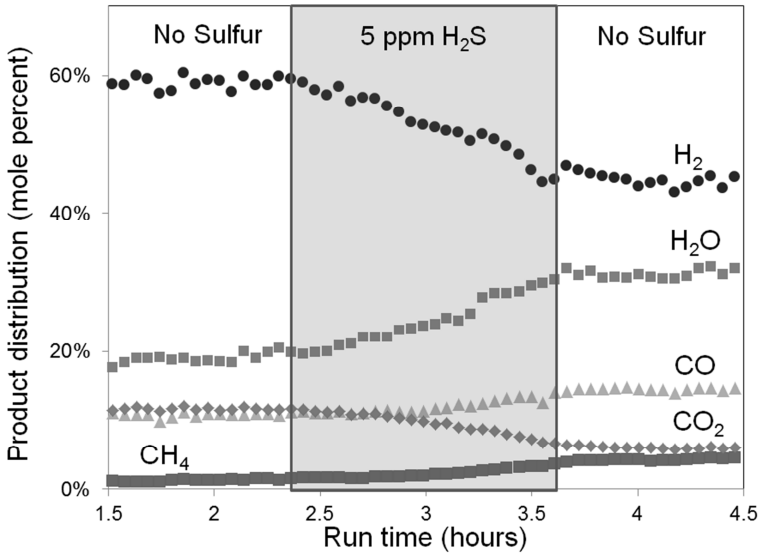

Figure 6.8: Reforming sulfur free E85 with conditions: S/C = 1.8, washcoat loading = 0.5 g/in^3, GHSV = 22,000 h^{-1}with 1.5-hr injection of 200 mL/min H_2S

The results of the tests in Figures 6.7 and 6.8 indicate that only a small degree of sulfur-induced deactivation is reversible by removing sulfur from the feed. Because sulfur increases coke formation, the deactivation which remains after sulfur is removed cannot be solely correlated with residual adsorbed sulfur. For instance, sulfur may desorb from the catalyst once it is removed from the feed, however, the coke formation that it promoted may remain on the surface.

6.5 Residual sulfur poisoning after regenerations

In the previous sections it was shown that some extent of sulfur poisoning is reversible. However, these tests did not conclusively show that sulfur was removed from the surface after regenerations. Thus, it is possible

that residual sulfur remained on the surface after regenerations and caused the higher deactivation rates measured in subsequent reforming cycles. To determine whether sulfur caused the irreversible deactivation observed in Chapter 5, calculations were performed to determine the amount of surface sulfur that would lead to such changes in behavior. These amounts were correlated with residual sulfur measurements by ICP on aged catalysts.

In Figure 5.2, catalyst deactivation was measureable after a period of stable activity and the period of stable activity was shorter during successive reforming cycles. During the first reforming cycle the period of stable activity was 14-hrs whereas during the second reforming cycle it was 7-hrs. A conservative calculation was performed to determine the amount of sulfur poisoning that would be required to decrease the period of stable activity to this extent. The deactivation rate measured from 14-hrs to 33-hrs was used to estimate the activity loss during the first 14-hrs on stream. For this calculation the catalytically active sites were assumed to be accessible precious metal (by CO chemisorption). It was estimated that 18% of the catalytic sites were inactive after the first reforming cycle and 25% were inactive after the second cycle. However, in Chapter 4 we demonstrated that the amount of sulfur on a catalyst that had been on stream for a significantly longer period of time (105-hrs) without regeneration had a S:PM ratio of less than 3:100. Thus, it was unlikely that sulfur was the cause of the more rapid

deactivation measured after regenerations in Figure 5.2. However, to provide additional verification that sulfur was not the cause of the faster deactivation in subsequent reforming cycles, regeneration tests were performed with sulfur-free fuels.

To determine whether the irreversible deactivation in Figure 5.3 also occurred in the absence of sulfur, reforming tests were performed at high space velocity conditions (washcoat loading = 0.5 g/in^3, monolith GHSV = 44,000 h^{-1}) at which deactivation was measureable with both pure ethanol and sulfur-free E85. During steam reforming of both sulfur-free E85 and pure ethanol, deactivation rates were higher after regenerations. Further, the deactivation rates increased more significantly after the catalyst had been on stream for longer periods of time. The catalyst performance while reforming the sulfur-free E85 is shown in Figure 6.9.

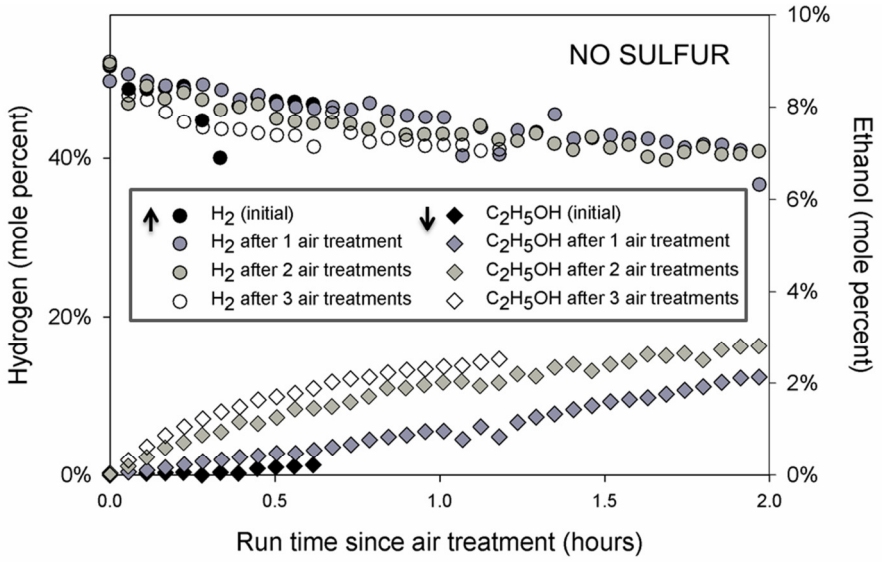

Figure 6.9: Reforming sulfur-free E85 with steam/carbon = 1.8, washcoat loading = 0.5 g/in^3 and GHSV = 44,000 h^{-1}, Air regeneration condition = 50% air/N_2

The results of these tests verified that the irreversibility described in Chapter 5 was not solely a consequence of sulfur poisoning. Based on these results it is likely that the irreversible aspect is due to another form of deactivation. Additional hypotheses are explored in the next chapters.

6.6 Conclusions

In previous chapters, the influence of sulfur on catalyst stability was demonstrated. In a 105-hr test, conversion decreased from 100% to 21%, however, low levels of residual sulfur were measured on the spent catalyst (0.03 at%). It is unlikely that such small amounts of sulfur are the sole cause of deactivation. Therefore, in this chapter, we proposed to study whether the extent of deactivation attributed to sulfur was caused by adsorbed sulfur

species that altered catalyst selectivity towards coke formation. In this chapter it was shown that sulfur increased the catalyst selectivity towards ethylene, a known precursors and acetaldehyde, another potential coke precursor. Further, results in this chapter confirmed the hypothesis that sulfur increased coking rates.

In addition to these tests, both reactor studies and TGA adsorption studies were used to determine the reversibility of sulfur poisoning. TGA adsorption tests found that H_2S adsorption was reversible in the presence of H_2 (and absence of sulfur). These tests indicated that sulfur adsorption was reversible in reducing conditions. Reactor tests found that only a small degree of activity was restored by removing sulfur from the feed. However, the reversibility of sulfur adsorption at these conditions could not be quantified due to the compounded impacts of sulfur and coking on catalyst activity. Reactor tests also indicated that sulfur adsorption may directly influence the selectivity of the catalyst to ethylene which decreased in concentration after sulfur was removed from the feed.

To determine whether the irreversible element of deactivation observed in the previous chapter was the result of sulfur poisoning, tests were performed using a sulfur-free fuel. During tests with both pure ethanol and sulfur-free E85, air treatments did not fully restore performance of a

catalyst. These results provided further evidence that sulfur was not the cause of the irreversibility described in the Chapter 5.

Chapter 7 : Coke formation

TPO results in Chapter 6 demonstrated that coke was formed on the catalyst after steam reforming the sulfur-free or sulfur-containing E85. TPO is a method to determine the form of coke on the surface. As discussed in Section 2.2.2, the form of coke during steam reforming can range from amorphous, polymeric coke to more graphitic forms. Further, the type of coke on the catalyst may change with TOS. For instance, it has been reported that amorphous coke can become more graphitic after high temperature treatment or after extended TOS [8, 60]. Graphitic forms of coke are less reactive and therefore harder to remove from the surface. Thus it is important to identify the form of carbon on the surface and understand how it is impacted by TOS.

In this chapter the impact of TOS on the type of coke that is formed on the catalyst during E85 SR is investigated. To accomplish this, coke on catalysts that have steam reformed E85 for different amounts of TOS is characterized using methods such as TPO, Raman spectroscopy and XPS. Additionally, the success of air treatments at removing coke is assessed by examining regenerated catalysts for residual coke. The results of these studies were used to determine whether the irreversible deactivation observed in Chapter 5 may result from residual, refractory coke species that are not removed by the air regenerations.

7.1 Coke formation over time

The type of coke species on the catalyst was studied by ex-situ characterization methods performed on catalysts that had been exposed to different TOS. Thus, the characterization of these samples provided a "snapshot" of the catalyst at several points during a 12-hr steam reforming process. The samples were generated from reactor tests conducted at 650°C, with S/C = 1.8, and GHSV of 22,000 h^{-1}. The deactivation profile for the 12-hr sample is shown in Figure 7.1.

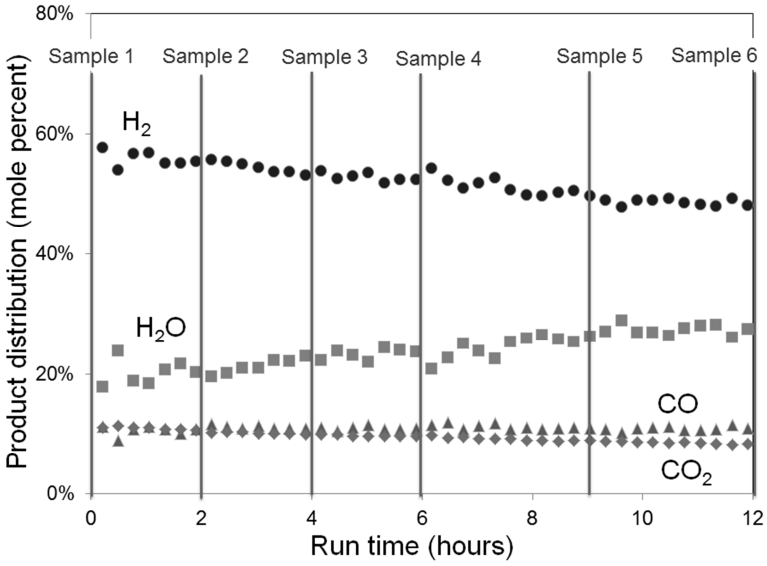

Figure 7.1: Reforming E85 with 5 ppm with conditions: S/C = 1.8, 250 mg catalyst, 3:1 wt ratio quartz:catalyst, GHSV = 22,000 h^{-1}

The catalysts that were characterized had been on stream for 0, 2, 4, 6, 9 or 12-hrs. TPO, Raman spectroscopy, and XPS were used to study the amount of coke and the type of coke on the samples.

7.1.1. Coke analysis by TPO

TPO was performed on samples that had been on stream for 2, 4, 6, 9 and 12-hrs on stream. During TPO, coke, of the form C_xH_y, is fully oxidized to CO_2 and H_2O. Neither CO nor H_2 was measured in the effluent during the series of tests. The CO_2 measured during TPO tests on the used catalysts are shown in Figure 7.2.

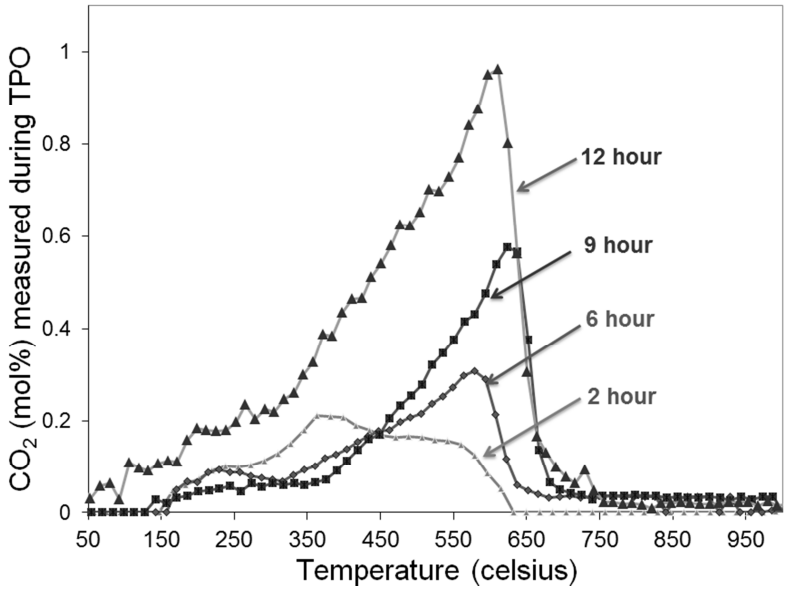

Figure 7.2: CO_2 measured during TPO (5% O_2/He with heat rate = 7°C/min) on samples that had steam reformed E85 for varying TOS (Figure 7.1)

As shown in Figure 7.2, higher temperatures were required to burn-off the carbon after the catalyst had been on stream for 9-hrs rather than after 2-hrs or 6-hrs. The burn-off temperature for the 9 and 12-hr samples was consistent (complete burn-off by 675°C). The TPO profiles for the 9 and 12-hr samples were consistent with the TPO profile of a 105-hr sample discussed

previously in Chapter 4 (Figure 4.5). Carbon burn-off on the 105-hr sample occurred between 500-650°C.

By integrating the CO_2 measurements in Figure 7.2, the total carbon accumulated as a fraction of the catalyst weight was calculated. These results are shown in Figure 7.3. As expected, the amount of coke on the catalyst increased with TOS.

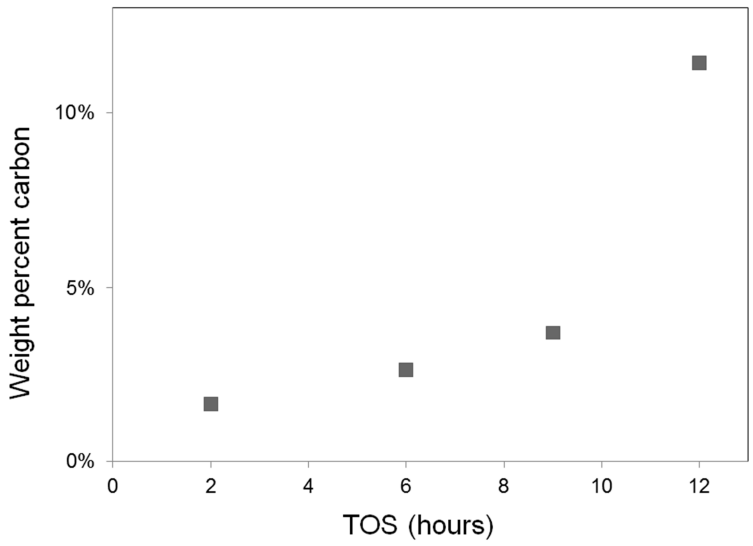

Figure 7.3: Weight percent carbon measured during TPO on catalysts that had steam E85 for varying TOS (Figure 7.1)

The coking rate in Figure 7.3 most closely resembles an exponential growth curve. However, the total carbon on the surface is not a simple indicator of the extent of deactivation, particularly, if different types of coke species are present on the surface. The relationship between coke and activity is further explored in the next sections.

More graphitic forms of coke have higher C/H ratios then amorphous forms. Thus, if the C/H ratio of the coke decreases with TOS it is an indicator that the coke is becoming increasingly graphitic. By integrating the concentrations of CO_2 and H_2O in the TPO effluent, the C/H ratio was calculated. The results of this calculation are shown in Figure 7.4. The results show that the coke becomes increasingly dehydrogenated with TOS. In the next sections this result is confirmed by studying the relative number of C-C and C-H bonds using Raman spectroscopy and XPS.

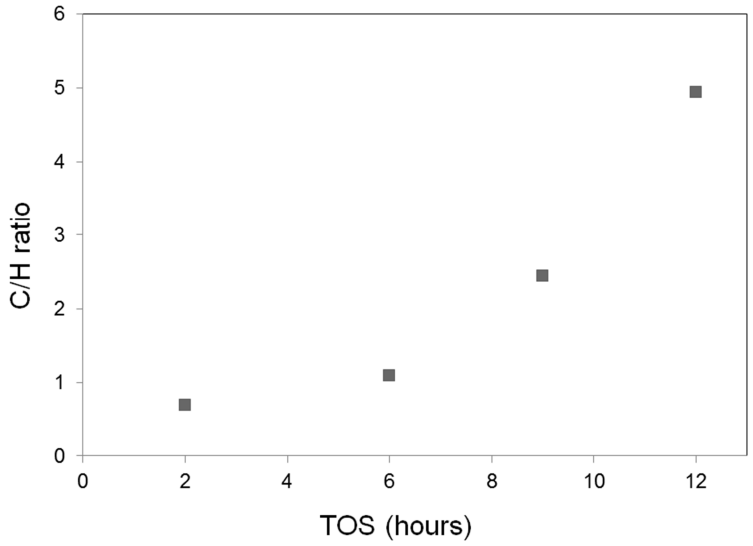

Figure 7.4: C/H ratio, calculated from CO_2 and H_2O measured during TPO on catalysts that had steam reformed E85 for varying TOS (Figure 7.1)

7.1.2. Coke analysis by Raman Spectroscopy

Raman spectroscopy can be used to quantify changes from amorphous to more graphitic forms of coke. For instance, the transition from a disordered carbon species to a more organized, graphitic structure is frequently characterized by a decrease in the D-band (disordered) peak expected at 1350 cm^{-1} and an increase in the G-band, (graphitic) peak at 1580 cm^{-1} [25, 121]. The ratio of these two peaks can be used to measure the degree of order of the carbon; lower D/G ratios indicate more ordered, graphitic species. Here, Raman spectroscopy was performed on catalyst samples that had been exposed to 4, 9, or 12-hrs on stream. As shown in Figure 7.5 and Table 7.1, the 12-hr sample has a considerably lower D/G ratio, and thus more graphitic carbon then the 4-hr sample. The average grain size of the coke (La) was calculated according to the Tuinstra and Koenig relationship [121-123].

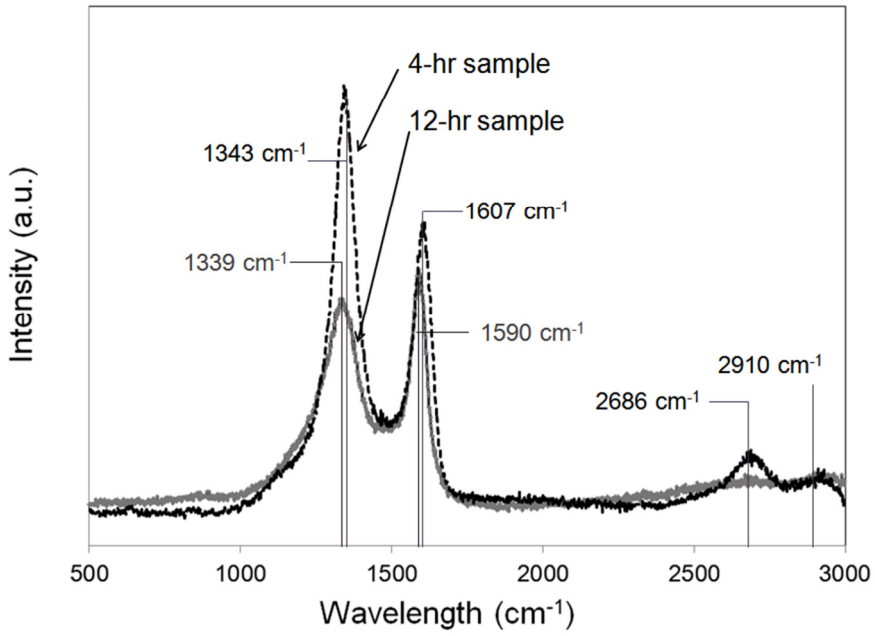

Figure 7.5: D-band and G-band Raman peaks measured on 4 and 12-hr samples

Table 7.1: Comparison of D-band and G-band Raman shift for 4-hr, 9-hr and 12-hr samples

Sample	D-band position (cm^{-1})	G-band position (cm^{-1})	D/G	La (nm)
4-hr sample	1343	1607	1.482	2.968
9-hr sample	1343	1599	0.986	4.338
12-hr sample	1339	1590	0.876	5.022

In addition to the D/G ratio, additional evidence for the increasingly graphitic nature of the coke species is demonstrated by changes in shape and position of the identified D and G peaks. An additional and smaller disordered peak exists at 1610 cm^{-1}, (within the graphitic peak measurement), thus, down shifts in the G-band position are indications of increasingly graphitic carbon [124]. The shift in the G-band position from

1607 cm^{-1} on the 4-hr sample to 1590 cm^{-1} on the 12-hr sample is further evidence that the carbon is becoming increasingly ordered. Lastly, an initial shoulder peak at 1250 cm^{-1}, attributed to C-H vibration and thus associated with amorphous and more hydrogenated coke formations [124], is measureable for the 4-hr sample only, and not for either the 9 or 12-hr sample. Therefore, Raman test results were aligned with TPO results.

7.1.3. Coke analysis by XPS

XPS was another method used to identify the type of coke species on aged catalysts. In agreement with both TPO and Raman results, it was shown that coke became increasingly graphitic with longer TOS. The graphitic carbon peak located at 283.7 eV (ubiquitous carbon is 285 eV) becomes increasingly prominent on the longer aged samples (this is demonstrated by a shift to lower binding energies in the carbon peak). The binding energies of the C1s peak are shown in Figure 7.6.

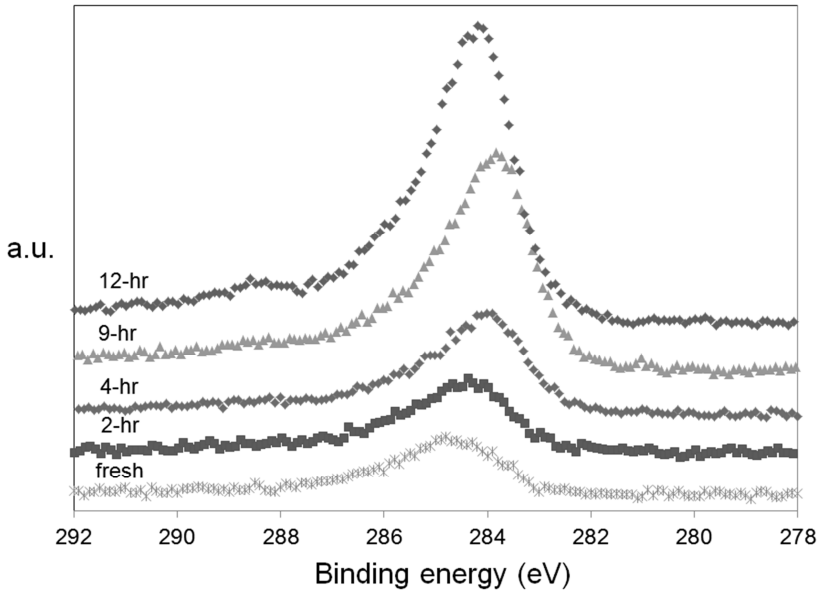

Figure 7.6: XPS binding energies of carbon 1s on samples that had steam reformed E85 for varying TOS (Figure 7.1)

Interestingly, the 12-hr sample had a peak at 288.6 eV, a binding energy assigned to carbonate or a C=O species [125]. Carbonate is not frequently reported on steam reforming catalysts. However, a carbonate peak on a Pt/ZrO_2 catalyst was reported by Yamazaki et al after bioethanol reforming [59]. An ethanol reforming mechanism that produces acetone may further decompose to produce carbonate species.

A quantitative assessment of the amount of graphite on the surface was performed by de-convoluting the C1s peak. The amount of graphite was plotted as a function of TOS and compared with a plot of the catalyst activity as a function of TOS. This result is shown in Figure 7.7. The activity data is plotted in the form of ethanol measured in the effluent.

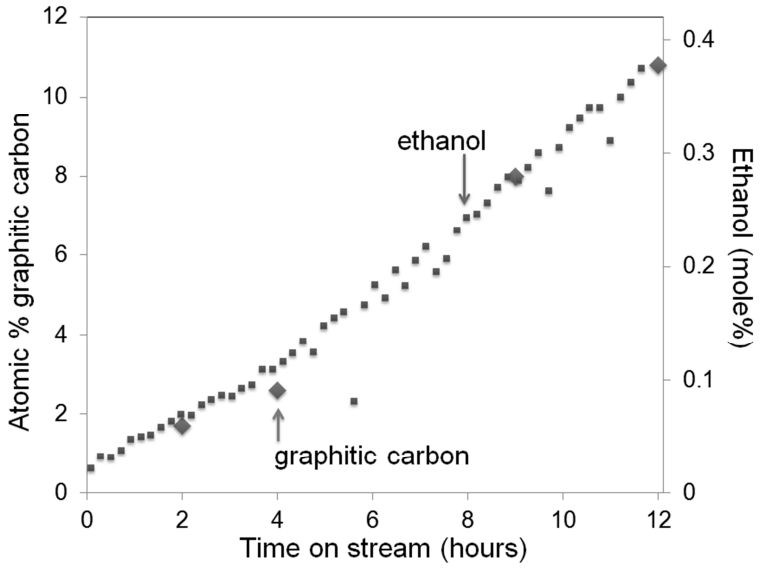

Figure 7.7: Activity (ethanol) and graphitic coke as a function of TOS

The results in Figure 7.7 may indicate that it is not the total carbon on the surface, but the amount of graphitic carbon that impacts performance. It is possible that more than one species of coke exist on the catalyst. TEM images revealed morphologies characteristic of whisker-like carbon on catalysts that had been on stream for 2-hr and 6-hr (image of 6-hr sample shown in Figure 7.8). It is possible that the whisker-like coke becomes a more encapsulating form of coke with TOS.

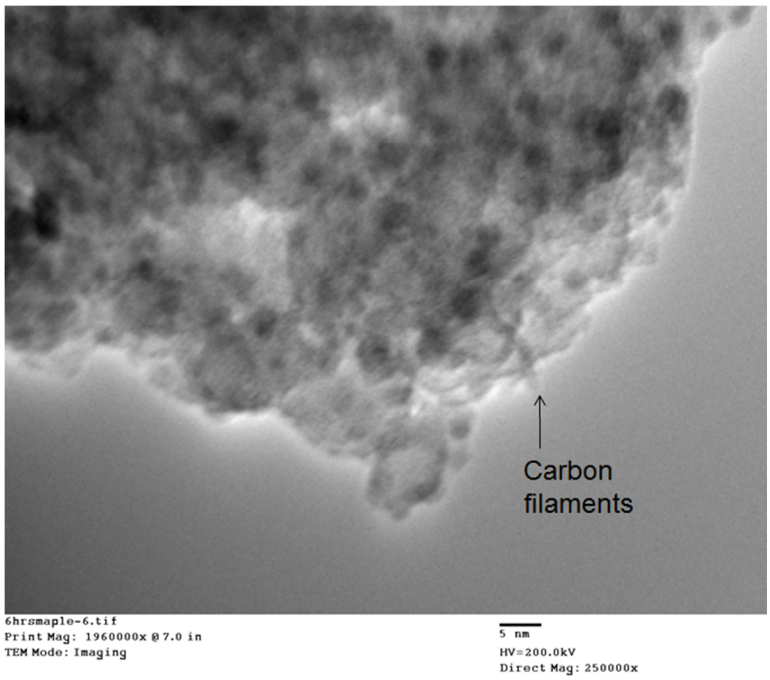

Figure 7.8: TEM image depicting filamentous coke on catalyst after 6-hrs steam reforming E85

In this section we provided further evidence that carbon becomes increasingly graphitic with TOS. Through TPO, Raman, and XPS it was shown that both the amount of coke and degree of dehydrogenation of the coke increase with TOS. The implication is that the coke may be harder to remove with air regenerations performed after longer TOS. The success of air treatments at removing coke is studied in the next section.

7.2. Regeneration of coked catalysts

As demonstrated in the previous section, coke becomes more graphitic with longer TOS. Regenerations may not be successful at removing the more

ordered carbon species. Thus, regenerations may not be successful after extended TOS. To test this hypothesis, TPO was performed on catalysts that had been exposed to 12-hrs steam reforming E85 followed by air regeneration in the reactor. If coke remained on the surface after regenerations, indicating it required temperatures higher than 650°C to remove, TPO would measure the oxidation of these species between 650-1000°C. However, it was found that catalysts that had been regenerated in the reactor after 12-hrs on stream did not have carbon burn-off at any temperature up to 1000°C. These TPO results, shown in Figure 7.9, indicate that coke is fully removed from the surface during air treatment.

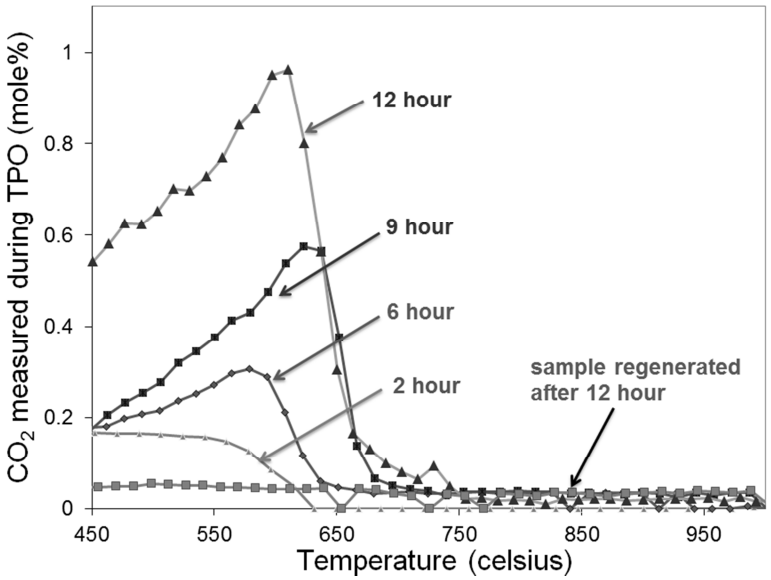

Figure 7.9: CO_2 measured during TPO (5% O_2/He with heat rate = 7°C/min) of samples that had varying TOS and on sample that had been regenerated after 12-hrs on stream

Similar to the TPO results, Raman spectroscopy did not detect either the disordered or graphitic carbon bands on the sample that was regenerated after 12-hrs of reforming. Therefore, there was significant evidence that coke was fully removed from this sample using air at 650°C.

In addition to the characterization performed on the 12-hr aged and regenerated sample, characterization was performed on a sample that had performed E85 steam reforming for 105-hrs (Figure 4.5). As discussed previously in Section 4.3, TPO of this sample revealed full carbon burn-off by 700°C. Further, after exposing the 105-hr sample to a 1-hr 650°C air treatment (ex-situ) graphitic carbon was not measureable on the surface by either XPS or TPO analysis.

Coke was not measured on samples after air treatment; however, the oxidation of the carbon species during the regeneration may generate high surface temperatures. It is possible that these high surface temperatures cause additional deactivation. Further, since the amount of coke and the degree of dehydrogenation of the coke increase during TOS, surface temperatures are expected to be higher during regenerations performed after longer TOS. Utilizing the results from TPO (Figure 7.3), the thermal energy released by oxidizing the total carbon on used samples was calculated. Assuming heat transfer at the gas-solid interface (and stagnant gas) the expected increase in surface temperature during the regeneration of these

samples was calculated. These results are shown in Table 7.3. The details of these calculations are given in Appendix B.4.

Table 7.2: Calculated increases in surface temperature that would be expected from oxidation of coke quantified in Figure 7.3

TOS	wt% C	ΔT (°C)
2	1.7%	52
4	2.9%	88
9	3.7%	116
12	11.5%	346

The results demonstrate that increasingly high temperatures will be generated on the catalyst during regenerations performed after longer TOS. In the next chapter the impacts of high temperature on the catalyst chemistry and morphology is investigated.

7.3 Conclusions

In this chapter it was demonstrated that the amount of coke on the surface increases with TOS and becomes increasingly dehydrogenated. Higher degrees of dehydrogenation indicate an increasingly graphitic type of coke. Although graphitic coke may require high temperatures and longer periods of time to oxidize from the surface [126], air treatments at 650°C successfully removed coke from the catalyst. Thus, the results of the last two chapters demonstrated that neither coke formation nor sulfur poisoning was implicated for the irreversible deactivation identified in Chapter 5.

Although the air treatments removed coke, it is possible that regenerations performed after longer TOS produce higher exotherms in the catalyst bed. Therefore, if high temperature oxidizing environments detrimentally impact the catalyst, the coke may indirectly cause the irreversibility discussed in Chapter 5. This theory is investigated in the next chapters.

Chapter 8 : Carrier deactivation mechanisms

The results of Chapter 6 demonstrated that sulfur poisoning was not the cause for the irreversible deactivation observed in Chapter 5. The results of Chapter 7 found that residual coke was also not the cause of the irreversible deactivation. To identify what type of deactivation was responsible, a series of ex-situ characterizations were performed to observe whether changes to the catalyst carrier occur during either TOS or regenerations. There are two primary deactivation mechanisms that can afflict the SiO_2-ZrO_2 carrier. First, changes in the carrier chemistry can occur, altering catalyst selectivity. Second, the porous carrier can lose surface area decreasing the accessibility of catalytic sites.

In studies on SiO_2-ZrO_2 carriers with similar formulations it has been reported that isolation and growth of ZrO_2 crystals can occur during high temperature treatment. As discussed in Section 2.4, the degree of interaction between ZrO_2 and SiO_2 can influence properties such as the thermal stability of the carrier, the acidity of the carrier, and the bonding between the carrier and precious metal. In order to determine whether 'demixing' of the SiO_2-ZrO_2 carrier occurs during the steam reforming or regeneration conditions, the degree of crystallization of ZrO_2 on catalysts is measured utilizing XRD. XPS is also used to study changes in the binding energy of the Si and Zr.

A common catalyst deactivation mechanism is temperature-induced carrier sintering. Carrier sintering is particularly a problem when exothermic reactions create high surface temperatures reducing the surface area of the support and collapsing catalyst pores. Therefore, it is more common during PROX or ATR than during the endothermic steam reforming process. Therefore, in this study, carrier sintering is more of a concern during oxidative regenerations that may incur high surface temperatures. The impact of high temperature air treatment on the BET surface area of the catalyst is studied in Section 8.2.

8.1 Changes to the carrier during TOS

8.1.1. XRD analysis

The impact of TOS on the morphology of the catalyst carrier was determined with XRD analysis. It has been reported that SiO_2-ZrO_2 supports (with Si/Zr ratios similar to those used in this study) are mainly amorphous after calcination with a weak band at 31° [87]. The fresh catalyst used in this study was also found to be primarily amorphous with a weak band at 31°, indicating that any isolated zirconia crystallites were small.

The diffraction patterns for samples that had reformed E85 for 2, 9 or 12-hrs are shown in Figure 8.1. Two crystalline structures were discerned on

all three samples. The first was a tetragonal structure associated with isolated ZrO_2. In addition to this structure, a wide peak at approximately 40° was identified and is likely associated with precious metal particles. The primary peak for monometallic Rh, monometallic Pt, or a Rh-Pt alloy, would exist between 39.6° and 41°. The presence of the primary (002) graphite peak, expected at approximately 25° is not identifiable on any sample; however, this may be due to the broad amorphous silica peak in this position.

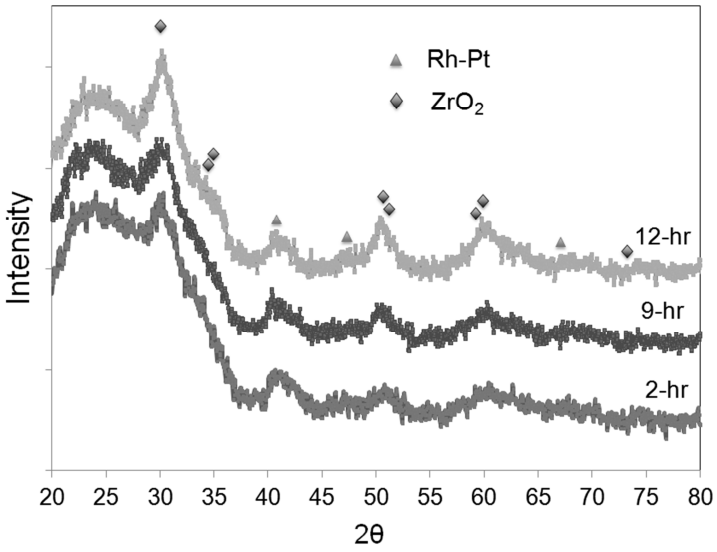

Figure 8.1: XRD profiles for samples that had reformed E85 for varying TOS. Referenced peaks = tetragonal ZrO_2 (ICDD No. 42-1164) and orthorhombic Rh-Pt (ICDD No. 65-7938)

The XRD patterns for the 2, 9, and 12-hr samples in Figure 8.1 indicate that isolation and growth of zirconia crystallites (zirconia sintering) may occur and increase with TOS. It has been reported that high temperature air treatment causes the isolation and sintering of zirconia on SiO_2-ZrO_2 carriers [87], however, reports of this behavior during steam

reforming conditions have not been identified. Particle agglomeration can be studied by measuring XPS atomic intensity ratios for the support and supported compound. In the next section XPS provides additional evidence for zirconia sintering.

8.1.2. XPS analysis

The impact of TOS on the chemistry and morphology of the support was further investigated with XPS. Interaction between Zr and Si oxides is signified by a decrease in Si binding energy and an increase in Zr binding energy (relative to the binding energy in the individual oxides) [127, 128]. Specifically, relative changes of the Si binding energy of -0.6 eV (from a SiO_2 reference of 103.7) and increases in Zr binding energy of between 0.7-1.2 eV (from a ZrO_2 reference of 182.1 eV) have been reported [127]. Similar to these studies, the fresh catalyst had higher Zr binding energy (182.7) and lower Si binding energy (103.2) than the references for the isolated oxides. Therefore, XPS results on the fresh catalyst suggest a degree of interaction between the two oxides.

The interaction between silica and zirconia was studied as a function of TOS by monitoring changes in the binding energy and the relative intensity ratios of each element. The binding energy of the two elements did not change significantly, however, differences in the intensity ratio of the

elements (I_{Si}/I_{Zr} ratio) were observed. The relative compositions of Si and Zr, (calculated from the intensity ratios) on the fresh and aged catalysts are given in Table 8.1. The I_{Si}/I_Z ratio increases with TOS. This same trend was found comparing a fresh monolith catalyst and a monolith catalyst that had reformed a sulfur-containing fuel for 105-hrs (Table 8.2).

Table 8.1: Surface composition (atomic percentages) of Si, Zr measured by XPS for samples that had steam reformed E85 for 2, 4, 9 or 12-hrs (Figure 7.1)

	Fresh catalyst	2-hr	9-hr	12-hr
Si	30.9	30.9	25.4	23.3
Zr	2.9	2.8	2.2	2
nSi/nZr	10.66	11.04	11.55	11.65

Table 8.2: Surface composition (atomic percentages) of Si, Zr measured by XPS for fresh and used washcoated monoliths after steam reforming E85 (Figure 4.5)

	Fresh catalyst	105-hr
Si	31	18.9
Zr	2.6	1.1
nSi/nZr	12.0	17.8

Three hypotheses are proposed for the behavior in Tables 8.1 and 8.2. First that the growth of zirconia crystallites lead to lower zirconia dispersion resulting in higher observed I_{Si}/I_Z. It has been demonstrated that the XPS atomic intensity ratio of a supported metal can be used to calculate its dispersion [129]. Using a similar SiO_2-ZrO_2 formulation, Meijers et al measured decreases in the I_{Si}/I_Z (by XPS) and implicated lower dispersions of zirconia on silica [88]. The second hypothesis is that the change in I_{Si}/I_Z is caused by a higher propensity for coke to form on the zirconia than on the

silica. In this case, coke would shield the Zr resulting in a lower intensity signal relative to the Si. However, as shown in Section 8.2, the I_{Si}/I_Z ratio is higher on samples regenerated after TOS (thus without carbon formation) than on fresh catalysts. The third hypothesis is that lower I_{Si}/I_Z ratios are caused by a shielding effect by the precious metal due to a SMSI interaction. Ryndin et al proposed that a SMSI between Pd and Zr in a Pd/ZrO_2-SiO_2 catalyst increased the relative intensities of the I_{Si}/I_{Zr} peaks and increased the overall binding energy of the Zr [130]. Thus, it is also possible that the results indicate more complex changes to the catalyst-carrier interaction occur with TOS.

8.2 Changes to the carrier caused by regeneration conditions

8.2.1 BET surface area

Catalyst carriers can lose surface area by a process known as carrier sintering. Carrier sintering is typically temperature-induced. Thermally induced sintering has been reported for most common carriers including Al_2O_3, CeO_2, ZrO_2, and mixed oxides such as CeO_2-ZrO_2. During catalyst regenerations exothermic carbon burn-off may produce high temperatures. Therefore, the thermal stability of the SiO_2-ZrO_2 carrier is a concern. To determine whether regenerations, particularly after longer TOS (and higher

carbon build-up) decreased carrier surface area, single-point N_2-desorption BET surface area was measured on catalysts that had undergone varying TOS followed by a regeneration treatment. These results were compared to the BET surface area of a fresh catalyst. The results of these tests are shown in Table 8.3. Because coke formation can change the surface area of samples, surface area was only measured after oxidative treatment.

Table 8.3: Single point N_2 BET surface area for catalysts that were regenerated after steam reforming sulfur-containing E85 for 12, 18, or 24-hrs performed.

Sample	BET surface area m^2/g
Fresh catalyst	200
12-hr with 1 regeneration	185
12-hr with 2 regeneration	180
18-hr with 1 regeneration	189
24-hr with 2 regeneration	217

All BET surface area measurements were within 10% of the value for the fresh catalyst and no consistent trend was discernable between samples that had been regenerated after longer periods of time. Thus, sintering of the catalyst carrier was not observed.

8.2.2. XRD analysis

In Section 8.1, the fresh SiO_2-ZrO_2 carrier was shown to have an amorphous structure. Further, it was shown that zirconia crystallites might increase in size during TOS. To determine whether regenerations might

cause similar behavior, XRD was performed on catalysts that had been calcined at 550, 650, 750, and 850°C. The results of these tests are shown in Figure 8.2. Peaks associated with tetragonal zirconia became sharper after calcination at 850°C.

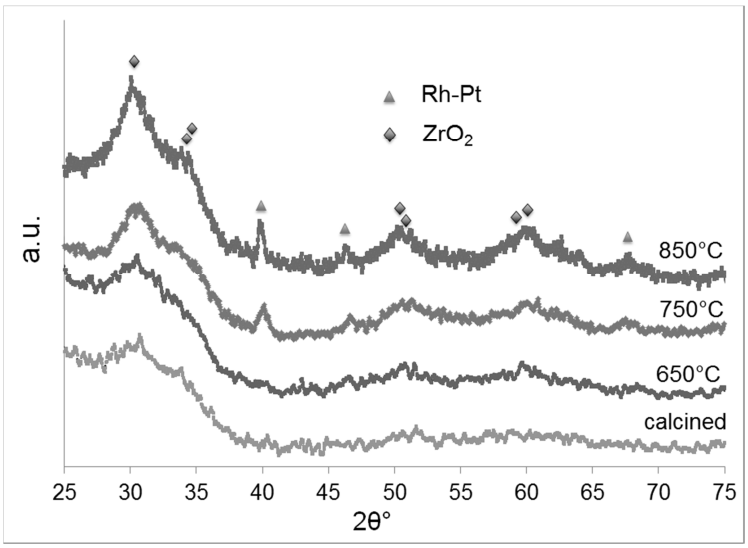

Figure 8.2: XRD patterns for samples calcined at: 550°C (2-hr), 650°C (1-hr), 750°C (1-hr) and 850°C (1-hr)

As expected from the literature on SiO_2-ZrO_2 supports, the results indicate that growth and isolation of zirconia crystallites occurs after high temperature air treatment. Thus, catalysts regenerated after longer TOS (and exposed to higher surface temperatures) may have lower zirconia dispersion. In addition to peaks associated with the tetragonal zirconia, Figure 8.2 exhibits an increasingly sharp peak assignable to the precious metal. This result indicates that precious metal particle morphology may also be affected by catalyst regenerations. This theory is investigated in Chapter 9.

8.2.3. XPS analysis

Section 8.1.2 demonstrated that the I_{Si}/I_Z ratio was higher on catalysts that had steam reformed E85 for longer periods of time. In order to determine whether regenerations performed after longer TOS also had higher I_{Si}/I_Z than on the fresh catalyst the relative intensities of the species was measured for a fresh catalyst, a catalyst regenerated after 28-hrs of E85 steam reforming and a catalyst that had also steam reformed E85 for 28-hrs but with preemptive regenerations performed (Figure 5.4). Thus, although the same TOS was experienced for the used samples, the TOS was not continuous for the catalyst with preemptive regenerations. The catalyst that had preemptive regenerations would have had lower coke burn-off and consequently lower surface temperatures during the regenerations. The I_{Si}/I_Z ratio measured on these samples is shown in Table 8.4.

Table 8.4: I_{Si}/I_Z (XPS) for a fresh catalyst, a catalyst regenerated after 28-hrs (continuous TOS), and a catalyst that had 'cyclic' regenerations with 28-hrs total TOS (Figure 5.4). Surface and ground washcoat samples measured.

	Fresh	Fresh ground	28-hr continuous	28-hr continuous ground	28-hr cycled	28-hr cycled ground
nSi/nZr	11.90	11.40	14.90	13.90	11.90	11.60

The results in Table 8.4 demonstrate that the I_{Si}/I_Z for the fresh catalyst is the same as that for the cycled catalyst. However, a significant increase in the I_{Si}/I_Z is measured on the continuously aged sample. This result indicates that preemptive regenerations were able to maintain the

morphology of the catalyst carrier. The impact of the zirconia isolation on catalyst performance and also on precious metal morphology is an interesting area for future research.

8.3 Conclusions

In this chapter it has been shown that zirconia crystals may isolate from the catalyst carrier. This effect was measured using XRD and observed on samples after both steam reforming conditions and after high temperature air treatment (850°C). The relative intensities of the Si and Zr XPS signals on the used samples provided additional evidence that zirconia might sinter at these conditions. Thus, in this chapter it was demonstrated that changes to the carrier morphology may occur with both TOS and during regenerations. Further, the ratio of the XPS Si and Zr peak intensities indicated that preemptive regenerations can maintain the carrier morphology. The isolation and sintering of zirconia may have implications for the metal-support interaction, the surface acidity (and thus propensity for coke formation) and the metal dispersion.

In addition to identifying the increasingly strong bands associated with tetragonal zirconia, XRD results also revealed that precious metal peaks became identifiable after treating the catalyst with air at 750°C. This result

indicated that precious metals particles may sinter during air regenerations. This hypothesis is investigated in the next Chapter.

Chapter 9 : Precious metal deactivation mechanisms

In the previous chapters the impact of both TOS and air regeneration were studied on coke formation, sulfur poisoning, and the morphology and chemistry of the catalyst carrier. In this chapter, potential deactivation mechanisms that would affect the precious metal particles are investigated. One potential cause of deactivation is precious metal sintering. As discussed in Section 2.5, during precious metal sintering the growth of precious metal particles reduces the amount of accessible catalytic sites. Metal sintering may occur during extended TOS but is more likely to occur during regenerations, which can expose the catalyst to high temperatures in an oxidizing environment. Preliminary evidence of precious metal sintering after high temperature air treatments was demonstrated by XRD in the previous chapter (Figure 8.2).

In addition to precious metal sintering, changes to the bonds between the precious metal components (Rh,Pt) such as alloy formation or alloy segregation could cause changes in catalyst performance. Alternatively, changes in the bonding between the precious metal and the carrier could also impact performance. In general, the analysis of such behavior is beyond the scope of this study, however, the characterization performed in this chapter can provide preliminary evidence of these behaviors. In this chapter, the

chemistry and structure of precious metal particles is investigated using XPS, CO chemisorption, and TPR.

9.1. Changes to the precious metal during TOS

9.1.1. CO Chemisorption

Precious metal sintering is typically measured by CO (or H_2) chemisorption. If precious metal particle size increases, fewer sites are available and the capacity to chemically adsorb CO is decreased. Coke can impact CO chemisorption results. Therefore, CO chemisorption was only performed on used samples that had been regenerated. These results are presented in the next section that investigates the impact of air regenerations on the precious metal. Further, it is more likely that particle sintering occurs during regenerations, in the presence of oxygen and high temperatures, than during the steam reforming conditions.

Although it is unlikely that precious metal sintering occurs during TOS, it is possible that other mechanisms occur during the steam reforming conditions that result in lower CO chemisorption capacity, namely, SMSI. SMSI is an effect which is caused by high temperature reducing environments (the effect is discussed in more detail in Section 2.2.5). In order to test whether SMSI impacted the catalyst during the steam reforming

conditions, CO chemisorption was performed on fresh catalysts that had been exposed to reducing conditions (4% H_2/N_2) at 650°C for varying periods of time. These results were compared with a fresh catalyst reduced at 400°C. The CO chemisorption capacity (μmol/g) are shown in Table 9.1.

Table 9.1: CO chemisorption capacity for samples after treatment in 4% H_2/N_2 at 650°C for varying time or at 400°C for 2-hr

CO chemisorption capacity (μmol/g) after H_2 treatment at 650°C	
1 hr	84.4
4 hr	85.1
9 hr	82.4
CO chemisorption capacity (μmol/g) after H_2 treatment at 400°C	
2 hr	88.2

No significant change in CO chemisorption capacity was measured between the fresh catalyst and catalysts that had been reduced at 650°C for varying periods of time. Thus, extended exposure to reducing conditions did not impact the morphology of the catalyst particles and it was unlikely that SMSI-type behavior was impacting the catalyst at these conditions.

9.1.2. XPS analysis

During steam reforming, the chemistry of the precious metal may change. For instance, due to changes in the bonds between the Rh and Pt or due to changes in the bonds between the precious metal and the carrier. XPS was performed to determine whether differences in the precious metal

binding energy or precious metal surface concentrations could be discerned between samples that had been on stream for different amounts of time. Binding energies and surface concentrations of the Rh and Pt were compared for the 0, 2, 4, 9 and 12-hr samples. The rhodium $3d_{5/2}$ and $3d_{3/2}$ binding energy is shown in Figure 9.1.

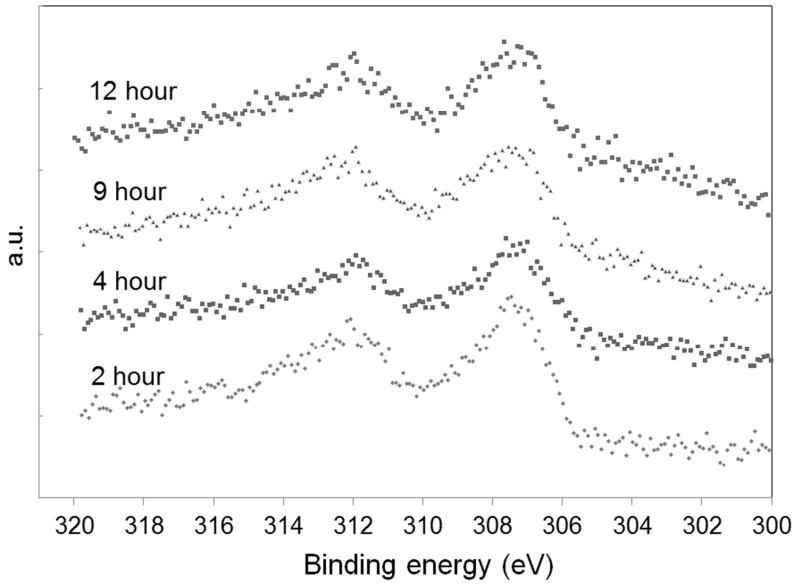

Figure 9.1: Rhodium binding energy for 3d 5/2 and 3d 3/2 peaks

Table 9.2: Atomic surface concentrations and binding energies (eV) for rhodium

	Binding energy (eV)				
	fresh	2-hr	4-hr	9-hr	12-hr
Rh^{+0}	NA	307.1	307.4	307.6	307.5
Rh^{+3} SMSI	308.7	308.4	NA	NA	NA
Rh^{+3} SMSI	NA	NA	NA	NA	NA
Pt^{+0}	71.2	71.4	71.5	71.4	71.7
Pt^{+2}	72.7	73.3	73.1	72.8	NA

NA = Not applicable

Neither changes to the rhodium binding energy nor changes to the platinum binding energy were observed with TOS. Significant trends were also not observed rhodium and platinum concentration data. Thus, neither CO chemisorption nor XPS results implied that precious metal particles were influenced by TOS.

9.2. The impact of regenerations on precious metal particles

9.2.1. CO Chemisorption and XRD analysis

To determine whether regenerations performed after longer TOS sintered catalyst particles, the CO chemisorption capacity of catalysts that had been regenerated after 12, 18 or 28-hrs on stream were compared to the CO chemisorption capacity of a fresh catalyst. Utilizing the CO chemisorption capacity, the total metal dispersion, a measure of the fraction of accessible sites, was calculated using equation 20:

$$M_d = \frac{metal\ accesible\ (g)}{total\ metal\ (g)} = \frac{n_{CO}}{S} \cdot \frac{M_{PM}}{\%PM \cdot g_{cat}} \quad (20)$$

In equation 20, n_{CO} is the number of moles of chemisorbed CO, M_{PM} is the average molecular weight of the precious metal, $\%PM$ is the precious metal loading (4.8wt%) and S is the adsorption stoichiometry which was assumed to be 1 (one CO molecule adsorbed per precious metal atom). The calculated dispersion values for a 12-hr, 18-hr and 28-hr aged and regenerated catalyst are shown in Table 9.3.

Table 9.3: Metal dispersion values measured by pulse CO chemisorption on catalysts exposed to 0, 12, 18 or 28-hrs on stream followed by regeneration (650°C air treatment)

Catalyst	Dispersion
fresh Rh-Pt/SiO_2-ZrO_2	22.0%
12-hr with 1 regeneration	11.7%
18-hr with 1 regeneration	8.6%
28-hr with 1 regeneration[1]	3.0%

1. Monolith catalyst with fresh dispersion = 31%

The samples that had been regenerated after longer TOS had lower dispersion. In most cases, CO chemisorption can be used as an indicator of particle size. By assuming a stoichiometry for adsorption, and a shape factor for the particles, an expected crystallite size can be calculated from CO chemisorption results. The particle sizes predicted from the dispersions measured on the fresh catalyst, the 12-hr, and the 18-hr samples are given in Table 9.4. Details on these calculations are provided in Appendix B.5.

Table 9.4: Calculated particle sizes for precious metal particles assuming 1:1 CO:PM adsorption

Catalyst	Calculated particle size (nm)
fresh Rh-Pt/SiO_2-ZrO_2	2.36
12-hr with 1 regeneration	4.35
18-hr with 1 regeneration	6.16

The results in Table 9.4 suggest that regenerations performed after longer TOS reduce the accessibility of precious metal sites. Extended TOS in steam reforming conditions may decrease metal dispersion, however, it was shown in Section 9.3.1 that extended exposure to reducing conditions did not impact CO chemisorption capacity. Further, it has been reported that sintering rates are exponentially dependent on temperature and that sintering rates for noble metals are higher in oxidizing rather than reducing conditions [60]. Therefore, it is likely that high temperatures during the air regenerations decrease dispersion. To provide further evidence that regeneration conditions rather than reforming conditions led to the dispersion losses in Table 9.3, CO chemisorption was measured on fresh catalysts that had been calcined for 1-hr at 650, 750, or 850°C in air. The results of these tests are shown in Table 9.5.

Table 9.5: Metal dispersion values measured by pulse CO chemisorption on catalyst exposed to high temperature air treatment at 650, 750 or 850°C for 1-hr

Calcined catalyst	Dispersion	Calculated particle size (nm)
650°C 1-hr	19.2%	2.8
750°C 1-hr	12.6%	4.2
850°C 1-hr	5.0%	10.6

Significantly lower dispersion was measured after high temperature calcination. These results are further evidence that the lower dispersions measured on the longer aged samples are caused by increasingly high temperatures produced by carbon burn-off during regenerations. Temperature is known to impact sintering rates. However, it is also possible that the oxidizing environment contributes to dispersion loss. To test this theory a fresh catalyst was treated at 850°C in helium (rather than air) for 1-hr. The resultant dispersion on this sample was 5.0%, the same dispersion measured on the sample treated with air at 850°C. Therefore, temperature was found to be the primary factor that was causing the changes in dispersion.

In this section it was found that regenerations performed after longer TOS reduce the chemisorption capacity of the metal. Sintering of precious metal particles due to high surface temperatures during air regenerations may cause the lower chemisorption capacity. In agreement with this hypothesis, decreases in dispersion were observed after high temperature calcination of fresh catalysts. These results are also in agreement with the

XRD results from Chapter 8 that revealed sharper peaks associated with the precious metal on samples after high temperature calcination. The XRD results in Chapter 8 were utilized to measure crystallite size to compare with the CO chemisorption data. The results of this analysis are described in detail in Appendix D. The particle sizes calculated using Scherrer analysis are shown in Table 9.6 below. The peaks associated with the precious metal particles were not identifiable on the samples calcined at either 550 or 650°C indicating that particle sizes were small (less than 5 nm).

Table 9.6: Particle sizes calculated from Scherrer analysis of (111) peak on XRD patterns of catalysts calcined in air at 550, 650, 750 and 850°C.

Calcination temperature (celsius)	FWHM (°)	Particle size (nm)
550	ND	ND
650	ND	ND
750	0.80	11.1
850	0.47	18.8

ND = not detected

The results of the XRD analysis were in agreement with the CO chemisorption results that particle size increased with increasing calcination temperature.

9.2.2. TPR analysis

The reduction temperature of a material can serve as an indicator for several factors relating to the chemistry and morphology of the metal. For instance, the nature of the metal-support bond impacts the metal reduction

temperature. It is well known that rhodium reduces at a lower temperature on a weaker binding support such as silica than it does on a stronger binding support such as zirconia or alumina [131]. Further, metals in strong interaction with the carrier (SMSI) exhibit higher reduction temperatures [132]. Precious metal particle size can also impact reduction temperature [133, 134]. Thus, differences in the reduction temperature of the aged samples can suggest whether there are differences in particle size or metal-support interaction.

During TPR tests, the catalyst is reduced according to equation 21, thus both hydrogen consumption and water production can be measured to evaluate the extent of metal reduction.

$$MO_x + xH_2 \leftrightarrow M + xH_2O \quad (21)$$

Since aged samples were in the metallic state and had considerable amounts of coking, the samples underwent a 650°C air treatment for 1-hr prior to TPR. During TPR, measurements were collected from the chemisorption (TCD) unit as well as from a micro-GC that was able to isolate and analyze individual gas species. Thus, three criteria: the TCD signal, decreases in H_2, and increases in H_2O, were used to identify and quantify reduction peaks.

Two major reduction peaks were identified during analysis: at 80-120°C and at 250-300°C. An additional small, wide peak occurs at approximately 600°C. The low temperature peak for samples that had been

on stream between 2, 9 and 12-hrs is shown in Figure 9.2. The low temperature peak is likely associated with a monometallic species and could be de-convoluted to two separate peaks on each sample except the 2-hr sample that had 3 distinct peaks. These peaks were located at approximately 79°C (2-hr sample only), 95°C and 110°C. The 250-300°C and 600°C peaks are shown in Figure 9.3 (both H_2 consumption and H_2O production shown). The peak at 250-300°C is likely associated with a Pt-Rh alloy [133] but could be associated with a hard to reduce monometallic Rh or Pt. The peak at approximately 600°C may be due to a hard to reduce metal species or due to some extent of ZrO_2 reduction. Other authors have reported reduction of ZrO_2 at this temperature [109].

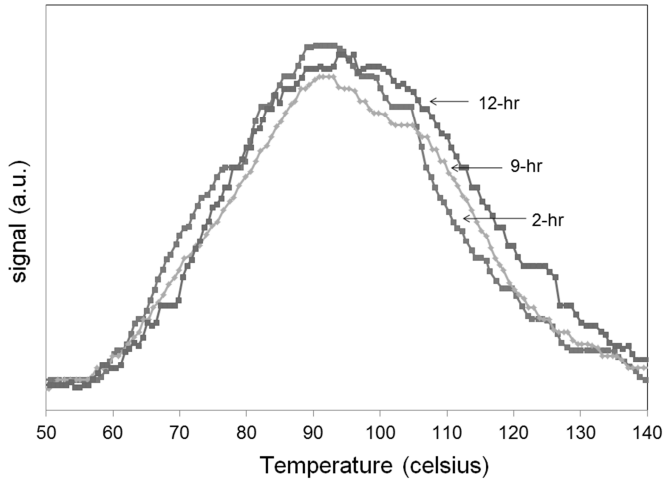

Figure 9.2: TCD signal measured during TPR (5% H_2/Ar with heating ramp = 7°C/min)

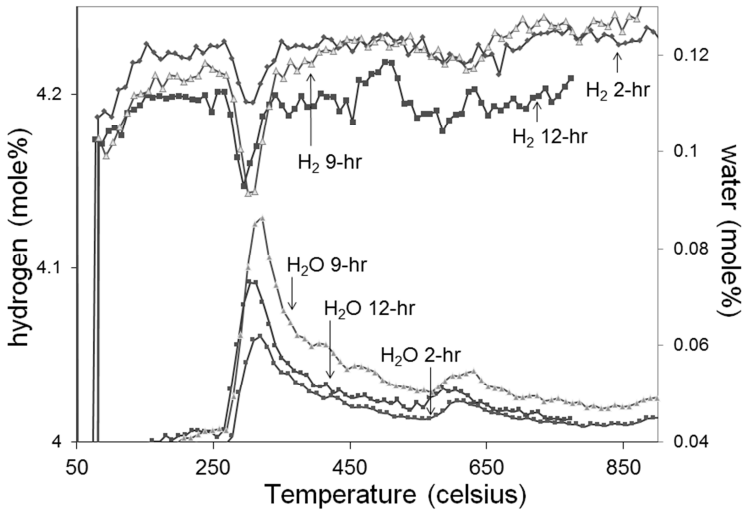

Figure 9.3: H_2 and H_2O measured during TPR (5% H_2/Ar with heating ramp = 7°C/min)

There were not discernible trends in the peak position or relative size of either of the higher temperature peaks. However, as shown in Figure 9.2, the position of the low temperature peak is shifted rightward on the x-axis for samples that had been on stream longer. There are several potential causes for the shift in peak position that occurs for the 80-120°C peak including changes in metal particle size, increased interaction between the metal and the support, or the metal becoming increasingly associated with zirconia rather than silica.

9.3 Conclusions

In this chapter it was shown that the chemisorption capacity of the catalyst (and corresponding dispersion) was impacted by calcination

temperature. Increasing the calcination temperature from 650 to 850°C decreased metal dispersion by 75%. Further, it was found that catalysts regenerated after longer TOS had lower CO chemisorption. This result suggested that higher surface temperatures, reached during regenerations (as calculated in Chapter 7), reduced the dispersion of the catalyst. This decrease may be due to an increase in particle size. XRD results presented in the previous chapter support this theory. These results suggest that the irreversible deactivation observed in Chapter 5 may be caused by precious metal sintering during the air regenerations.

Chapter 10 : Conclusions and future work

10.1 Conclusions

The purpose of this work was to identify the causes of deactivation during catalytic steam reforming of sulfur containing fuels and to recommend processes to improve stability. A commercially available Rh-Pt/SiO_2-ZrO_2 catalyst was used to steam reform E85, a commercial sulfur-containing liquid fuel. This fuel is present in service stations and could be reformed to produce hydrogen for fuel cell vehicles. The conditions used were energy efficient steam/carbon ratios and moderate temperatures. At these conditions, the addition of 5 ppm sulfur to the fuel caused significant catalyst deactivation. Rather than mitigate the impact of sulfur by changing the operating conditions, either by increasing the temperature or water concentration, the potential to incorporate catalyst regeneration techniques was investigated.

The only effective method to significantly restore catalyst performance was treating the catalyst with air. Even after extensive levels of deactivation (to less than 25% of initial activity), air regenerations were found to restore initial activity. However, deactivation occurred more rapidly after successive air treatments. This result indicated that some extent of the catalyst deactivation was not reversible or alternatively, that regenerations detrimentally impacted the life of the catalyst. Several possible causes of this

behavior were investigated. Since sulfur was found to be the primary cause of catalyst deactivation, the first hypothesis that was investigated was whether sulfur was not removed during regenerations and caused higher deactivation rates during subsequent steam reforming segments.

Although sulfur was found to deactivate the Rh-Pt/SiO_2-ZrO_2 catalyst to less than 21% of its initial activity (with no identified deactivation at these conditions in the absence of sulfur), the concentration of sulfur on the spent catalyst was low. Instead, high concentrations of surface carbon were detected on the spent catalyst. It was confirmed that sulfur increased coke formation by comparing TPO results on catalysts that had reformed either a sulfur-free or sulfur-containing fuel. Sulfur likely promotes coke formation by increasing the catalyst's selectivity towards ethylene, a known precursor. Thus, small amounts of adsorbed sulfur could significantly deactivate a catalyst by changing its selectivity towards ethylene and promoting coking. Tests performed at high GHSV with sulfur-free E85 indicated that residual sulfur poisoning was not the cause of higher deactivation rates after air regenerations.

The second hypothesis that was investigated was whether graphitic coke was not removed by air treatments and therefore caused more rapid deactivation after the regeneration. In Chapter 7 the amount and the type of coke was measured as a function of TOS using TPO, Raman and XPS. Both

the amount of coke and the degree of graphitization increased with TOS. Although graphitic coke may require higher temperatures and longer periods of time to oxidize than more amorphous forms, air treatments performed at 650°C were successful at removing the coke from the surface. However, regenerations performed after longer TOS produce higher exotherms in the catalyst that were found to impact the structure of the catalyst.

CO chemisorption measurements were found to be lower on catalysts that were regenerated after longer TOS. This result indicated that the precious metal particles might be sintering. Further, it was found that increasing the calcination temperature of a fresh catalyst from 650 to 850°C decreased its metal dispersion by 75%. Additionally, catalysts calcined at higher temperatures had sharper XRD peaks associated with both the precious metal and tetragonal zirconia. These results indicated that regenerations, which expose the catalyst to high burn-off temperatures, reduce the amount of accessible precious metal by sintering the precious metal particles.

In addition to the changes to the precious metal, changes to the catalyst carrier were also observed after regenerations performed after longer time on stream. XRD results indicated that zirconia crystals may isolate from the SiO_2-ZrO_2 carrier and sinter during both time on stream and during air regenerations. Although the impact of these changes in carrier morphology

are not known, performing air regenerations after shorter periods of time on stream was found to limit this effect.

An additional finding of this thesis was that preemptive air regenerations were successful at improving catalyst stability. Preemptive regenerations result in lower surface temperatures during the oxidation of coke. Thus, preemptive regenerations can limit the degree of precious metal and zirconia sintering that may occur during time on stream. The time between regenerations has been found to be an important factor to optimize in order to run a steam reforming process with sulfur-containing fuels.

10.2 Future work

This thesis demonstrated the potential of a preemptive regeneration process that can maintain catalyst stability during steam reforming of sulfur-containing fuels. Optimizing this process is an important area for future research. Additionally, the preemptive regeneration process could be investigated for the steam reforming of other sulfur-containing fuels. Another area for future research could focus on optimizing the catalyst formulation. Specifically, the catalyst formulation could be improved to prevent sintering. Lastly, an interesting finding of this work is that preemptive regenerations maintain the carrier morphology. Thus, studying the impact of changes in carrier morphology on catalyst performance and precious metal dispersion is

another area for potential research. Additionally, specific studies that relate to the deactivation measured in Chapters 6-9 are outlined below:

Sulfur poisoning

- In Chapter 6 it was shown that sulfur increased both the production of acetaldehyde and ethylene. Ethylene was observed to decrease immediately upon removal of H_2S whereas acetaldehyde increased upon removal. It is well reported that ethanol dehydrates to ethylene on acidic sites. Thus, it was proposed that H_2S increased the surface acidity which led to higher ethylene production and coke formation. The increases in acetaldehyde and corresponding changes in C_1 product distributions were proposed to occur due to the coke rather than the presence of sulfur. Therefore, doping the reactants with ethylene should have a similar effect as doping the reactants with H_2S. Studying the impact of ethylene on the catalyst performance could confirm whether ethylene increases coke formation and further whether coke formation, rather than sulfur poisoning, causes the significant changes in catalyst performance observed during the tests in Section 6.3.

Coke formation

- In Chapter 6 we proposed that coke may form as a result of surface ethylene concentrations which can form stable surface carbon species. However, this result was not confirmed (as discussed in the previous section). Future work could confirm that ethylene generates coke under these conditions and study the coke formation mechanism in more detail. For instance, the type of surface from which the ethylene or coke originates (for instance support vs. precious metal) could be identified. Therefore, future work could investigate which sites are associated with coke formation. With this understanding, the catalyst formulation could be optimized to reduce coking. Further, understanding where the coke originates may provide additional evidence for the relationship between coke and catalyst activity. For instance, data presented in Chapter 7 indicated that activity may be proportional to the amount of graphitic carbon on the surface.

Precious metal sintering

- In Chapter 9 it was shown that the CO chemisorption capacity of the Rh-Pt catalyst decreased with increasing calcination temperature. Decreases in CO chemisorption are typically assumed

to represent increases in particle size. Thus, the CO chemisorption result may mean that precious metal particles sinter during high temperature air treatment. In support of this theory, XRD patterns on catalysts after high temperature aging had sharp peaks assignable to precious metal species. TEM results could not be used to confirm this due to the difficulty of identifying and measuring precious metal particles in the presence of zirconia particles. Therefore, more advanced characterization methods such as EXAFS could be used to conclude whether the average precious metal particle size is larger on samples that have been regenerated after longer TOS.

Catalyst carrier

- XRD patterns and XPS abundance ratios provided preliminary evidence that zirconia may isolate and agglomerate into larger crystallites during steam reforming conditions. Further, XRD patterns revealed sharper tetragonal zirconia peaks on catalysts calcined at higher temperatures. There have been several studies that have reported the isolation and growth of zirconia particles from a SiO_2-ZrO_2 carrier during high temperature oxidative treatment [87]. However, no studies have been identified that

report this behavior during steam reforming conditions. Confirming whether this behavior occurs during steam reforming conditions and understanding what impact this behavior has on catalyst selectivity and metal dispersion is another interesting area for future research.

Bibliography

[1] Contributions of Working Group I to the Fourth Assessment report of the IPCC, Climate Change 2007 - The physical science basis, Cambridge University Press, 2007.

[2] "Comparison of fuel cell technologies" US Department of Energy: http://www1.eere.energy.gov/hydrogenandfuelcells/fuelcells/pdfs/fc_comparison_chart.pdf, 01 Feb 2013.

[3] A.E. Lutz, R.S. Larson, J.O. Keller, International Journal of Hydrogen Energy 27 (2002) 1103-1111.

[4] "Fuel Economy: Where the energy goes" US Department of Energy: http://www.fueleconomy.gov/feg/atv.shtml, 01 Feb 2013.

[5] " Greenhouse Gas Emissions from the U.S. Transportation Sector, 1990-2003" US Environmental Protection Agency Office of Transportation and Air Quality: http://www.epa.gov/oms/climate/420r06003.pdf, 01 Feb 2013.

[6] "Well-to-Wheels Case Studies for Hydrogen Pathways" US Department of Energy Hydrogen and Fuel Cells Program, http://www.hydrogen.energy.gov/well_wheels_analysis.html, 01 Feb 2013.

[7] Spendelow, Jacob, and Jason Marcinkoski. *"Fuel Cell System Cost - 2012."* Rep. DOE Fuel Cell Technologies Program, http://www.hydrogen.energy.gov/pdfs/12020_fuel_cell_system_cost_2012.pdf, 01 Feb 2013.

[8] R.J. Farrauto, C.H. Bartholomew, Fundamentals of industrial catalytic processes, 2nd ed., Wiley, Hoboken, N.J., 2006.

[9] Basic Research Needs for the Hydrogen Economy. Report of the Basic Energy Sciences Workshop on Hydrogen Production, Storage and Use, May 13-15, 2003, United States. Dept. of Energy. Office of Basic Energy Sciences, S.l., 2004.

[10] M. Wang, Journal of Power Sources 112 (2002) 307-321.

[11] R. Kwok, Nature 461 (2009) 582-583.

[12] G.W. Davis, Ethanol Vehicle Cold Start Improvement When Using a Hydrogen Supplemented E85 Fuel, Intersociety EnergyConversion Engineering Conference, 2000, pp. 303-308.

[13] C. Hulteberg, International Journal of Hydrogen Energy 37 (2012) 3978-3992.

[14] C.S. Song, Catalysis Today 77 (2002) 17-49.

[15] J.A. Francesconi, M.C. Mussati, R.O. Mato, P.A. Aguirre, Journal of Power Sources 167 (2007) 151-161.

[16] T. Ioannides, Journal of Power Sources 92 (2001) 17-25.

[17] P.R. de la Piscina, N. Homs, Chem Ind-Ser 112 (2006) 233-248.

[18] A.N. Fatsikostas, X.E. Verykios, Journal of Catalysis 225 (2004) 439-452.

[19] J.W.C. Liberatori, R.U. Ribeiro, D. Zanchet, F.B. Noronha, J.M.C. Bueno, Applied Catalysis A: General 327 (2007) 197-204.

[20] N. Laosiripojana, S. Assabumrungrat, Applied Catalysis B: Environmental 66 (2006) 29-39.

[21] P. Biswas, D. Kunzru, Chemical Engineering Journal 136 (2008) 41-49.

[22] V. Klouz, V. Fierro, P. Denton, H. Katz, J.P. Lisse, S. Bouvot-Mauduit, C. Mirodatos, Journal of Power Sources 105 (2002) 26-34.

[23] M.C. Sánchez-Sánchez, R.M. Navarro, J.L.G. Fierro, International Journal of Hydrogen Energy 32 (2007) 1462-1471.

[24] A.L. Alberton, M.M.V.M. Souza, M. Schmal, Catalysis Today 123 (2007) 257-264.

[25] A. Carrero, J.A. Calles, A.J. Vizcaíno, Chemical Engineering Journal 163 (2010) 395-402.

[26] D.K. Liguras, D.I. Kondarides, X.E. Verykios, Applied Catalysis B: Environmental 43 (2003) 345-354.

[27] H. Idriss, Platinum Metals Review 48 (2004) 105-115.

[28] T. Montini, L. De Rogatis, V. Gombac, P. Fornasiero, M. Graziani, Applied Catalysis B: Environmental 71 (2007) 125-134.

[29] P.Y. Sheng, W.W. Chiu, A. Yee, S.J. Morrison, H. Idriss, Catalysis Today 129 (2007) 313-321.

[30] J.P. Breen, R. Burch, H.M. Coleman, Applied Catalysis B: Environmental 39 (2002) 65-74.

[31] A. Yee, S.J. Morrison, H. Idriss, Catalysis Today 63 (2000) 327-335.

[32] J.J. Strohm, J. Zheng, C. Song, Journal of Catalysis 238 (2006) 309-320.

[33] E.C. Wanat, K. Venkataraman, L.D. Schmidt, Applied Catalysis A: General 276 (2004) 155-162.

[34] M. Ni, D.Y.C. Leung, M.K.H. Leung, International Journal of Hydrogen Energy 32 (2007) 3238-3247.

[35] R.K. Kaila, A. Gutiérrez, R. Slioor, M. Kemell, M. Leskelä, A.O.I. Krause, Applied Catalysis B: Environmental 84 (2008) 223-232.

[36] A. Erdőhelyi, J. Raskó, T. Kecskés, M. Tóth, M. Dömök, K. Baán, Catalysis Today 116 (2006) 367-376.

[37] A. Bshish, Z. Yaakob, B. Narayanan, R. Ramakrishnan, A. Ebshish, Chemical Papers 65 (2011) 251-266.

[38] R.M. Heck, R.J. Farrauto, S.T. Gulati, Catalytic air pollution control : commercial technology, 3rd ed., John Wiley, Hoboken, N.J., 2009.

[39] W.E. Giroux; Thomas, Farrauto; Robert Joseph Reforming sulfur-containing hydrocarbons using a sulfur resistant catalyst, BASF Corporation, USA, 2011.

[40] R. Farrauto, Y. Liu, W. Ruettinger, O. Ilinich, L. Shore, T. Giroux, Catalysis Reviews - Science and Engineering 49 (2007) 141-196.

[41] A. Simson, E. Waterman, R. Farrauto, M. Castaldi, Applied Catalysis B: Environmental 89 (2009) 58-64.

[42] J. Sun, X.-P. Qiu, F. Wu, W.-T. Zhu, International Journal of Hydrogen Energy 30 (2005) 437-445.

[43] P.D. Vaidya, A.E. Rodrigues, Industrial and Engineering Chemistry Research 45 (2006) 6614-6618.

[44] L.E. Arteaga, L.M. Peralta, V. Kafarov, Y. Casas, E. Gonzales, Chemical Engineering Journal 136 (2008) 256-266.

[45] A. Akande, A. Aboudheir, R. Idem, A. Dalai, International Journal of Hydrogen Energy 31 (2006) 1707-1715.

[46] P.V. Mathure, S. Ganguly, A.V. Patwardhan, R.K. Saha, Industrial and Engineering Chemistry Research 46 (2007) 8471-8479.

[47] R. Trane, S. Dahl, M.S. Skjøth-Rasmussen, A.D. Jensen, International Journal of Hydrogen Energy 37 (2012) 6447-6472.

[48] F. Soyal-Baltacıoğlu, A.E. Aksoylu, Z.I. Önsan, Catalysis Today 138 (2008) 183-186.

[49] H.S. Roh, Y. Wang, D.L. King, A. Platon, Y.H. Chin, Catalysis Letters 108 (2006) 15-19.

[50] A. Birot, F. Epron, C. Descorme, D. Duprez, Applied Catalysis B: Environmental 79 (2008) 17-25.

[51] S. Cavallaro, Energy and Fuels 14 (2000) 1195-1199.

[52] N. Bion, D. Duprez, F. Epron, ChemSusChem 5 (2012) 76-84.

[53] J.M. Guil, N. Homs, J. Llorca, P.R. de la Piscina, J Phys Chem B 109 (2005) 10813-10819.

[54] J.R. Rostrup-Nielsen, T.S. Christensen, I. Dybkjaer, in: T.S.R.P. Rao, G.M. Dhar (Eds.), Studies in Surface Science and Catalysis, Elsevier, 1998, pp. 81-95.

[55] A. Platon, H.S. Roh, D.L. King, Y. Wang, Top Catal 46 (2007) 374-379.

[56] N. Palmeri, S. Cavallaro, V. Chiodo, S. Freni, F. Frusteri, J.C.J. Bart, International Journal of Hydrogen Energy 32 (2007) 3335-3342.

[57] A. Le Valant, F. Can, N. Bion, D. Duprez, F. Epron, International Journal of Hydrogen Energy 35 (2010) 5015-5020.

[58] A. Le Valant, A. Garron, N. Bion, F. Epron, D. Duprez, Catalysis Today 138 (2008) 169-174.

[59] T. Yamazaki, N. Kikuchi, M. Katoh, T. Hirose, H. Saito, T. Yoshikawa, M. Wada, Applied Catalysis B: Environmental 99 (2010) 81-88.

[60] C.H. Bartholomew, Applied Catalysis A: General 212 (2001) 17-60.

[61] C.H. Bartholomew, P.K. Agrawal, J.R. Katzer, in: H.P. D.D. Eley, B.W. Paul (Eds.), Advances in Catalysis, Academic Press, 1982, pp. 135-242.

[62] S.L. Swartz, P.H. Matter, G.B. Arkenberg, F.H. Holcomb, N.M. Josefik, Journal of Power Sources 188 (2009) 515-520.

[63] A. Simson, R. Farrauto, M. Castaldi, Applied Catalysis B: Environmental 106 (2011) 295-303.

[64] S.L. Lakhapatri, M.A. Abraham, Applied Catalysis A: General 364 (2009) 113-121.

[65] C. Xie, Y. Chen, Y. Li, X. Wang, C. Song, Applied Catalysis A: General 390 (2010) 210-218.

[66] S. Rabe, F. Vogel, T.-B. Truong, T. Shimazu, T. Wakasugi, H. Aoki, H. Sobukawa, International Journal of Hydrogen Energy 34 (2009) 8023-8033.

[67] L. Wang, K. Murata, M. Inaba, Applied Catalysis B: Environmental 48 (2004) 243-248.

[68] A. Qi, S. Wang, C. Ni, D. Wu, International Journal of Hydrogen Energy 32 (2007) 981-991.

[69] G. Delahay, D. Duprez, Applied Catalysis 53 (1989) 95-105.

[70] Y. Chen, C. Xie, Y. Li, C. Song, T.B. Bolin, Physical Chemistry Chemical Physics 12 (2010) 5707-5711.

[71] C. Xie, Y. Chen, M.H. Engelhard, C. Song, ACS Catalysis 2 (2012) 1127-1137.

[72] P.K. Cheekatamarla, A.M. Lane, Journal of Power Sources 154 (2006) 223-231.

[73] A.C. Lausche, J.A. Schaidle, L.T. Thompson, Applied Catalysis A: General 401 (2011) 29-36.

[74] M. Ferrandon, J. Mawdsley, T. Krause, Applied Catalysis A: General 342 (2008) 69-77.

[75] P.K. Cheekatamarla, A.M. Lane, Journal of Power Sources 152 (2005) 256-263.

[76] E. Xue, M. O'Keeffe, J.R.H. Ross, in: F.V.M.S.M. Avelino Corma, G.F. José Luis (Eds.), Studies in Surface Science and Catalysis, Elsevier, 2000, pp. 3813-3818.

[77] J.R. Rostrup-Nielsen, Journal of Catalysis 21 (1971) 171-178.

[78] X. Karatzas, K. Jansson, A. González, J. Dawody, L.J. Pettersson, Applied Catalysis B: Environmental 106 (2011) 476-487.

[79] R. Burch, P.K. Loader, Applied Catalysis A: General 143 (1996) 317-335.

[80] D.L. Trimm, Catalysis Today 37 (1997) 233-238.

[81] E.B. Pereira, N. Homs, S. Martí, J.L.G. Fierro, P. Ramírez de la Piscina, Journal of Catalysis 257 (2008) 206-214.

[82] E.C. Wanat, K. Venkataraman, L.D. Schmidt, Applied Catalysis A: General 276 (2004) 155-162.

[83] J.H. Bitter, K. Seshan, J.A. Lercher, Journal of Catalysis 183 (1999) 336-343.

[84] D.L. Trimm, Applied Catalysis A: General 212 (2001) 153-160.

[85] M. Deeba, R.J. Farrauto, Y.K. Lui, Applied Catalysis A: General 124 (1995) 339-344.

[86] D.H. Aguilar, L.C. Torres-Gonzalez, L.M. Torres-Martinez, T. Lopez, P. Quintana, Journal of Solid State Chemistry 158 (2001) 349-357.

[87] G.K. Reddy, S. Loridant, A. Takahashi, P. Delichère, B.M. Reddy, Applied Catalysis A: General 389 (2010) 92-100.

[88] A.C.Q.M. Meijers, A.M. de Jong, L.M.P. van Gruijthuijsen, J.W. Niemantsverdriet*, Applied Catalysis 70 (1991) 53-71.

[89] R.G. Rodríguez Avendaño, J.A. De Los Reyes, T. Viveros, J.A. Montoya De La Fuente, Catalysis Today 148 (2009) 12-18.

[90] R. Hughes, Deactivation of catalysts, Academic, London ; Orlando, 1984.

[91] S.A. Hassan, F.H. Khalil, F.G. Elgamal, Journal of Catalysis 44 (1976) 5-14.

[92] S. Cavallaro, V. Chiodo, S. Freni, N. Mondello, F. Frusteri, Appl Catal a-Gen 249 (2003) 119-128.

[93] M. Ferrandon, T. Krause, Applied Catalysis A: General 311 (2006) 135-145.

[94] T. Wang, L.D. Schmidt, Journal of Catalysis 70 (1981) 187-197.

[95] H. Birgersson, M. Boutonnet, S. Järås, L. Eriksson, Top Catal 30-31 (2004) 433-438.

[96] S.J. Tauster, Accounts of Chemical Research 20 (1987) 389-394.

[97] R. Polvinen, M. Vippola, M. Valden, T. Lepistö, A. Suopanki, M. Härkönen, Journal of Catalysis 226 (2004) 372-381.

[98] S. Bernal, J.J. Calvino, M.A. Cauqui, J.M. Gatica, C. Larese, J.A. Pérez Omil, J.M. Pintado, Catalysis Today 50 (1999) 175-206.

[99] S.-i. Ito, K. Tomishige, Catalysis Communications 12 (2010) 157-160.

[100] Y. Men, M. Yang, Catalysis Communications 22 (2012) 68-73.

[101] U. Hennings, R. Reimert, Applied Catalysis A: General 337 (2008) 1-9.

[102] A. Maubert, G.A. Martin, H. Praliaud, P. Turlier, Reaction Kinetics and Catalysis Letters 24 (1984) 183-186.

[103] S. Bernal, F.J. Botana, J.J. Calvino, C. López, J.A. Pérez-Omil, J.M. Rodríguez-Izquierdo, Journal of the Chemical Society - Faraday Transactions 92 (1996) 2799-2809.

[104] A.D. Logan, E.J. Braunschweig, A.K. Datye, D.J. Smith, Langmuir 4 (1988) 827-830.

[105] E.J. Braunschweig, A.D. Logan, A.K. Datye, D.J. Smith, Journal of Catalysis 118 (1989) 227-237.

[106] R.J. Fenoglio, G.M. Nuñez, D.E. Resasco, Journal of Catalysis 121 (1990) 77-88.

[107] C. Binet, A. Jadi, J. Lavalley, M. Boutonnet-Kizling, Journal of the Chemical Society, Faraday Transactions 88 (1992) 2079-2084.

[108] A. Gutierrez, R. Karinen, S. Airaksinen, R. Kaila, A.O.I. Krause, International Journal of Hydrogen Energy 36 (2011) 8967-8977.

[109] D.L. Hoang, H. Lieske, Catalysis Letters 27 (1994) 33-42.

[110] C. Yin, D. Xia, Fuel 83 (2004) 433-441.

[111] J.H. Scofield, Journal of Electron Spectroscopy and Related Phenomena 8 (1976) 129-137.

[112] Z. Dang, B.G. Anderson, Y. Amenomiya, B.A. Morrow, The Journal of Physical Chemistry 99 (1995) 14437-14443.

[113] B. McMahon, Power 150 (2006) 36-+.

[114] S.M. Hashemnejad, M. Parvari, Chinese Journal of Catalysis 32 (2011) 273-279.

[115] N.M. Rodriguez, Journal of Materials Research 8 (1993) 3233-3250.

[116] J. Boon, E. van Dijk, S. de Munck, R. van den Brink, Journal of Power Sources 196 (2011) 5928-5935.

[117] J. Sehested, J.A.P. Gelten, S. Helveg, Applied Catalysis A: General 309 (2006) 237-246.

[118] Y. Lu, J. Chen, Y. Liu, Q. Xue, M. He, Journal of Catalysis 254 (2008) 39-48.

[119] C. Xie, Y.S. Chen, Y. Li, X.X. Wang, C.S. Song, Appl Catal a-Gen 390 (2010) 210-218.

[120] S.K. Goud, W.A. Whittenberger, S. Chattopadhyay, M.A. Abraham, International Journal of Hydrogen Energy 32 (2007) 2868-2874.

[121] J. Robertson, Materials Science and Engineering: R: Reports 37 (2002) 129-281.

[122] B. Guichard, M. Roy-Auberger, E. Devers, B. Rebours, A.A. Quoineaud, M. Digne, Applied Catalysis A: General 367 (2009) 1-8.

[123] F. Tuinstra, J.L. Koenig, The Journal of Chemical Physics 53 (1970) 1126-1130.

[124] D. Espinat, H. Dexpert, E. Freund, G. Martino, M. Couzi, P. Lespade, F. Cruege, Applied Catalysis 16 (1985) 343-354.

[125] P. Albers, K. Deller, B.M. Despeyroux, A. Schäfer, K. Seibold, Journal of Catalysis 133 (1992) 467-478.

[126] C. Li, T.C. Brown, Carbon 39 (2001) 725-732.

[127] A. Karelovic, X. García, R. Wojcieszak, P. Ruiz, A.L. Gordon, Applied Catalysis A: General 384 (2010) 220-229.

[128] M.J.C. Guittet, J. P.; Gautier-Soyer, M., Physical Review B 63 (2001).

[129] H.P.C.E. Kuipers, H.C.E. Vanleuven, W.M. Visser, Surf Interface Anal 8 (1986) 235-242.

[130] Y.A. Ryndin*, O.S. Alekseev, E.A. Paukshtis, A.V. Kalinkin, D.I. Kochubey, Applied Catalysis 63 (1990) 51-65.

[131] W. Weng, C. Luo, J. Huang, Y. Liao, H. Wan, Top Catal 22 (2003) 87-93.

[132] H.C. Yao, S. Japar, M. Shelef, Journal of Catalysis 50 (1977) 407-418.

[133] P. Samoila, M. Boutzeloit, C. Especel, F. Epron, P. Marécot, Journal of Catalysis 276 (2010) 237-248.

[134] D. Martin, D. Duprez, Applied Catalysis A: General 131 (1995) 297-307.

Appendices

Appendix A: Experimental

Appendix A.1. Sulfur compounds in E85

The sulfur compounds were analyzed by Empact analytical according to ASTM D5504-94. The following compounds were the most abundant sulfur species in the fuel. The total sulfur (mg/L) in the commercial grade E85 was found to be 28 ppm and 5 ppm in the synthetic E85.

Table A.1.10.1: Most abundant sulfur species in fuel

Sulfur compound	ppm (mg/L)
Thiophene	5.36
Methyldibenzothiophene	2.86
Trimethylbenzothiophene	1.77
n-Propanethiol	0.76
diethyldisulfide	0.67

Appendix B: Additional studies and calculations

B.1: Kinetics of ESR on a Rh/Pt washcoated monolith

As a baseline for an overall process, a global rate expression for the steam reforming of ethanol using the Rh-Pt/SiO_2-ZrO_2 catalyst was developed. A range of residence times and initial concentrations were tested. An Arrhenius rate expression was developed for ethanol reforming with the washcoated monolith of the form:

$$r = \frac{d[C_{EtOH}]}{dt} = -k \cdot [C_{EtOH}]^{\alpha} \cdot [C_{H2O}]^{\beta} \quad \text{(B.1.1)}$$

where α and ß represent the reaction orders for ethanol and water and k represents the rate coefficient. The k values are functions of temperature and are related to the activation energy for a specific reaction according to:

$$k = k_o \cdot e^{\frac{-E_a}{R \cdot T}} \quad (B.1.2)$$

where k_o indicates the pre-exponential function, E_a represents the activation energy and T represents bed temperature.

B.1.1 Calculation of reaction orders

To calculate a reaction order with respect to ethanol, the concentration of ethanol was varied while maintaining constant water concentration at isothermal conditions.

A modified version of equation B.1 was used to determine reaction orders for ethanol and water:

$$lnr = K + \alpha \cdot ln[C_{EtOH}] \quad (B.1.3)$$

where K represents a combination of constants: the natural log of the activation energy term, *k*, and the natural log of the water concentration. According to equation B.1.3, the natural log of ethanol consumption rates was plotted as a function of the natural log of the initial ethanol concentrations and the slope yielded the reaction order (α) for ethanol. The reaction rates for ethanol disappearance and acetaldehyde formation as a function of ethanol partial pressure are shown in Figure B.1.1.

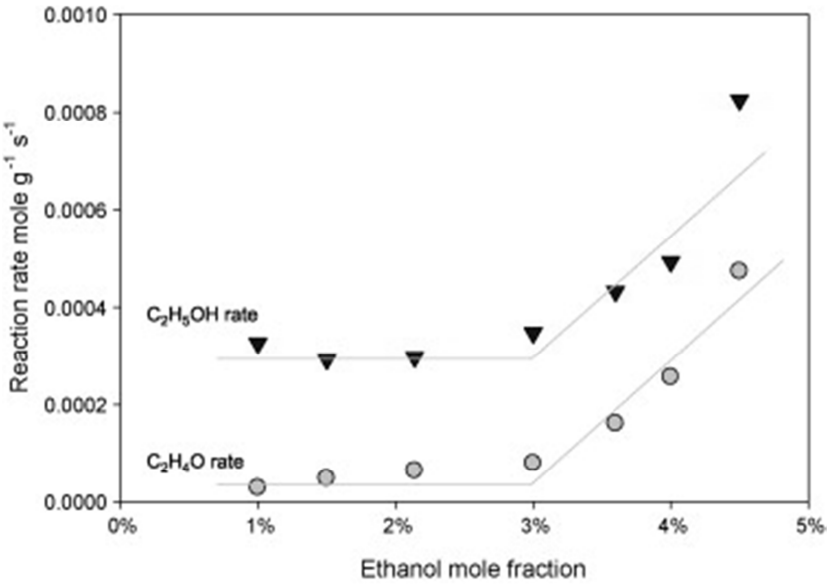

Fig. B.1.1 Effect of ethanol concentration on production/consumption rates for GHSV = 100,000 h^{-1}, washcoat loading = 0.5 g/in^3, for ethanol (▼) and acetaldehyde (●).

The results depicted in Figure B.1.1 show that two regimes existed within the range tested, a response at low ethanol molar fractions (or high

water/ethanol ratios) and another at high ethanol molar fractions (or low water/ethanol ratios near stoichiometric). For the region with ethanol concentrations of 1-3% (water/ethanol ratios of 4:1-6:1) a reaction order of 1.2 was calculated. For the region with ethanol concentration between 3-5% (water/ethanol ratios of 6:1-10:1) a reaction order of 0.25 for ethanol was calculated.

In order to calculate a reaction order for water, water concentration was varied from 9-18% of total feed (water/ethanol ratios of 3:1-7:1) keeping ethanol constant at 3% of the total feed. At the lowest concentrations of water, changes in water concentration had minimal effect on the rate of ethanol disappearance and the reaction was determined to be zero order; however a more significant negative dependence was found at higher water concentrations (-0.25).

B.1.2. Calculation of activation energy

Utilizing the reaction orders calculated in the previous section for low water/ethanol ratios, the Arrhenius expression (B.1.1) can be rewritten:

$$k = k_o \cdot e^{\frac{-E_a}{R \cdot T}} \cdot [C_{EtOH}]^{1.2} \quad (B.1.4)$$

Unlike typical kinetic studies which maintain conversion of the reactants to less than 5% and limit temperature changes across the bed to less than 10°C, here the monolith was operated near adiabatic, thus differences in the measured inlet and outlet monolith temperature were observed. Therefore

the value of k in Equation B.1.1 is not independent of temperature. By assuming a linear profile between inlet and outlet temperature measurements the following modified Arrhenius expression was utilized:

$$\int \frac{d[C_{EtOH}]}{[C_{EtOH}]^{1.2}} = -k_o \cdot \int e^{\frac{-E_a}{R(a+bT)}} dt \quad (B.1.5)$$

The pre-exponential factor k_o and the apparent activation energy E_a were not considered functions of temperature. The resulting expression was integrated numerically for a series of conditions with variable conversions, residence times and temperature profiles.

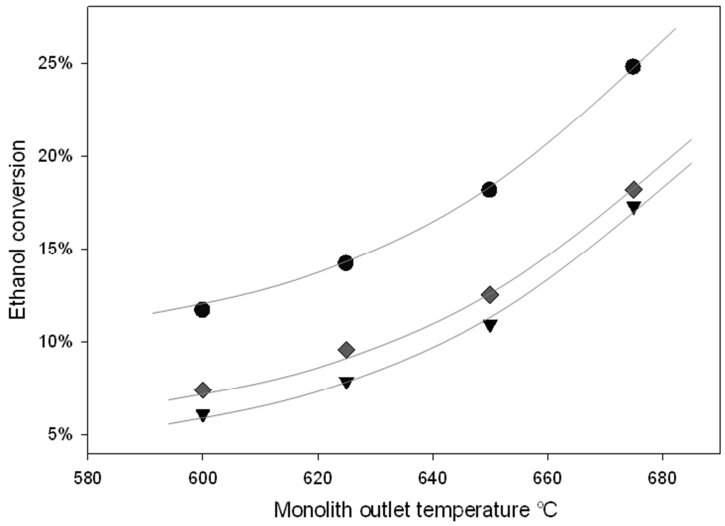

Figure B.2.2: Ethanol conversion values for washcoat loadings of 0.5 g/in^3, 1.5 S/C (stoichiometric) with GHSV = 50 000 h^{-1} (●), GHSV = 75 000 h^{-1}(◆), GHSV = 100 000 h^{-1} (▼).

For each condition a 1.5 S/C ratio (stoichiometric) was utilized with a catalyst loading of 0.5 g/in^3. Using the conjugate gradient method equation B.1.5 was evaluated for each of the different data points given in Figure B.2.2

and the overall activation energy was found to be 85.24 kJ mole^{-1} with the following pre-exponential constant:

$$k = 2.21 \cdot 10^5 \cdot mol^{-0.2} \cdot m^{0.6} \cdot s^{-1}$$

B.2 Sulfur analysis during TPO

An initial assumption was made that catalysts that had reformed the sulfur containing fuel would have significant levels of sulfur on the surface. TPO of spent catalysts was identified as a method to measure total sulfur on spent catalysts. During the ex-situ oxidation tests, carbon is oxidized to CO_2 and sulfur is oxidized to SO_2. Thus, gas analysis of the TPO effluent was performed with mass spectrometry (MS), which is capable of measuring SO_2. By integrating SO_2 concentrations over the test runtime the total sulfur could be quantified.

The TPO tests were performed with TGA with a heating ramp of 5°C/min in 3% O_2/N_2 with a total flowrate of 100 mL/min. The products of the TPO test were analyzed with MS scanning for CO_2 and SO_2 molecules. Thus, mass changes, energy changes (by DTA) and gas analysis was collected. Prior to testing, the SO_2 detection limit of the TGA/MS system was determined. The signal to noise level of the MS was measured at a series of SO_2 concentrations in a 1 µL sample. The results of these tests are shown in the table below.

Table B.10.2.1: Signal to noise levels for associated SO_2 concentrations

Sulfur amount (kg)	Signal to noise
374 ng	17
3.74 ng	7
0.374	ND[1]

1. ND = not detectable

In order to correlate gas phase SO_2 concentrations with sulfur concentrations on the catalyst surface a number of assumptions had to be made. First, it was assumed that sulfur would be oxidized within the residence time of the TGA (V/Q). The sample size for the TGA was 100 mg catalyst and the chemisorption from the fresh catalyst (32%) was used to determine total precious metal sites. Based on these assumptions the following concentrations of SO_2 (for a 1 µL sample) were calculated associated S:PM ratios:

Table B.2.2: Expected SO_2 concentrations for associated chemisorbed sulfur

Sulfur adsorption (S:PM ratio)	Sulfur expected in MS sample
1:1	50 ng
1:100	0.5 ng

Based on the results of these tests it was assumed that S:PM concentrations below 1:100 would not be detectable by TPO with MS analysis. For the catalyst that had been on stream for 105-hrs (Figure 4.5) the sulfur concentrations were not measureable with this test rig and were later confirmed to be in the range of 1:100 S:PM by ICP analysis.

B.3 Analysis of pressure drop through a packed bed

Packed beds frequently suffer from high pressure drops compared to monolith beds. However, a packed bed was desired for a series of tests to facilitate easier ex-situ characterization of the catalyst. The pressure drop is significantly dependent on particle size. Larger particles lead to lower pressure drop at the expense of increased diffusion limitations. Thus, in order to determine an appropriate particle size for the packed bed, the pressure drop was calculated as a function of particle size. In addition, mass and heat transfer rates through the particle boundary layer and within the catalyst pores were calculated as a function of particle size. These rates were compared to kinetic rates calculated according to the parameters developed in Appendix B.1. Based on these calculations an appropriate particle size was chosen that allowed for a low pressure drop without sacrificing significant increases in heat or bulk mass transfer rates.

B.3.1. Calculation of kinetic rate

The rate was calculated based on the Arrhenius expression developed in Appendix B.1. It was assumed that the kinetic rate would not vary significantly for the monolith and packed bed. The initial concentrations that were used depended on the test conditions. In order to determine whether the conditions would lead to a kinetically or BMT controlled reaction the kinetic

rate constant k (equation B.1.1) was compared to the mass transfer rate constant k_c.

B.3.2. Calculation of mass transfer rate through a packed bed

In a BMT controlled reaction the rate is dictated by the diffusion of reactants or products through the particle boundary layer. To calculate the mass transfer rate, the reaction coefficient (for a mass transfer limited reaction) k_c was calculated according to the following equation:

$$r = -k_c \cdot \left[C_{i,g}\right] \quad (B.3.1)$$

In equation B.3.1, the variable $[C_{i,g}]$ is the concentration of the limiting reactant, i, in the bulk. For a mass transfer limited reaction it is assumed that the concentration of the limiting reactant at the surface is 0. It is assumed that the limiting reactant is ethanol. The reaction coefficient k_c is a function of the diffusivity of ethanol through a stagnant gas at the reaction conditions as well as the geometry of the boundary layer. The following expression is used to calculate k_c:

$$k_c = \frac{D_{EtOH}}{D_p} \cdot Sh \quad (B.3.2)$$

In the equation above Sh represents the Sherwood number, D_p is the diameter of the particle, D_{EtOH} represents the diffusivity of ethanol through the boundary layer. The diffusivity of ethanol though nitrogen at 650°C

(973K) was used as an approximation for this value and calculated according to the following expression:

$$D_{EtOH} = \frac{.001858 \cdot T^{\frac{3}{2}} \cdot \left[\frac{1}{M_A} + \frac{1}{M_B}\right]}{P \cdot \sigma_{AB} \cdot \Omega_D} \quad (B.3.3)$$

In the above equation M_A and M_B are the molecular weights of ethanol and nitrogen respectively, P is the pressure (atmospheric), and the collision diameter was calculated according to the average of the diameter of the individual species. The collision integral Ω_D was determined from tables by correlating it with the value of kT/ϵ_{AB} where ϵ_{AB} is the energy of molecular interaction calculated based on the following equations and parameters:

$$\epsilon_{AB} = \sqrt{\epsilon_A \cdot \epsilon_B} \quad (B.3.4)$$

$$\sigma_{AB} = \frac{\sigma_A + \sigma_B}{2} \quad (B.3.5)$$

Ethanol	ϵ_A/k	91.5	K
	σ_A	4.455	angstrom
Nitrogen	ϵ_B/k	391	K
	σ_B	3.681	angstrom

In order to complete the calculation for k_c, the Sherwood number must be calculated. The Sherwood number is a dimensionless number which is a function of the geometry of the catalyst, and the dimensionless Reynolds and Schmidt numbers. Thus, for spherical particles the Frossling correlation can be utilized:

$$Sh = 2 + 0.6 \cdot Re^{0.5} \cdot Sc^{0.3} \quad \text{(B.3.6)}$$

The Reynolds number was calculated according to the following definition:

$$Re = \frac{U \cdot D_p \cdot \rho}{\mu} \quad (B.3.7)$$

In equation B.3.7, the variable U is the average velocity in the bulk, D_p is the particle diameter, ρ is the density of the gas (calculated assuming 20% steam in nitrogen), and μ is the gas viscosity. The Reynolds numbers calculated for the range of conditions studied were in the range of 1-100, thus, the flow was laminar. The Schmidt number was calculated according to the following expression:

$$Sc = \frac{\upsilon}{D_{EtOH}} \quad \text{(B.3.8)}$$

where υ is the viscosity of the gas. From these numbers the Sherwood number was calculated and the bulk mass transfer rates could be calculated as a function of D_p.

B.3.3. Internal mass diffusion analysis

In order to calculate the influence particle size and bed type on pore diffusion limitations the Thiele modulus and Weisz-Prater criterion were calculated for each condition. The Thiele modulus is a ratio of the surface reaction rate to the rate of diffusion in the catalyst pores. The Weisz-Prater criterion is a function of the Theile modulus and is a dimensionless number

which determines whether pore diffusion effects can be ignored. The criterion is calculated as follows:

$$C = \frac{r_{obs} {L_c}^2}{C_{EtOH} \cdot D_{eff}} \quad (B.3.9)$$

The pore length, L_c, is conservatively assumed to be the radius of the pellet. A separate diffusivity of the gases through the pores, D_{eff}, the effective diffusivity was calculated according to the equation below.

$$D_{eff} = \frac{\varepsilon_p \cdot d_p}{\tau_k \cdot 3} \cdot \sqrt{\frac{8 \cdot R \cdot T}{\pi \cdot M}} \quad (B.3.10)$$

The values used were a porosity, ε_p, of 0.3, a tortuosity τ_k of 0.15 and a pore diameter of 8 nm. For the washcoats utilized the criterion is on the order of 10^{-5} and thus is not considered. For a particle size of 600 μm the value was 0.1. Thus, this particle size was the boundary for considerations of pore diffusion and larger particle were not desired in order to limit internal diffusion limitations.

B.3.4 Heat transfer analysis during reforming conditions

Heat transfer through both the particle boundary layer and the internal catalyst pore were compared to kinetic rates. The Mears criterion was used to estimate the influence of the particle size on the heat transfer limitations. The following expression was used to calculate the criterion:

$$\frac{-\Delta H \cdot r \cdot L_c \cdot E_a}{\alpha \cdot T^2 \cdot R} \quad (B.3.11)$$

The heat transfer coefficient, α is calculated according to the Nusselt number, Nu and the heat conductivity of the gas λ_g:

$$\alpha = \frac{Nu \cdot \lambda_g}{D_p} \quad (B.3.12)$$

The conductivity of the gas that was calculated was 480 kg/K-s^3. The criterion was on the order of 10^{-3}, thus, significant differences in temperature across the boundary layer were assumed to be negligible during the endothermic steam reforming reaction.

B.3.5. Pressure drop calculations

The pressure drop was calculated as a function of D_p using the following expression (a variation of the Ergun equation) for pressure drop through a packed bed:

$$p = L \cdot f_p \cdot \frac{\rho \cdot U^2}{D_p} \cdot \left(\frac{1 - \varepsilon_p}{{\varepsilon_p}^3} \right) \quad (B.3.13)$$

In equation B.3.13, L is the length of the bed, ε is the porosity, f_p is a friction factor defined as:

$$f_p = \frac{150}{Re} + 1.75 \quad (B.3.14)$$

(the coefficient of 150 and 1.75 are a good approximation for our geometry).

B.2.6. Analysis

In order to ensure a low pressure drop and approximate isobaric conditions a particle size was chosen that allowed for a low pressure drop and

had a high BMT rate (relative to the kinetic rate). The table below illustrates how particle size impacts both pressure drop and BMT in a packed bed. Based on the results, a particle size of 600 um was chosen in order to minimize heat and mass diffusion and limitations and have a low pressure drop in the bed.

Table B.3.1: Pressure drop in packed beds with different sized particles

Particle diameter μm	Pressure drop, psi	k_c/k_r
10	10.7	8646
100	1.1	929
600	0.179	256
1000	0.1	113

B.4 Estimation of surface temperature during regeneration

During regenerations coke is burned off the surface. The oxidation of these carbon species is a highly exothermic process that can generate high surface temperatures on the catalyst surface. A series of calculations were performed to correlate the extent of coke formation on the catalyst with an approximate surface temperature during air regeneration. An energy balance was performed at the gas-solid interface that assumed that some fraction of the thermal energy was distributed to the solid χ and another fraction was transported to the gas phase (1-χ). In order to simplify the calculations convective heat transfer was ignored and the gas was assumed to be stagnant.

The following expression was used to determine the increase in surface temperature, ΔT_s, which would occur due to the exothermic oxidation reaction:

$$\Delta T_s = \frac{\chi \cdot n_i \cdot \Delta H_r}{n_t \cdot C_p} \qquad (B.4.1)$$

In the numerator of equation B.4.1, n_i represents the total number of moles carbon, ΔH_r represents the heat of reaction and χ represents the fractional heat transfer to the solid phase. The heat of reaction was assumed to be -393 kJ/mol, which is the enthalpy for the full oxidation of graphite to CO_2. In the denominator of equation B.4.1, n_t represents the number of moles

in the solid phase (including catalyst diluent) and C_p represents the heat capacity of the solid. The heat capacity used for $ZrSiO_4$ was 133 J/mol-K (from tables).

In order to approximate χ, the distribution of thermal energy transferred across the gas solid interface, the thermal conductivities of the solid and gas were compared. The thermal conductivity of the gas phase was calculated according to the kinetic theory of gases assuming 100% N_2:

$$k = \frac{1}{\pi^{\frac{3}{2}} \cdot d^2} \cdot \sqrt{\kappa^3 \cdot \frac{T}{m}} \qquad (B.4.2)$$

In the equation above, d is the diameter of a nitrogen molecule, T is 923K and m is the mass of a nitrogen molecule. The thermal conductivity of the gas was 0.082 W/m-K. The thermal conductivity of the solid was assumed to be 0.5 W/m-K, a common value for porous catalysts. The assumption was to ignore conductive effects and assume a stagnant gas phase above the catalyst. Thus, the ratio of thermal conductivities was on the order of 6:1. Thus, 85% of the heat was assumed to be transferred to the solid material.

In Chapter 7 catalysts that had been exposed to different TOS were subjected to ex-situ TPO which determined the amount of total surface carbon. Equation B.4.2 was evaluated with the results from the TPO tests (mole carbon) to predict the surface temperatures during regenerations performed after different TOS. As shown in Table B.4.1, a catalyst that had

performed E85 steam reforming for 12-hrs (in the conditions discussed in Section 7.1) would be subjected to increases of up to 346°C during the regeneration condition (surface temperatures up to approximately 1000°C)

Table B.4.1: Expected temperature increases measured on the catalyst surface during regenerations performed after varying TOS (calculated from TPO results shown in Chapter 7)

TOS	wt% C	ΔT (°C)
2	1.7%	52
4	2.9%	88
9	3.7%	116
12	11.5%	346

B.5. Determining dispersion and particle size from CO chemisorption

Metal dispersion can be calculated from total chemisorption capacity by assuming a stoichiometry between the adsorbent molecule and the active metal. In this case, we assume that the adsorbent molecule, CO, chemically adsorbs on precious metal sites with a 1:1 stoichiometry. By measured the volume of CO uptake (calibrated for with syringe injections of CO) the number of moles of accessible precious metal is calculated. The number of moles was calculated using a weight average of the molecular weights of platinum and rhodium.

The total surface area of the metal is calculated according to the following equation:

$$A = n_{CO} \cdot SA_{PM} \cdot S \quad (B.5.1)$$

where n_{CO} is the moles of CO adsorbed, SA_{PM} is the weighted average of the surface area of the precious metal species, and S is the stoichiometry of adsorption (assumed to be 1).

The corresponding particle size (mean particle diameter) was calculated according to equation B.5.2 where D_{PM} is the weighted average of the metal density (gram per metal volume – we used 14.6 g/mL) and A_m is the metal surface area (square meters per gram metal).

$$D_{PM} = \frac{L \cdot f}{g_{cat} \cdot A_m \cdot \rho_m} \quad (B.5.2)$$

The primary assumptions are the stoichiometry of adsorption, *S*, and the shape factor, which is a surface to volume ratio for the solid crystallites. Here, we use a shape factor of 6, representative of spherical particles. The calculated particle sizes for a set of dispersions (discussed in 9.2.1) are given in Table B.5.1.

Table B.5.1: Calculated dispersion and particle size for catalyst after high temperature calcination in air

Calcined catalyst	Dispersion	Calculated particle size (nm)
650°C 1-hr	19.2%	2.8
750°C 1-hr	12.6%	4.2
850°C 1-hr	5.0%	10.6

Appendix C: Additional data

C.1.Deactivation during ESR

During ESR both activity and selectivity changes were measured. In order to understand the changes in selectivity, the selectivity for individual product species was calculated and the change in the selectivities of each species were studied as a function of TOS. Molar flow rates of each species (N_i) were calculated (using nitrogen as an internal standard) and the production rates of each individual species r_i were calculated according to the following equation:

$$r_i = \frac{d(N_i)}{W} \quad (C.1.1)$$

The catalyst selectivity towards individual species was calculated according to:

$$S_i = \frac{N_{i,out} - N_{i,in}}{N_{ethanol,out} - N_{ethanol,in}} \quad (C.1.2)$$

The changes in selectivity of each species as a function of TOS were calculated in addition to the traditional deactivation rate which is a function of only activity:

$$r_{d,i} = \frac{d(S_i)}{dt} \quad (C.1.3)$$

The following plot shows the changes in catalyst selectivity during a 19-hr ethanol steam reforming test (details in Section 4.1).

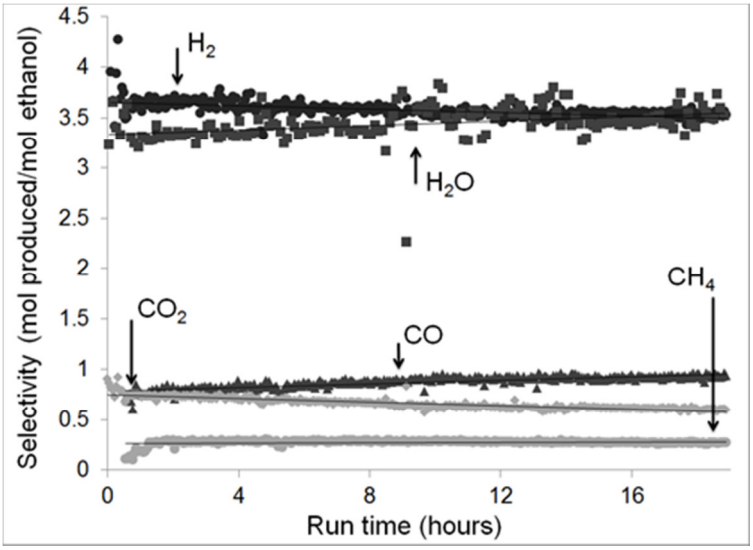

Figure C.1.1: Selectivities for major product species measured during ESR with S/C = 1.6, washcoat loading = 0.5 g/in^3 and GHSV = 44,000h^{-1}

The changes in selectivity were quantified and the result are shown in Table C.1.1. Significant changes in selectivity towards methane were not measured with TOS. The selectivity for CO and H_2O increased at approximately the same rate at which H_2 and CO_2 rates decreased. This was consistent with a change in WGS activity (equation 5).

Table C.1.1: Changes in selectivity measuring during the test in Figure C.1.1.

Species	Selectivity change (mol/hr)	
H2	-	8.10E-03
H2O	+	1.10E-02
CO2	-	9.10E-03
CO	+	9.00E-03
CH4	+	8.20E-04
C2H4	+	3.00E-04
C2H4O	+	2.60E-04

C.2. Additional regeneration studies

In Chapter 5 the impact of regenerations on subsequent catalyst performance is studied. In addition to the conditions shown in Chapter 5, regenerations were also performed after deactivation measured at high GHSV. At these conditions the irreversible deactivation discussed in Chapter 5 was also identified with both a sulfur-free and sulfur-containing fuel. The results with the sulfur-free fuel are shown in Section 6.6. The conditions in the test below were: washcoat loading = 0.5 g/in^3 and GHSV = 44,000 h^{-1}. As shown, after regenerations the hydrogen production and conversion decreased more rapidly than in the first reforming cycle. Thus, the irreversible deactivation discussed in Chapter 5 was also measured at these conditions.

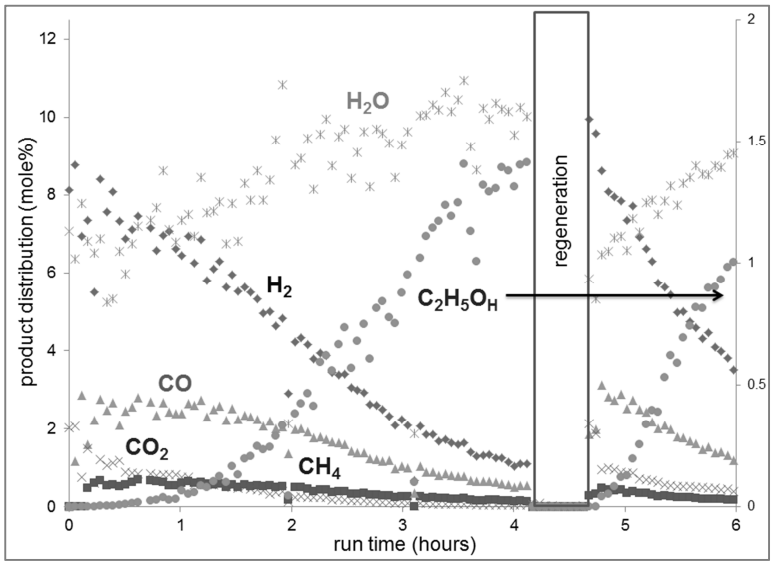

Figure C.2.1: Reforming 28 ppm sulfur E85 with steam/carbon = 1.8, washcoat loading = 0.5 g/in^3 and GHSV = 22,000 h^{-1}, with air regeneration = 50% air, 50% N_2

Appendix D: XRD analysis

Peak positions in X-ray diffraction patterns correspond with specific planes (hkl) of a crystal lattice and thus the crystal structure(s) of a sample can be extracted from this type of data. Furthermore, the relative intensity of peaks can indicate composition of the sample and the shape of the peaks can indicate information on crystallite size, texture, or lattice strain.

For this work, the primary purpose of XRD data was to observe changes in particle size that occurred due to time on stream or sample pretreatment. Thus, the following section (Section D.1) describes methods to calculate crystallite size from the diffraction patterns presented in Chapters 9 and 10. XRD was not used to extract information on compositional analysis of the samples; however, the method typically used to perform such analysis (Rietveld analysis) is described in Section D.2.

D.1. Measuring crystallite size with XRD data

Generally, peak breadth is inversely proportional to the thickness of the crystallite measured, however several other factors can contribute to relative peak width; namely lattice strain and instrumental broadening. Thus, as described in equation D.1, the width of a diffraction peak, $ß_{hkl}$, has three primary contributing factors: broadening due to the instrument $ß_i$,

broadening due to lattice strain, β_s, and broadening due to the crystallite depth, β_D.

$$\beta_{hkl} = \beta_i + \beta_s + \beta_D \quad (D.1)$$

The contributions of each factor in equation D.1 have different dependencies on the angle of diffraction. Thus, the three factors can be isolated by analyzing the relationship between peak breadth and the diffraction angle. Two primary methods were used to perform such analysis and calculate the crystallite size from the peak broadening: The Scherrer method (Section D.1.1) and the Williamson-Hall method (Section D.1.2). In addition to these two methods, several methods have been developed using Fourier transforms to deconvolute the contributions from size and strain from peak shape[1].

D.1.1. The Scherrer Method

The first method that was used to measure particle size was the Scherrer method which relates the peak breadth directly to crystallite size. The Scherrer equation on which the method is based describes the relationship between the peak breadth due to the crystallite size β_D, and the diffraction angle θ:

---

[1] Marinkovic, B., Avillez, R., Saavedra, A., Assuncao, F., *Mat Res,* (2001), 4, 71-76.

$$D = \frac{k\lambda}{\beta_D cos\theta} \quad (D.2)$$

In equation D.2, λ is the wavelength of the radiation (1.54056 A°) and k is a constant which can vary between 0.8 and 1.2 based on the crystallite shape (in this case we use 0.94). Thus, the Scherrer equation can be utilized to measure crystallite size based on a specific Bragg peak. The precious metal particles were assumed to be bimetallic crystallites with a face centered cubic structure (ICDD 40356) which was in agreement with the position of the Bragg peaks (diffraction data shown in Chapter 10 of the thesis). Particle size was calculated for the (111) peak (of the FCC crystallites) for samples calcined for one hour at 550, 650, 750, or 850°C. Particle size was calculated assuming it was equivalent to crystallite size. As shown in Table D.1, peaks were not detected for samples calcined at either 550°C or 650°C indicating that the particle size was less than 5 nm.

Table D.1: Particle size calculated for the (111) peak of the FCC precious metal crystal structure using the Scherrer expression (equation D.2)

Calcination temperature (celsius)	FWHM (°)	Particle size (nm)
550	ND	ND
650	ND	ND
750	0.80	11.1
850	0.47	18.8

ND = not detected

In the particle size data presented in Table D.1, neither the contributions due to instrumental broadening nor for lattice strain are

considered. Using the Scherrer method, instrumental broadening can be isolated by measuring the slope of cosθ versus the inverse of the peak breadth ß for several different Bragg peaks. In this case, the peak breadth was measured as the full width at half maximum (FWHM) for four bragg angles in each diffraction pattern. These results are shown in Tables D.2 and D.3 for two samples: a fresh catalyst precalcined at 850°C for one hour and a fresh sample precalcined at 750°C for one hour.

Table D.2: Data calculated to perform Scherrer method for fresh catalyst precalcined at 850°C for one hour

850°C Calcined sample				
hkl	2θ	FWHM	1/ß	cosθ
111	40.5	0.47	121.93	0.94
200	47.1	0.50	114.61	0.92
220	68.8	0.80	71.63	0.83
311	83.0	1.05	54.58	0.75

Table D.3: Data calculated to perform Scherrer method for fresh catalyst precalcined at 750°C for one hour

750°C Calcined sample				
hkl	2θ	FWHM	1/ß	cosθ
111	40.5	0.80	71.63	0.94
200	47.1	1.00	57.31	0.92
220	68.8	1.40	40.93	0.83

According to equation D.2, the crystallite thickness, *D*, was calculated from the slope of the plots in Figure E.1 (the slope = kλ/D from rearrangement of equation D.2).

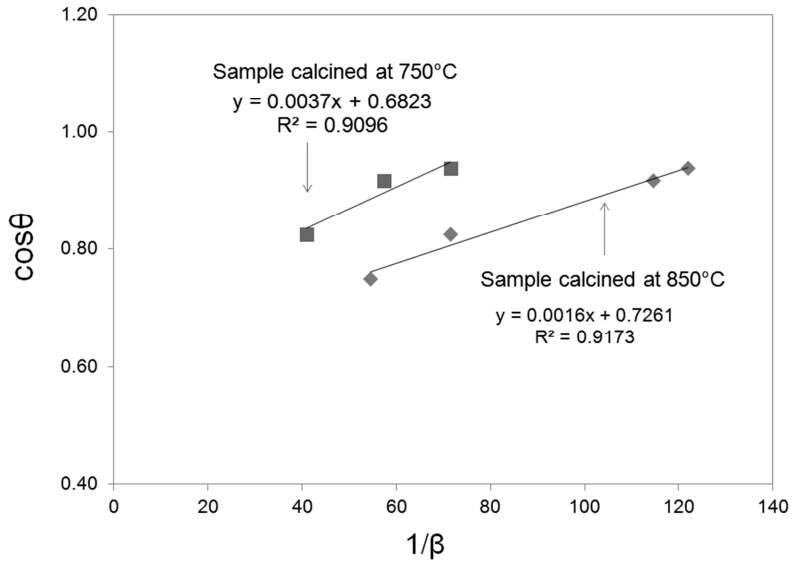

Figure D.1: Cosθ vs 1/ß plotted to perform Scherrer analysis on samples precalcined at either 750 or 850°C

A modification to the Scherrer expression was required to account for the geometry of the experimental set-up. The detector used in these experiments was a point detector without sample rotation, thus, the width was only half of that expected with a set-up that incorporated sample rotation[2]. This factor of two is accounted for in the results in both Tables D.1 and D.4.

[2] Ying, A., Osting, B., Noyan, I.C., Murray, C., Holt, M., Maser, J. *J. Appl. Cryst.* (2010). 43, 587-595

Table D.4: Particle size calculated based on Scherrer analysis of data plotted in Figure D.1

Calcination temperature (celsius)	Particle size (nm)
650	ND
750	19.4
850	27.5

A discussion of these results and how they compare to particle size measured utilizing additional methods is presented in Chapter 10 of the thesis.

D.1.2. Williamson-Hall methods

The Williamson-Hall method is based on the relationship between lattice strain,ε, and diffraction angle which takes on the relationship ε=ßsinθ. The Williamson-Hall method assume that the contributions from lattice strain and crystallite size on the peak width are additive. The expression on which the method is based is a modification of equation D.2:

$$\beta_{hkl} = \frac{k\lambda}{Dcos\theta} + 4\varepsilon tan\theta \quad (D.3)$$

Rearranging equation D.3 the Williamson-Hall equation can be written:

$$\beta_{hkl} cos\theta = \frac{k\lambda}{D} + 4\varepsilon sin\theta \quad (D.4)$$

Since peak broadening due to strain and crystallite size have a different dependence on θ, these factors can be isolated. By plotting $ß_{hkl}$cosθ by 4sinθ, both the strain (slope) and crystallite size (from y-intercept) can be calculated. This analysis is shown in Figure D.2 for the two samples with

different calcination temperatures discussed in the previous section (data provided in Tables D.2 and D.3).

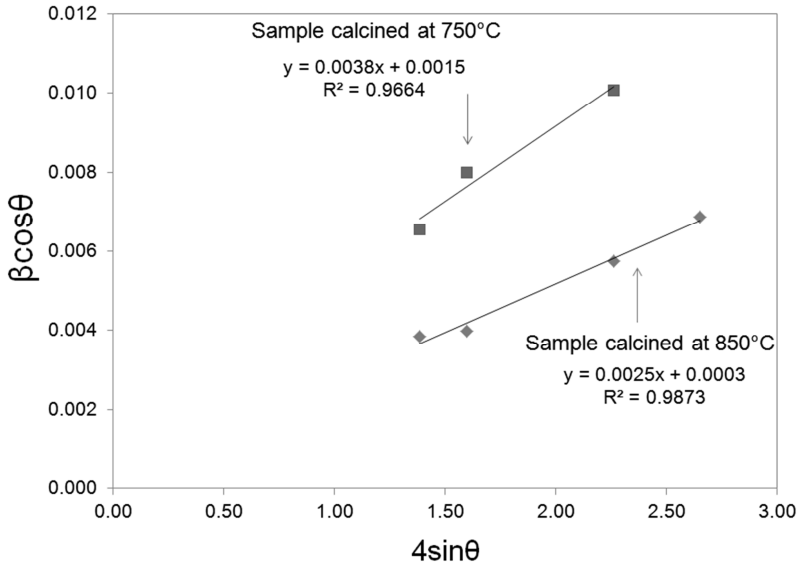

Figure D.2: βcosθ vs 4εsinθ in order to perform Williamson-Hall analysis on samples precalcined at 750 or 850°C for one hour

The corresponding lattice strain and crystallite size were calculated based on the slope and y-intercept of the plots in Figure D.2 and are given in Table D.5.

Table D.5: Strain and crystallite size calculated according to Williamson-Hall method for catalysts precalcined at either 750 or 850°C for one hour

Sample	Strain ε (no unit)	Crystallite size (nm)
750°C	3.82E-03	47.34
850°C	2.46E-03	282.64

The positive slope in Figure D.2 indicates that positive strain exists (a crystallite without strain should have a null slope). The corresponding stress of the crystal was calculated according to the uniform stress deformation

model (USDM) utilizing Hooke's law[3] assuming the stress and strain are proportional according to Youngs modulus, Y:

$$\sigma = Y\varepsilon \quad (D.5)$$

The Youngs modulus, a measure of the stiffness of a material, was assumed to be 230 GPa based on previously reported data in the literature for Rh-Pt alloys[4]. The corresponding crystallite size and lattice stress and strain are given in Table D.6.

Table D.6: Stress, strain and crystallite size calculated assuming Hooke's law for samples precalcined at 750 or 850°C for one hour

Sample	Strain ε (no unit)	Crystallite size (nm)	σ (MPa)
750°C	3.82E-03	47.34	879.34
850°C	2.46E-03	282.64	566.69

D.2. Compositional analysis

In order to determine the composition of a sample, the Rietveld refinement technique can be utilized, which uses a least squares method to minimize the difference between an observed intensity profile and an expected intensity profile. The expected intensity profile is computed by

[3] Zak, A., Majid, W., Abrishami, M., Yousefi, R., *Sol State Sci.* (2011) 43, 251-256.

[4] Tahir Çağin, Yoshitaka Kimura, Yue Qi, Hao Li, Hideyuki Ikeda, William L. Johnsonb and William A. Goddard (1998). *MRS Proceedings*, 554, 43 doi:10.1557/PROC-554-43.

combining potential unit cell structures (which may have overlapping peaks) and assuming a peak shapes based on a variety of factors (such as lattice imperfection, sample texture, etc.). Several programs are available to perform such an analysis and these programs require detailed information on the instrumental set-up and sample preparation as well as the potential unit cell reference files. The MAUD (materials analysis using diffraction) program was utilized to perform analysis of composition. The standard reference files utilized during analysis of the diffraction patterns in Chapter 10 were identified using the FIZ Karlsruhe inorganic crystal structure database (ICSD) and are shown in Table D.7.

Table D.7: ICSD reference files utilized for XRD analysis of Rh-Pt/SiO_2-ZrO_2 samples

ICSD ref. number	Structure formula	Crystal system
72700	ZrO_2	tetragonal
9482	SiO_2	hexagonal
64991	Rh	face centered cubic
40356	Rh-Pt	face centered cubic
64912	Pt	face centered cubic

For this study the refinement was only calculated utilizing a simplified analysis that did not include factors such as strain and texture. The result was an analysis that was not within acceptable margins for typical Rietveld analysis (for instance, to $\sigma<1.5$). Further, more precise methods were used to measure composition data (as discussed in Chapter 10). Future work on analysis of the crystal structure of the Rh-Pt/SiO_2-ZrO_2 catalyst, or on additional materials, can benefit from Rietveld refinement programs such as

MAUD and can improve the analysis performed here by incorporating additional types of analysis (strain and texture) which will improve the data fit.

Appendix E: Niobium as a replacement for Cerium in OSC materials

Cerium, a rare earth metal, is becoming increasingly expensive inhibiting the application of ceria-based oxygen storage components (OSC) and raising the price of the catalysts they support. OSC materials are used in many applications, notably, in the three-way catalyst (TWC) in vehicle exhausts. Therefore, finding an adequate replacement for cerium is necessary. Niobium is a promising element to replace some of the cerium present in current oxygen storage components[5] because it can have multiple oxidation states. Therefore, in this study, OSC materials are produced that incorporate niobium to determine whether it provides enhanced OSC. The effect of doping ceria-zirconia complexes with niobium is explored through the analysis of reduction/oxidation performance.

E.1. Materials and Methods

In this study, the current OSC materials utilized in the TWC are compared to potential niobium-containing OSC materials. The baseline material was CeO_2-ZrO_2 Low concentrations of yttrium were added to

---

5. A. Bortun and J. Nunan, "Niobium containing zirconium-cerium based solid solutions", U.S. Patent 6 468 941, Oct. 22, 2002

materials as a promoter for thermal stability. The list of materials that were investigated is shown in Table E.1.

Table E.1: Materials synthesized for OSC testing

Baseline materials	Mole% Ce	Mole% Nb
$Zr_{0.80}Ce_{0.20}O_2$	6.7%	0.0%
Nb_2O_5	0.0%	28.6%
CeO_2	33.3%	0.0%
Materials with varying concentrations Nb:	**Mole% Ce**	**Mole% Nb**
$Zr_{0.701}Ce_{0.216}Y_{0.081}O_2$	7.2%	0.0%
$Zr_{0.65}Ce_{0.20}Y_{0.075}Nb_{0.075}O_2$	6.7%	2.5%
$Zr_{0.62}Ce_{0.19}Nb_{0.12}Y_{0.071}O_2$	6.3%	4.0%
$Zr_{0.59}Ce_{0.18}Nb_{0.16}Y_{0.068}O_2$	6.0%	5.3%

After synthesis and aging, the materials were investigated for the extent, rate and temperature of their reduction and oxidation. The goal was to determine whether the materials had higher OSC material when niobium was included.

E.1.1. Synthesize of OSC materials

To prepare CeO_2 and $Zr_{0.8}Ce_{0.2}O_2$ samples, a water solution of the $CeNO_3$ (and $ZrO(NO_3)_2$ in addition for the latter) was slowly added to a vigorously stirred 0.2 M Ammonium Hydroxide solution to precipitate the sample. To prepare the various $(Ce_xZr_yNb_zY_{1-x-y-z})O_2$ samples, a water solution of the $CeNO_3$, $ZrO(NO_3)_2$,YNO_3 and $C_6H_4NNbO_{12}$ was added by

burette to vigorously stirred 0.2 M solution of ammonium hydroxide. Following precipitation, samples were filtered, triple washed, dried and calcined at 550°C followed by aging in air at 900°C for 48 hours. The baseline Nb_2O_5 sample was dried at 120°C for 2 hours followed by calcination in air at 550°C for 2 hours. Samples were crushed and sieved to particle sizes between 600-700µm. For precious metal containing samples, 0.5wt% platinum was deposited on calcined materials using the incipient wetness technique with a proprietary BASF Pt "A" salt. Samples were then dried, re-calcined and aged at 900°C for 48 hours

E.1.2. OSC measurements

The adsorption and desorption of oxygen in either lean or rich conditions was measured using TGA. Two types of measurements were performed. Isothermal redox cycling was performed at 450, 550 or 650°C which exposed the catalyst to alternating cycles of reducing (2% H_2 in N_2) and oxidizing (1% O_2 in N_2) conditions. Additionally, TPR/TPO cycles were conducted to determine total reduction and oxidation capacity over a range of temperatures. For TPR/TPO tests a heating and cooling rate of 5°C/min was used with minimum temperature of 30°C and maximum of 900°C. In between TPR and TPO cycles, a 30-minute isothermal step at 30°C was performed. All tests were performed with a Netzsch STA 449F3. Prior to all tests the samples were pre-dried in Nitrogen at 150°C for 1 hour to remove moisture.

The data was characterized by the mole percent cerium assuming reduction from the +4 to the +3 oxidation state according to the following equation:

$$2CeO_2 + H_2 \rightarrow Ce_2O_3 + H_2O \quad (C.1)$$

E.1.3. XRD

XRD was used to provide insight into the crystallite size and structure of the samples. Powder XRD patterns were recorded with a INEL XRG 3000 using Cu-Kα radiation of wavelength 1.541 Å. XRD results were used to determine the impact of the niobium on the crystal structure of the Ce-Zr oxide. The XRD patterns of the mixed oxides (the niobium-containing materials in Table 1) did not show evidence of Nb_2O_5 crystallites, nor cubic CeO_2.

E.1.4. BET Surface area

Single point BET surface area was performed with a Quantachrome ChemBET Pulsar unit. Surface areas of all materials were in the range of 12-25 m^2/g. Drastic losses in surface area of all materials occurred after air treatment at temperature above 950°C which was correlated to significant losses in performance. A significant impact of niobium on surface area was not observed.

E.2. Redox capacity of niobium containing OSC materials

Several niobium-containing materials were investigated and the optimum formulation was identified according to the total reduction capacity during TPR to 900°C. The total reduction capacity for the four formulations is shown in Table E.2.

Table E.2. Extent of Ceria reduced for OSC materials containing varying concentrations of Niobium (total reduction calculated at 900°C).

Materials with varying concentrations of Nb:	Mole% Nb	Measured H_2 uptake (mmol H_2/g)	Mole% Ce reduced
$Zr_{0.701}Ce_{0.216}Y_{0.081}O_2$	0.0%	0.68	79.3%
$Zr_{0.65}Ce_{0.20}Y_{0.075}Nb_{0.075}O_2$	2.5%	0.71	87.4%
$Zr_{0.62}Ce_{0.19}Nb_{0.12}Y_{0.071}O_2$	4.0%	0.66	90.2%
$Zr_{0.59}Ce_{0.18}Nb_{0.16}Y_{0.068}O_2$	5.3%	0.54	75.5%

An optimum niobium concentration of 4% was identified to maximize reduction. Several of the niobium-containing compounds increased total oxygen storage (OS) compared to the compound without niobium.

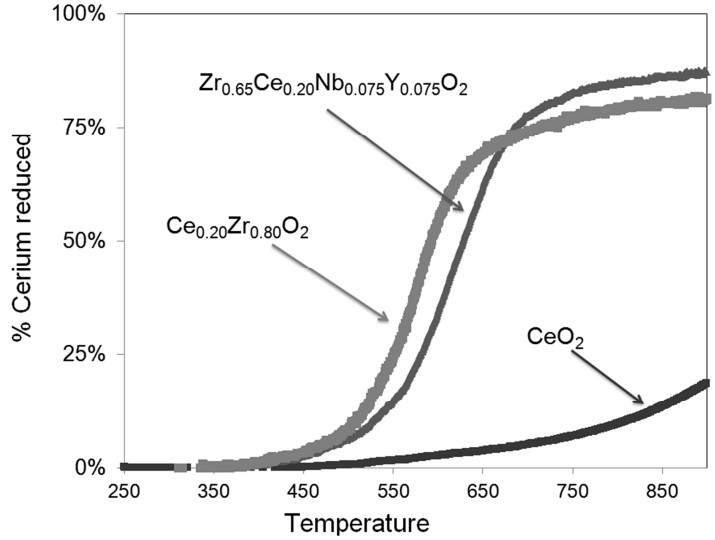

Figure E.1: TPR profiles for $Zr_{0.65}Ce_{0.20}Nb_{0.075}Y_{0.075}O$, $Ce_{0.20}Zr_{0.80}O_2$, and CeO_2. The y-axis is %cerium based on theoretical CeO_2 reduction to Ce_2O_3

The operating range of the TWC is 250-600°C[6], therefore, the temperature that the reduction/oxidation occurs is an important parameter in the determining the viability of a niobium-containing TWC. Although it was found that niobium could increase the overall extent of reduction and oxidation (Table E.2) compared to the compound without niobium, the additional extent of reduction did not occur until temperatures above 650°C, higher than the typical operating temperature of the TWC.

Therefore, it was found that the presence of niobium increases the reduction/oxidation capacity of traditional Ce-Zr oxides but the temperature

---

[6] R.M. Heck, R.J. Farrauto, S.T. Gulati, Catalytic air pollution control : commercial technology, 3rd ed., John Wiley, Hoboken, N.J., 2009

that reduction occurred was too high for the desired application. For niobium-containing compounds to be useable in this application, the reduction temperature of the niobium would need to be lowered. TWC materials contain precious metal, and it has been shown that precious metal can lower the reduction temperature of OSC materials[7]. Further, it has been shown that platinum can lower the reduction temperature of niobium[8]. Thus, the materials in Table E.1 were impregnated with 0.5% platinum to investigate whether the addition of the precious metal might lower the niobium reduction temperature, thereby enabling additional redox capacity of niobium within the operating temperature range of the TWC.

E.3. Redox capacity of platinum and niobium-containing OSC materials

As shown in Figure E.2, the presence of 0.5wt% platinum significantly lowered the reduction temperature of the niobium-containing formulations. Further, the presence of platinum increased the extent of reduction to over 100% of the Cerium present (assuming reduction of CeO_2 to Ce_2O_3), at temperatures below 650°C. Thus, significant reduction of the niobium

---

[7] P.S. Lambrou, C.N.Costa, S.Y.Christou, A.M.Efstathio, Applied Catalysis B, 54 (2004), 237-250

[8] Zha, Y., (2001) The Rational Preparation of Niobia Supported and Promoted Platinum Catalysts (Doctoral dissertation)

occurred. The materials were found to be stable during 24-hrs of redox cycling at 600°C.

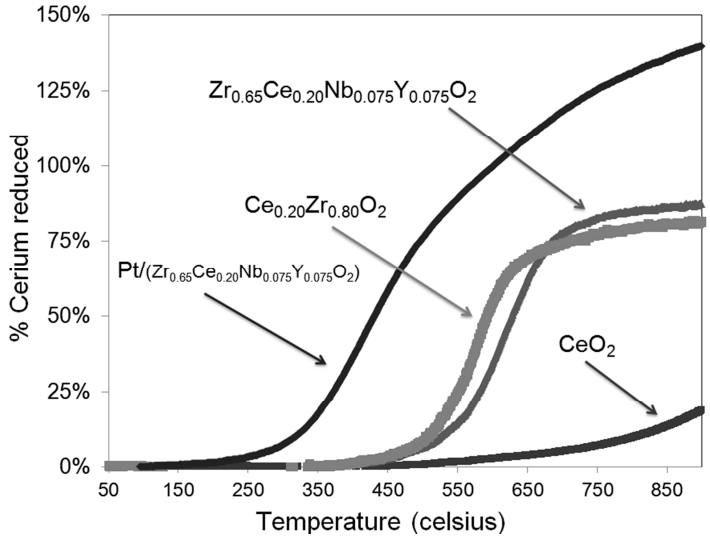

Figure E.2. TPR profiles for 0.5wt%Pt/($Zr_{0.65}Ce_{0.20}Nb_{0.075}Y_{0.075}O$), $Zr_{0.65}Ce_{0.20}Nb_{0.075}Y_{0.075}O$, $Ce_{0.20}Zr_{0.80}O_2$, and CeO_2. The y-axis is %cerium reduced based on theoretical CeO_2 reduction to Ce_2O_3

E.4. Conclusions and future work

This study indicates that niobium may be a potential replacement for some amount of cerium present in the oxygen storage component of the TWC without any loss in OSC performance. Future work will investigate additional formulations of precious metal and niobium-containing OSC materials and study redox conditions more similar to those in vehicle exhaust.